Technische Universität München

Max-Planck-Institut für Astrophysik

Fakultät für Physik

General Relativistic Multidimensional Flux-Limited Diffusion Scheme for Neutrino Transport and its Application to Core-Collapse Supernova Simulations of Very Massive Stars

Ninoy Rahman

Vollständiger Abdruck der von der Fakultät für Physik der Technischen Universität München zur Erlangung des akademischen Grades

Doktors der Naturwissenschaften (Dr. rer. nat.)

genehmigten Dissertation.

Vorsitzende/-r: Prof. Dr. Lothar Oberauer
Prüfer der Dissertation: 1. apl. Prof. Dr. rer. nat. Hans-Thomas Janka
2. Prof. Dr. Alejandro Ibarra

Die Dissertation wurde am 14.01.2019 bei der Technischen Universität München eingereicht und durch die Fakultät für Physik am 01.02.2019 angenommen.

Acknowledgements

Contents

Chapter 1

Introduction

A massive star ($> 8\,\mathrm{M}_\odot$) at the end of its life undergoes core-collapse and possibly explodes as a supernova (SN). The core-collapse supernova (CCSN) mechanisms have been reviewed in past years, e.g. by Janka (2012), Burrows (2013), Janka (2017a), and Janka (2017b). At the end of the star's life, after subsequent nuclear burning stages, a massive star forms an iron core with onion-like shells of silicon and other lighter elements. The iron core is supported against gravity mainly by electron degeneracy pressure. The iron core mass grows due to ongoing shell burning of silicon. When the mass of iron core grows to a mass close to the Chandrasekhar mass, the iron core collapses. The iron core collapse is accelerated by the photodisintegration of iron group nuclei at high temperature and the deleptonization (electron capture on nuclei). Both processes decrease the pressure support against gravity and the core collapses in a homologous manner, the infall velocity increases linearly with radius. The neutrinos produced by electron capture on nuclei, initially escape the core and carry away energy and lepton number. When the central density of the core reaches $\sim 10^{11}$ g/cm^3, neutrinos begin to become trapped and are carried inward with the infalling material. The neutrinos are in equilibrium with the stellar material when the density reaches a value of $\sim 10^{12}$ g/cm^3.

When the core reaches the nuclear saturation density of $\sim 2.8 \times 10^{14}$ g/cm^3, the implosion of the core is stopped by the repulsive part of nuclear forces, forming a proto-neutron star (PNS) and a pressure wave that turns into a shock front. The shock propagates outwards and loses energy by dissociating iron group nuclei into free nucleons (protons and neutrons). When the post-shock densities drop below $\sim 10^{11}$ g/cm^3, previously trapped neutrinos can escape and produce the so-called shock breakout neutrino burst.

The shock loses its energy by dissociation of the iron-group nuclei and deleptonization. Consequently, the shock stagnates. The temperature of the PNS rises along with its ongoing compression and continuous mass accretion. The hot PNS obtains additional thermal pressure support due to its high temperature. As a result, a hot PNS can support more mass than a cold neutron star (NS). Rotation can add centrifugal support against gravity. Consequently, a rotating PNS can support additional mass.

The matter accreting onto a newly born PNS releases its gravitational binding energy partially in the form of neutrino radiation and, in addition, neutrinos continue to diffuse out of a hot PNS. A part of these neutrinos get absorbed on the layer behind the shock. The neutrino absorption proceeds through the following charged-current reactions:

$$\nu_e + n \rightarrow e^- + p$$
$$\bar{\nu}_e + p \rightarrow e^+ + n \tag{1.1}$$

These absorption processes lead to heating of the matter behind the shock. This region between the PNS and the shock with net neutrino heating is called "gain region". Different fluid instabilities can develop in this gain region: convection (see, e.g. Herant et al. 1994; Janka and Mueller 1996; Murphy, Dolence, and Burrows 2013) and the "standing accretion shock instability" (SASI, see, e.g. Blondin, Mezzacappa, and DeMarino 2003; Foglizzo, Scheck, and Janka 2006; Foglizzo et al. 2007; Fernández 2015). SASI can cause large-scale deformation of the stagnating shock. Fluid instabilities allow for enhanced neutrino heating and create turbulant pressure, thus help to push the stagnating shock outward.

If enough energy is deposited behind the shock by neutrinos, the shock can be revived leading to a successful explosion. If shock revival is not achieved, due to ongoing mass accretion through the shock the PNS will eventually collapse and form a black hole (BH). Even if the shock is sucessfully revived, the deposited energy may not be enough to overcome the gravitational binding energy of the star and the shock-heated material can fall back and cause the collapse of the PNS to a BH. After the shock revival, accretion onto the PNS can continue through downdrafts surrounding the shock-heated material. A BH can be formed due to this ongoing mass accretion. In this case, some shock-heated material may escape the gravitational pull by the BH or all post-shock matter may fall back into the BH.

In this study, we conduct core-collapse simulations of the very massive stars ($\simeq 100$ M$_\odot$, see, e.g. Vink 2015 for definition of very massive stars) which have undergone phases of so-called pulsational pair-instability supernovae (PPISN). A non-rotating very massive star may experience pulsational pair-instability (PPI) if it forms a helium core of 35-64 M$_\odot$ (Woosley and Heger, 2015). If the central temperature, T_c, of a very massive star reaches a value of $\sim 10^8$ K, gamma-ray photons are produced. In the post-carbon burning phase, if $T_c > 3 \times 10^9$ K, gamma-ray photons are energetic enough to be converted to electron-positron pairs. As a consequence, the outer layers of such a star, which are supported against gravity by the photon pressure, experience contraction. The contraction causes the temperature to rise further. Due to the high temperature, rapid burning of carbon, oxygen and in some case even silicon can take place. If the burning releases enough energy, the contraction is stopped and the star rebounds. So, the star experiences pulsations and this phenomenon is called pulsational pair-instability (PPI). If the mass of the helium core is above 65 M$_\odot$, the energy released in the rapid burning is high enough to explode the whole star in a single pulse. This is called a pair-instability supernova. For helium core masses over 133 M$_\odot$ the pair-production instability leads to a direct collapse of the star to a BH. In the case of PPI progenitors, the very massive star experiences multiple pulsations and eventually forms an iron core at the center. Due to PPI the outer hydrogen layer and in some cases the outer helium layer are ejected. This phenomenon is called the (PPISN). Eventually, the iron core collapses.

The PPI has several astrophysical consequences. The helium shells ejected due to pulsations can collide with each other or with previously ejected hydrogen. The collision between shells can produce supernova-like light curves. For example, one of the most massive stars in our galaxy, Eta Carinae, with a mass of approximately 120 M$_\odot$, might encounter or already has undergone PPI. Smith (2013) made a plausible claim that the 19th century "Great Eruption" of Eta Carinae requires an interaction of the ejected shell, expelled by an explosive mechanism from the star, and the circumstellar material. This kind of eruption produces a Type IIn supernova-like light curve and is sometimes called "supernova imposter".

A rapidly rotating very massive star can leave a BH with an accretion disk as remnant upon its death. The accretion disk can act as a source of neutrinos. In the

so-called collapsar model, the emitted neutrinos deposit energy near the rotation axes by pair annihilation or by scattering with electrons. If enough energy is transferred by neutrinos to the matter, a jet can be launched. The jet may eventually burst out of the star and could lead to a long gamma-ray burst (see, e.g. Woosley 1993; MacFadyen and Woosley 1999).

Recently, Chan et al. (2018) studied the core-collapse of a metal-free 40 M$_\odot$ progenitor of Heger and Woosley (2010) and Kuroda et al. (2018) of a metal-free 70 M$_\odot$ progenitor of Takahashi, Umeda, and Yoshida (2014) in three dimensions. Both papers reported shock expansion by neutrino heating before BH formation. Chan et al. (2018) obtained the shock expansion by artificially increasing the neutrino heating. In their model, after the shock expansion, due to ongoing accretion onto the PNS, a BH is formed. Meanwhile, the shock has expanded to 4000 km. The energy of the shock-heated expanding material is barely equal to the binding energy of the overlaying stellar material. The shock-heated material transfers its energy to the surrounding infalling material by mechanical work while still expanding. Eventually, most of the originally neutrino heated material falls back onto the BH, but the energy transferred was enough to make the surrounding material unbound and the supernova shock breaks out. In Kuroda et al. (2018), the shock expansion starts only 40 ms before BH formation. Kuroda et al. (2018) claimed that the shock expansion starts due to the high neutrino emission before BH formation. Unfortunately the authors did not continue the simulation beyond BH formation.

In this work, we conduct a systematic study of the core collapse of very massive stars with zero-age main sequence masses of 60 M$_\odot$ (rapidly rotating), 80 M$_\odot$ (rotating and non-rotating) and 115 M$_\odot$ (non-rotating) with massive iron cores (>2.3 M$_\odot$). We have conducted two dimensional general relativistic hydrodynamics simulations with neutrino transport. We aim to answer the following questions in this work: what are the final remnants of the core collapse of the above-mentioned set of very massive stars, BHs or NSs? Can shock expansion, as reported by (Chan et al., 2018) and Kuroda et al. (2018), take place before BH formation? What is the impact of rotation and progenitor mass? If a BH is formed, what are the properties of the BH and what are the characteristics of the neutrinos emitted? What happens to the expanding shock after BH formation?

A general relativistic treatment of gravity and hydrodynamics is desirable for the study of CCSNe beyond BH formation. Also neutrino transport plays a crucial role in this scenario. In this work, we developed a general relativistic multidimensional neutrino transport solver and applied it in our core-collapse simulations of very massive stars. CCSNe are the main distributors of heavy elements in the universe (A>12) (see, e.g. Janka et al. 2007), and the nucleosynthesis yields in CCSNe depend sensitively on the neutron-to-proton ratio of the ejecta. This enhances the importance of determining detailed properties of emitted neutrinos because neutrino interactions set the electron fraction and thus the neutron-to-proton ration in the ejected matter.

During the last several decades, various approaches have been developed for treating neutrino transport in hydrodynamical simulations. The most sophisticated schemes solve the full Boltzmann equation, e.g. by direct discretization using finite differences (see, e.g. Liebendörfer et al. 2004; Livne et al. 2004; Sumiyoshi and Yamada 2012), or by employing a Monte Carlo treatment (see, e.g. Janka and Hillebrandt 1989; Abdikamalov et al. 2012; Richers et al. 2015), or by coupling a somehow simplified Boltzmann solver to an additional system of equations for the lowest angular moments of the Boltzmann equation (see, e.g. Rampp and Janka 2002; Foucart

2018). While these methods have the advantage of providing the full phase-space information of the generally six-dimensional distribution function of neutrinos, they still are too expensive in terms of computational resources to be used for long-term, high-resolution simulations, or for exhaustive parameter exploration. In this work, we construct and apply a multi-dimensional multi-energy-group flux-limited diffusion scheme with energy-bin coupling in full general relativity. Although FLD is not known to generally produce more accurate results than an M1 code, we opted for the FLD approach mainly for two reasons. First, FLD evolves only a single equation per neutrino species and energy bin, whereas M1 evolves three additional flux-vector components. Particularly in GR this reduces the complexity of the equations and (at least potentially) improves the computational performance. Second, the M1 method is currently employed already in several existing codes. Developing different, complementary algorithms therefore enhances diversity of applied methods and in the long run might help to discriminate numerical artefacts from physical effects.

The concept of FLD was first introduced by Pomraning (1981) and Levermore and Pomraning (1981) and since then has been used, apart from many applications in the context of photon transport, for neutrino transport in CCSNe and PNS cooling (Bowers and Wilson, 1982; Bruenn, 1985; Burrows and Lattimer, 1986; Myra et al., 1987; Baron et al., 1989; Cernohorsky, 1990; Burrows et al., 2007; Lentz et al., 2015; Bruenn et al., 2018). Cooperstein and Baron (1992) derived the FLD equation correct to order v/c. The maximum entropy principle was applied by Cernohorsky, van den Horn, and Cooperstein (1989) in FLD to determine Eddington factors. Baron et al. (1989) generalized the FLD approach to the general relativistic context. An improved flux-limiter was suggested by Janka (1992) based on the comparison with a Monte-Carlo study. A two dimensional, multi-group (i.e. energy-dependent) FLD scheme for neutrinos was developed by Swesty and Myra (2009).

General relativistic (GR) radiative transfer as a scientific discipline was established with the formulation of the Boltzmann equation in GR by Lindquist (1966) and of the corresponding two moment formalism in Thorne (1981). Until rather recently, most numerical applications were restricted to spherical symmetry (e.g. Baron et al., 1989; Bruenn, De Nisco, and Mezzacappa, 2001; Liebendörfer et al., 2004). A few years ago, multi-group GR transport has found its way into multiple dimensions. For instance, Müller, Janka, and Dimmelmeier (2010) have solved the two-moment equations with a variable Eddington-factor method using the conformal-flatness condition and the ray-by-ray-plus approximation (Buras et al., 2006). Moreover, Sekiguchi et al. (2016), O'Connor (2015), and Kuroda, Takiwaki, and Kotake (2016), and Roberts et al. (2016) have employed the M1-method to solve neutrino transport in full general relativity.

Our algorithm employs spherical polar coordinates and solves the GR equations using the partially implicit Runge-Kutta method (Montero and Cordero-Carrión, 2012; Baumgarte et al., 2013). The transport equations are solved in the comoving (i.e. fluid-rest) frame. In order to avoid multi-directional coupling of grid cells, and therefore the inversion of matrices spanned over the entire grid, we employ operator splitting. The source terms, the radial- and energy-derivatives, as well as the non-radial derivatives are integrated separately, each using an appropriate discretization scheme. In this way, the scheme can be parallelized in a straightforward manner and remains numerically less complex than an unsplit, fully implicit solver.

1.1   Organization of this Thesis

In chapter 2, we present the governing equations of general relativistic radiation hydrodynamics. The Einstein equation in covariant BSSN formulation is shown. We also show the hydrodynamics equations (the continuity and Euler equations) in the generalized Valencia formulation suitable for a curvilinear coordinate system (e.g. spherical-polar coordinates). We also present the evolution equation for the comoving-frame neutrino energies and introduce the concept of the flux-limited diffusion approximation. We present our new numerical algorithm for neutrino transport and show the discretization method for the transport equation in detail.

In chapter 3, we present several idealized tests for radiation transport. We assess different features of our newly developed algorithm for radiation transport and validate our implementation by doing these tests. We also present a one-dimensional CCSN simulation of a massive star with "realistic" microphysics. We compare our results for Newtonian tests with results obtained with the ALCAR code of Just, Obergaulinger, and Janka (2015). The ALCAR code uses an M1 scheme for neutrino transport. We also evaluate general relativistic effects of neutrino transport and compare with other existing work (Bruenn, De Nisco, and Mezzacappa, 2001; Marek et al., 2006; Müller, Janka, and Marek, 2012).

In Chapter 4, we present the results from CCSN simulations of very massive stars in two dimensions. We used several progenitors of very massive star for our study. We show the dynamical evolution of the shock as well as different properties of the newly formed compact remnant, gain layer and emitted neutrinos. We study the dependence of the shock revival on the progenitor structure and the effects of rotation on the shock dynamics and black hole formation. We evaluate properties of the newly born BH. We also present one simulation after BH formation to see the evolution of shock-heated material.

Chapter 2

Numerical Method

In this section, we introduce the basic equations used for our general relativistic radiation-transport method. We use a spherical polar coordinate system. Throughout the paper we follow the convention that a, b, c, μ, ν run over space-time index 0, 1, 2, 3 and i, j, k, l run over space index 1,2,3. We denote quantities defined in the comoving orthonormal frame by using an index with a hat ($\hat{i}, \hat{j}, \hat{k}$...) and quantities defined in the comoving curvilinear frame index with a bar ($\bar{i}, \bar{j}, \bar{k}$...). We denote the electron neutrinos and the electron anti-neutrinos as ν_e, $\bar{\nu}_e$ respectively and the muon and tau neutrinos and their anti-neutrinos combinedly as ν_x.

2.1 Metric equations

We use a $3 + 1$ decomposition in which the space-time manifold is foliated into space-like hyper-surfaces Σ (see, e.g., Baumgarte and Shapiro 2010). We denote the 4-metric as g_{ab}. The time-like future pointing normal vector to Σ is n^a, and the space-like 3-metric on Σ is γ_{ij}. The line element is then given by:

$$
\begin{aligned}
\mathrm{d}s^2 &\equiv g_{ab}\mathrm{d}x^a\mathrm{d}x^b \\
&= -\alpha^2\mathrm{d}t^2 + \gamma_{ij}(\mathrm{d}x^i + \beta^i\mathrm{d}t)(\mathrm{d}x^j + \beta^j\mathrm{d}t) ,
\end{aligned}
\tag{2.1}
$$

where α, β^i are the lapse function and shift-vector, respectively, and

$$
\begin{aligned}
\gamma_{ab} &= g_{ab} + n_a n_b , \\
n^a &= (1/\alpha, -\beta^i/\alpha) , \\
n_a &= (-\alpha, 0, 0, 0) .
\end{aligned}
\tag{2.2}
$$

Moreover,

$$
\bar{\gamma}_{ij} \equiv \mathrm{e}^{-4\phi}\gamma_{ij}
\tag{2.3}
$$

is the conformal metric, with the conformal factor $\exp(4\phi)$ (see, e.g. chapter 3 of Baumgarte and Shapiro 2010 for detail discussion about conformal transformation). Furthermore, the extrinsic curvature, K_{ij}, the conformal traceless extrinsic curvature, $\bar{A}_{ij}$, and the trace of the extrinsic curvature, K, are defined as:

$$
\begin{aligned}
K_{ij} &\equiv -\gamma_i{}^k\gamma_j{}^l\nabla_k n_l \\
&= -\frac{1}{2\alpha}\partial_t\gamma_{ij} + D_{(i}\beta_{j)} , \\
\bar{A}_{ij} &\equiv \mathrm{e}^{-4\phi}(K_{ij} - \frac{1}{3}K) , \\
K &\equiv K^i{}_i .
\end{aligned}
\tag{2.4}
$$

Here, We denote the symmetric parts of a tensor with a brackets (), e.g. $A_{(ij)} \equiv \frac{1}{2}(A_{ij} + A_{ji})$, where A_{ij} is a tensor. The Minkowski metric in spherical polar coordinates is $\hat{\gamma}_{ij} = \mathrm{diag}(1, r^2, r^2 \sin^2 \theta)$. We denote the connection coefficients associated with the metrics γ_{ab}, $\bar{\gamma}_{ij}$, and $\hat{\gamma}_{ij}$ as Γ^a_{bc}, $\bar{\Gamma}^i_{jk}$, and $\hat{\Gamma}^i_{jk}$, respectively. The covariant derivatives associated with γ_{ij}, $\bar{\gamma}_{ij}$, and $\hat{\gamma}_{ij}$ are denoted by D, $\bar{D}$, and $\hat{D}$, respectively. We define the connection vector Λ^i as

$$\Lambda^i \equiv \gamma^{jk} \Delta \Gamma^i_{jk} \,, \tag{2.5}$$

with

$$\Delta \Gamma^i_{jk} \equiv \bar{\Gamma}^i_{jk} - \hat{\Gamma}^i_{jk} \,, \tag{2.6}$$

and express the Ricci tensor as

$$\begin{aligned}
\bar{R}_{ij} &= -\frac{1}{2} \bar{\gamma}^{kl} \hat{D}_k \hat{D}_l \bar{\gamma}_{ij} + \bar{\gamma}_{k(i} \hat{D}_{j)} \bar{\Lambda}^k + \Delta \Gamma^k \Delta \Gamma_{(ij)k} \\
&\quad + \bar{\gamma}^{kl} \left(2 \Delta \Gamma^m_{k(i} \Delta \Gamma_{j)ml} + \Delta \Gamma^m_{ik} \Delta \Gamma_{mjl} \right) \,.
\end{aligned} \tag{2.7}$$

To evolve the space-time metric we solve the covariant BSSN equations (Baumgarte et al., 2013), which are given by:

$$\begin{aligned}
\partial_\perp \bar{\gamma}_{ij} &= -\frac{2}{3} \bar{\gamma}_{ij} \bar{D}_k \beta^k - 2\alpha \bar{A}_{ij} \,, \\
\partial_\perp \bar{A}_{ij} &= -\frac{2}{3} \bar{A}_{ij} \bar{D}_k \beta^k - 2\alpha \bar{A}_{ik} \bar{A}^k{}_j + \alpha \bar{A}_{ij} K \\
&\quad + \mathrm{e}^{-4\phi} \Big[-2\alpha \bar{D}_i \bar{D}_j \phi + 4\alpha \bar{D}_i \phi \bar{D}_j \phi \\
&\qquad\quad + 4 \bar{D}_{(i} \alpha \bar{D}_{j)} \phi - \bar{D}_i \bar{D}_j \alpha \\
&\qquad\quad + \alpha (\bar{R}_{ij} - 8\pi S_{ij}) \Big]^{\mathrm{TF}} \,, \\
\partial_\perp \phi &= \frac{1}{6} \bar{D}_k \beta^i - \frac{1}{6} \alpha K \,, \\
\partial_\perp K &= \frac{\alpha}{3} K^2 + \alpha \bar{A}_{ij} \bar{A}^{ij} \\
&\quad - \mathrm{e}^{-4\phi} (\bar{D}^2 \alpha + 2 \bar{D}^i \alpha \bar{D}_i \phi) \\
&\quad + 4\pi \alpha (\rho + S) \,, \\
\partial_\perp \bar{\Lambda}^i &= \bar{\gamma}^{jk} \hat{D}_j \hat{D}_k \beta^i + \frac{2}{3} \Delta \Gamma^i \bar{D}_j \beta^j + \frac{1}{3} \bar{D}^i \bar{D}_j \beta^j \\
&\quad - 2 \bar{A}^{jk} (\delta^i{}_j \partial_k \alpha - 6\alpha \delta^i{}_j \partial_k \phi - \alpha \Delta \Gamma^i_{jk}) \\
&\quad - \frac{4}{3} \alpha \bar{\gamma}^{ij} \partial_j K - 16\pi \alpha \bar{\gamma}^{ij} S_j \,. \tag{2.8}
\end{aligned}$$

Here,

$$\partial_\perp \equiv \partial_t - \mathcal{L}_\beta \,,$$

where $\mathcal{L}_\beta$ is the Lie derivative along the shift vector β^i. The superscript TF denotes the trace-free part of a tensor. The matter-radiation source terms are given by:

$$
\begin{aligned}
\rho &\equiv n_a n_b T^{ab} , \\
S_i &\equiv \gamma_{ia} n_b T^{ab} , \\
S_{ij} &\equiv \gamma_{ia} \gamma_{jb} T^{ab} , \\
S &\equiv \gamma^{ij} S_{ij} ,
\end{aligned}
\tag{2.9}
$$

where T^{ab} is the total stress-energy tensor of matter and radiation (see below for more explanation). We use the '1+log' slicing and the gamma driver condition to evolve α and β^i, respectively, i.e.:

$$
\begin{aligned}
\partial_t \alpha &= -2\alpha K , \\
\partial_t \beta^i &= B^i , \\
\partial_t B^i &= \frac{3}{4} \partial_t \bar{\Lambda}^i .
\end{aligned}
\tag{2.10}
$$

The time integration of equations (2.8) and (2.10) is done using a 2nd-order partially implicit Runge-Kutta method, which is described in detail in Montero and Cordero-Carrión (2012) and Baumgarte et al. (2013). The integration time step is given by the Courant-Friedrichs-Lewy condition:

$$
\Delta t = \text{CFL} \min\{\Delta r, (\Delta r/2)\Delta\theta, (\Delta r/2)\sin(\Delta\theta/2)\Delta\phi\} .
\tag{2.11}
$$

Here, $\Delta r, \Delta\theta, \Delta\phi$ are the minimum widths in the radial, polar and azimuthal directions, respectively, and CFL refers to the chosen Courant number.

2.2 Hydrodynamics

The general relativistic hydrodynamics equations expressing the local conservation of baryonic mass (with current density J^a), energy-momentum (with energy-momentum tensor T_h^{ab}), and electron lepton number (with current density J_e^a) read (e.g. Font 2008):

$$
\begin{aligned}
\nabla_a J^a &= 0 , \\
\nabla_a T_h^{ab} &= s^b , \\
\nabla_a J_e^a &= S_N ,
\end{aligned}
\tag{2.12}
$$

where

$$
\begin{aligned}
J^a &\equiv \rho u^a , \\
T_h^{ab} &\equiv \rho h u^a u^b + p g^{ab} , \\
J_e^a &\equiv \rho u^a Y_e ,
\end{aligned}
\tag{2.13}
$$

and

$$
\begin{aligned}
h &= 1 + e + p/\rho , \\
u^0 &= W/\alpha , \\
u^i &= W(v^i - \beta^i/\alpha) .
\end{aligned}
\tag{2.14}
$$

The symbols ρ, e, v^i, W, p, h, and Y_e denote the baryonic mass density, specific internal energy, 3-velocity, Lorentz factor, gas pressure, specific enthalpy, and electron fraction (equal to the number of protons per nucleon), respectively. In order to obtain explicit expressions of equations (2.12), we use the flux-conservative Valencia formulation generalized to curvilinear coordinates, as described in Montero, Baumgarte, and Müller (2014). In this formulation, singular terms proportional to $1/r$ and $\cot\theta$ are scaled out by using the reference metric $\hat{\gamma}_{ij}$. The conservative variables D, S_i, τ, and D_e that are evolved in time are defined in terms of the primitive variables ρ, e, v^i, p, and Y_e as:

$$
\begin{aligned}
D &\equiv W\rho \,, \\
S_i &\equiv W^2\rho h v_i \,, \\
\tau &\equiv W^2\rho h - p - D \,, \\
D_e &\equiv DY_e \,.
\end{aligned}
\tag{2.15}
$$

The continuity, Euler, energy, and lepton-number equations in the generalized Valencia formulation read:

$$
\begin{aligned}
\partial_t(\sqrt{\gamma}D) + \partial_j(f_D)^j &= 0 \,, \\
\partial_t(\sqrt{\gamma/\hat{\gamma}}S_i) + \partial_j(f_S)_i{}^j &= (s_S)_i + (f_S)_k{}^j\hat{\Gamma}^k_{ji} - (f_S)_i{}^k\hat{\Gamma}^j_{kj} + \alpha\sqrt{\gamma/\hat{\gamma}}(S_M)_i \,, \\
\partial_t(\sqrt{\gamma}\tau) + \partial_j(f_\tau)^j &= s_\tau - (f_\tau)^k\hat{\Gamma}^j_{jk} + \alpha\sqrt{\gamma}S_E \,, \\
\partial_t(\sqrt{\gamma}D_e) + \partial_j(f_{De})^j &= \alpha\sqrt{\gamma}S_N \,,
\end{aligned}
\tag{2.16}
$$

where the flux functions are given by:

$$
\begin{aligned}
(f_D)^j &\equiv \alpha\sqrt{\gamma}D(v^j - \beta^j/\alpha) \,, \\
(f_S)_i{}^j &\equiv \alpha e^{6\phi}\sqrt{\bar{\gamma}/\hat{\gamma}}\left(W^2\rho h v_i(v^j - \beta^j/\alpha) + p\delta_i{}^j\right) \,, \\
(f_\tau)^j &\equiv \alpha\sqrt{\gamma}\left(\tau(v^j - \beta^j/\alpha) + pv^j\right) \,, \\
(f_{De})^j &\equiv \alpha\sqrt{\gamma}D_e(v^j - \beta^j/\alpha) \,,
\end{aligned}
\tag{2.17}
$$

and the source functions are defined by:

$$
\begin{aligned}
(s_S)_i &\equiv \alpha e^{6\phi}\sqrt{\bar{\gamma}/\hat{\gamma}}\Big(-T^{00}\alpha\partial_i\alpha + T^0{}_k\hat{\mathcal{D}}_i\beta^k \\
&\quad + \frac{1}{2}(T^{00}\beta^j\beta^k + 2T^{0j}\beta^k + T^{jk})\hat{\mathcal{D}}_i\gamma_{jk}\Big) \,, \\
s_\tau &\equiv \alpha e^{6\phi}\sqrt{\bar{\gamma}/\hat{\gamma}}\Big(T^{00}(\beta^i\beta^j K_{ij} - \beta^i\partial_i\alpha) \\
&\quad + T^{0i}(2\beta^j K_{ij} - \partial_i\alpha) + T^{ij}K_{ij}\Big) \,.
\end{aligned}
\tag{2.18}
$$

The source terms S_E, $(S_M)_i$ and S_N express the change of gas energy, momentum, and lepton number, respectively, due to neutrino-matter interactions and will be quantified in Section 2.3.1. To close the system of equations, an equation of state is required that provides the pressure, temperature and composition as functions of the primitive variables. The hydrodynamics equations are solved using a finite difference Godunov-type High-Resolution-Shock-Capturing-Method (HRSC) (Toro, 2009). For the reconstruction of primitive variables at the cell interfaces, the PPM (Colella and Woodward, 1984), CENO (Liu and Osher, 1998) and MP5 (Suresh and Huynh, 1997) methods are implemented. The fluxes at cell interfaces are calculated

from primitive variables using the HLL Riemann solver (Harten, Lax, and Leer, 1983). The time integration is done with a second-order Runge-Kutta method, where the time step is the same as that used for integrating the BSSN equations (cf. equation (2.11)). The numerical implementation and test of the hydrodynamics part of the code is discussed in Montero, Baumgarte, and Müller (2014).

2.3 Neutrino transport

In this section we present the evolution equations used in our FLD neutrino transport scheme and their coupling to the evolution of the metric, eqs. (2.8), and of the hydrodynamic quantities, eqs. (2.16). The formalism of fully general relativistic truncated-moment schemes has been developed and extensively discussed in Shibata et al. (2011), Endeve, Cardall, and Mezzacappa (2012), and Cardall, Endeve, and Mezzacappa (2013), from who we adopt a great share of our notation. Like in the aforementioned works, all (comoving-frame and lab-frame) angular moments as well as the neutrino stress-energy tensor are expressed as functions of Eulerian (i.e. lab-frame) space-time coordinates, x^μ, and of the neutrino energy measured by a comoving observer, ϵ. One difference of our scheme to that of the aforementioned papers is, however, that we evolve the neutrino moments (i.e. the energy densities) as measured in the orthonormal comoving frame, instead of those measured in the lab frame. In that respect, our scheme is similar to that of Müller, Janka, and Dimmelmeier (2010).

2.3.1 Basic definitions

In terms of the neutrino distribution function, f, the comoving-frame 0th-, 1st-, and 2nd-order moments are given by[1]:

$$\mathcal{J}(x^\mu, \epsilon) \equiv \epsilon^3 \int f(x^\mu, p^{\hat{\imath}}) \, \mathrm{d}\Omega \,,$$

$$\mathcal{H}^{\hat{\imath}}(x^\mu, \epsilon) \equiv \epsilon^3 \int l^{\hat{\imath}} f(x^\mu, p^{\hat{\imath}}) \, \mathrm{d}\Omega \,,$$

$$\mathcal{K}^{\hat{\imath}\hat{\jmath}}(x^\mu, \epsilon) \equiv \epsilon^3 \int l^{\hat{\imath}} l^{\hat{\jmath}} f(x^\mu, p^{\hat{\imath}}) \, \mathrm{d}\Omega \,, \tag{2.19}$$

where $p^{\hat{\imath}} \equiv \epsilon(1, l^{\hat{\imath}})$ denotes the neutrino momentum-space coordinates, with unit momentum three-vector $l^{\hat{\imath}}$, and the angular integration is performed in the comoving-frame momentum space.

The comoving-frame moments in eqs. (2.19) are related to the monochromatic lab-frame neutrino stress-energy tensor, $\mathcal{T}_r^{ab}$, by

$$\mathcal{T}_r^{ab}(x^\mu, \epsilon) = L^a{}_{\hat{0}} L^b{}_{\hat{0}} \mathcal{J} + (L^a{}_{\hat{0}} L^b{}_{\hat{\imath}} + L^a{}_{\hat{\imath}} L^b{}_{\hat{0}}) \mathcal{H}^{\hat{\imath}}$$
$$+ L^a{}_{\hat{\imath}} L^b{}_{\hat{\jmath}} \mathcal{K}^{\hat{\imath}\hat{\jmath}} \,, \tag{2.20}$$

from which the corresponding energy-integrated tensor is obtained as

$$T_r^{ab}(x^\mu) = \int \mathcal{T}^{ab} \mathrm{d}\epsilon \,. \tag{2.21}$$

---

[1]We note that our definition of the comoving-frame moments is consistent with Shibata et al. (2011), but contains an additional factor ϵ^2 compared to those of Endeve, Cardall, and Mezzacappa (2012) and Cardall, Endeve, and Mezzacappa (2013).

In eq. (2.20), the matrices $L^a{}_{\hat{b}} \equiv e^a{}_{\bar{c}} \Lambda^{\bar{c}}{}_{\hat{b}}$ are responsible for transforming tensors from the orthonormal comoving frame to the global coordinate (i.e. lab) frame. Here, the Lorentz transformation, $\Lambda^{\bar{c}}{}_{\hat{b}}$, converts orthonormal comoving-frame quantities into an orthonormal (i.e. locally Minkowskian) tetrad basis in the lab frame, and the tetrad transformation $e^a{}_{\bar{c}}$ converts from the orthonormal lab-frame tetrad basis to the basis of global coordinates (which are generally not orthonormal in curved space-time).

The lab-frame moments of 0th-, 1st-, and 2nd-order are respectively given in terms of the comoving-frame moments by (cp. equations A18-A20 in Endeve, Cardall, and Mezzacappa 2012):

$$
\begin{aligned}
\mathcal{E}(x^\mu, \epsilon) &= W^2 \big(\mathcal{J} + 2\bar{v}_{\hat{i}} \mathcal{H}^{\hat{i}} + \bar{v}_{\hat{i}} \bar{v}_{\hat{j}} \mathcal{K}^{\hat{i}\hat{j}} \big), \\
\mathcal{F}^i(x^\mu, \epsilon) &= W \bigg[e^i_{\hat{i}} \mathcal{H}^{\hat{i}} + W v^i \mathcal{J} + e^i_{\hat{i}} \bar{v}_{\hat{j}} \mathcal{K}^{\hat{i}\hat{j}} \\
&\quad + \frac{W}{W+1} v^i \big\{ (2W+1) \bar{v}_{\hat{i}} \mathcal{H}^{\hat{i}} + W \bar{v}_{\hat{i}} \bar{v}_{\hat{j}} \mathcal{K}^{\hat{i}\hat{j}} \big\} \bigg], \\
\mathcal{S}^{ij}(x^\mu, \epsilon) &= e^i_{\hat{i}} e^j_{\hat{j}} \mathcal{K}^{\hat{i}\hat{j}} + W \big(v^i e^j_{\hat{j}} \mathcal{H}^{\hat{j}} + v^j e^i_{\hat{i}} \mathcal{H}^{\hat{i}} \big) + W^2 v^i v^j \mathcal{J} \\
&\quad + \frac{W^2}{W+1} \big(\big[v^i \bar{v}_{\hat{i}} e^j_{\hat{j}} + v^j \bar{v}_{\hat{j}} e^i_{\hat{i}} \big] \mathcal{K}^{\hat{i}\hat{j}} + 2W v^i v^j \bar{v}_{\hat{i}} \mathcal{H}^{\hat{i}} \big) \\
&\quad + \frac{W^4}{(W+1)^2} v^i v^j \bar{v}_{\hat{i}} \bar{v}_{\hat{j}} \mathcal{K}^{\hat{i}\hat{j}},
\end{aligned}
\tag{2.22}
$$

where $e^i_{\hat{i}} = e^i_{\hat{j}} \delta^{\bar{j}}_{\hat{i}}$ and $v^i \equiv e^i_{\hat{i}} \bar{v}^{\hat{i}}$, with $\bar{v}^{\hat{i}}$ being the three-velocity in the orthonormal tetrad basis. Using these lab-frame moments instead of the comoving-frame moments, the monochromatic lab-frame stress-energy tensor (cp. Eq. (2.20)) reads:

$$
\mathcal{T}_r^{ab}(x^\mu, \epsilon) = \mathcal{E} n^a n^b + \mathcal{F}^a n^b + \mathcal{F}^b n^a + \mathcal{S}^{ab}.
\tag{2.23}
$$

subsectionNeutrino interaction source terms The coupling between the transport equations and the equations of hydrodynamics and the Einstein equations is done as follows. We first compute the exchange rates of energy, momentum, and lepton number as measured in the orthonormal comoving frame:

$$
\begin{aligned}
Q_{\rm E} &\equiv -\sum_\nu \int d\epsilon\, \kappa_{\rm a} (\mathcal{J}^{\rm eq} - \mathcal{J}), \\
Q_{\rm M}^{\hat{i}} &\equiv \sum_\nu \int d\epsilon\, \kappa_{\rm t} \mathcal{H}^{\hat{i}}, \\
Q_{\rm N} &\equiv -m_{\rm u} \int d\epsilon \left[\left(\frac{\kappa_{\rm a}(\mathcal{J}^{\rm eq} - \mathcal{J})}{\epsilon} \right)_{\nu_e} - \left(\frac{\kappa_{\rm a}(\mathcal{J}^{\rm eq} - \mathcal{J})}{\epsilon} \right)_{\bar{\nu}_e} \right],
\end{aligned}
\tag{2.24}
$$

where

$$
\mathcal{J}^{\rm eq} \equiv \frac{4\pi\epsilon^3}{\exp((\epsilon - \mu_\nu)/T) + 1},
\tag{2.25}
$$

and $m_{\rm u}$, T, and μ_ν are the atomic mass unit, Boltzmann constant, fluid temperature, and neutrino chemical potential of the equilibrium distribution. In eqs. (2.24), the summation runs over all six neutrino species. To obtain the lab-frame source terms

S_E and $(S_M)_i$, we consider $q^{\hat{b}} \equiv (Q_E, Q_M^{\hat{i}})$ as four-vector, apply a Lorentz- and tetrad transformation, resulting in $s^a \equiv L_{\hat{b}}^a q^{\hat{b}}$, and perform the projections $S_E = -s^a n_a$ and $(S_M)_i = s^j \gamma_{ij}$ (see, e.g. Müller, Janka, and Dimmelmeier 2010; Cardall, Endeve, and Mezzacappa 2013). The lepton-number exchange rates, Q_N, are scalar and therefore frame invariant. We end up with:

$$
\begin{aligned}
S_E &= W(Q_E + \bar{v}_{\hat{i}} Q_M^{\hat{i}}) , \\
(S_M)_i &= e_{i\hat{i}} Q_M^{\hat{i}} + W(v_i - \beta_i/\alpha) Q_E \\
&\quad + W\left(\frac{W}{W+1} v_i - \beta_i/\alpha\right) \bar{v}_{\hat{i}} Q_M^{\hat{i}} , \\
S_N &= Q_N .
\end{aligned}
\tag{2.26}
$$

The neutrino contributions to the source terms for the Einstein equations (eqs. (2.26)) are obtained from the lab-frame neutrino angular moments (cf. eq. (2.22)) using eq. (2.23) as:

$$
\begin{aligned}
\rho_{\mathrm{r}} &= \sum_\nu \int \mathrm{d}\epsilon\, \mathcal{E} , \\
S_{\mathrm{r}}^i &= \sum_\nu \int \mathrm{d}\epsilon\, \mathcal{F}^i , \\
S_{\mathrm{r}}^{ij} &= \sum_\nu \int \mathrm{d}\epsilon\, \mathcal{S}^{ij} .
\end{aligned}
\tag{2.27}
$$

2.3.2   Energy equation and flux-limited diffusion approximation

The evolution equation for the comoving-frame neutrino energies, $\mathcal{J}$, can be derived from the evolution equations for the lab-frame moments, $\mathcal{E}$ and $\mathcal{F}^i$, which are discussed in Shibata et al. (2011), Endeve, Cardall, and Mezzacappa (2012), and Cardall, Endeve, and Mezzacappa (2013). We refer to Appendix A for the detailed derivation. The resulting evolution equation reads:

$$
\begin{aligned}
&\frac{1}{\alpha}\frac{\partial}{\partial t}\left[W(\hat{\mathcal{J}} + \bar{v}_{\hat{i}} \hat{\mathcal{H}}^{\hat{i}})\right] + \frac{1}{\alpha}\frac{\partial}{\partial x^j}\left[\alpha W(v^j - \beta^j/\alpha)\hat{\mathcal{J}}\right] + \\
&\frac{1}{\alpha}\frac{\partial}{\partial x^j}\left[\alpha e_{\hat{i}}^j \hat{\mathcal{H}}^{\hat{i}} + \alpha W\left(\frac{W}{W+1}v^j - \beta^j/\alpha\right)\bar{v}_{\hat{i}}\hat{\mathcal{H}}^{\hat{i}}\right] + \\
&\hat{R}_\epsilon - \frac{\partial}{\partial\epsilon}(\epsilon\hat{R}_\epsilon) = \kappa_a(\hat{\mathcal{J}}^{eq} - \hat{\mathcal{J}}) ,
\end{aligned}
\tag{2.28}
$$

where we use the notation $(\hat{\mathcal{J}}, \hat{\mathcal{J}}^{\mathrm{eq}}, \hat{\mathcal{H}}, \hat{\mathcal{K}}) \equiv \sqrt{\gamma}(\mathcal{J}, \mathcal{J}^{\mathrm{eq}}, \mathcal{H}, \mathcal{K})$. The terms subsumed in $R_\epsilon - \partial_\epsilon(\epsilon R_\epsilon)$ are responsible for spectral shifts in the energy-density distribution due to Doppler- and gravitational effects. They are functions of the comoving-frame moments by virtue of eqs. (A.14), (A.15), and (2.22). The specific shape of the neutrino source terms on the right-hand side of eq. (2.28) takes account of the fact that the current implementation is restricted to absorption and emission (or formally equivalent) reactions, and iso-energetic scattering processes. We denote the absorption opacity, scattering opacity, transport opacity, and equilibrium energy distribution as $\kappa_{\mathrm{a}}, \kappa_{\mathrm{s}}, \kappa_{\mathrm{t}} \equiv \kappa_{\mathrm{a}} + \kappa_{\mathrm{s}}$, and $\mathcal{J}^{\mathrm{eq}}$, respectively.

The flux-limited diffusion (FLD) approximation is implemented as follows. The flux density as measured in the orthonormal comoving frame, $\mathcal{H}^{\hat{i}}$, is in the diffusion limit approximately given by $\mathcal{H}^{\hat{i},\mathrm{diff}} = e^{k\hat{i}}\partial_k \mathcal{J}/(3\kappa_{\mathrm{t}})$. This expression can be obtained

from the evolution equation of the neutrino flux densities (shown, e.g., in eq. (A.9)), by neglecting time derivatives, velocity terms, and general relativistic corrections, which should all be subdominant. Going towards lower optical depths, radiation approaches the causality limit, i.e. $\mathcal{H}^{\hat{i},\text{free}} \approx \mathcal{J}$. In FLD, a smooth interpolation between these two regimes is accomplished by the use of a scalar flux-limiter, $\lambda \in [0, 1/3]$, in terms of which the flux is expressed as:

$$\mathcal{H}^{\hat{i}} \longrightarrow -D e^{k\hat{i}} \partial_k \mathcal{J} , \qquad (2.29)$$

where

$$D \equiv \frac{\lambda}{\kappa_t} \qquad (2.30)$$

is the (scalar) diffusion coefficient. In doing so, it is implicitly assumed that the partial time derivative of the flux vanishes, i.e. $\partial_t \mathcal{H}^{\hat{i}} = 0$. In this work, we use the Levermore-Pomraning (LP) limiter (Pomraning, 1981; Levermore and Pomraning, 1981) and the Wilson limiter (Bowers and Wilson, 1982), which are computed as:

$$\begin{aligned}
\lambda_{\text{LP}} &\equiv \frac{2 + R}{6 + 3R + R^2} , \\
\lambda_{\text{Wilson}} &\equiv \frac{1}{3 + R} ,
\end{aligned} \qquad (2.31)$$

where

$$R \equiv \frac{|e^{k\hat{i}} \partial_k \mathcal{J}|}{\kappa_t \mathcal{J}} \qquad (2.32)$$

is the Knudsen number and we use the flat metric tetrad $e^{k\hat{i}} = \text{diag}(1, 1/r, 1/(r \sin\theta))$ in eq. (2.32).

The Eddington tensor, χ^{ij}, which is related to the second moment tensor, $\mathcal{K}^{ij}$, by

$$\chi^{\hat{i}\hat{j}} = \frac{\mathcal{K}^{\hat{i}\hat{j}}}{\mathcal{J}} , \qquad (2.33)$$

is in the FLD approximation given by (see, e.g. Pomraning 1981; Levermore and Pomraning 1981; Swesty and Myra 2009):

$$\chi^{\hat{i}\hat{j}} = \frac{1}{2}[(1 - \chi)\delta^{\hat{i}\hat{j}} + (3\chi - 1)h^{\hat{i}}h^{\hat{j}}] , \qquad (2.34)$$

where $h^{\hat{i}}$ is the unit vector along $\mathcal{H}^{\hat{i}}$ and the (scalar) Eddington factor, χ, is given by

$$\chi = \lambda + (\lambda R)^2 . \qquad (2.35)$$

For future reference, we also define the flux factor as

$$f^{\hat{i}} \equiv \frac{\mathcal{H}^{\hat{i}}}{\mathcal{J}} . \qquad (2.36)$$

The final FLD equation solved in our code reads:

$$
\begin{aligned}
&\frac{1}{\alpha}\frac{\partial}{\partial t}(W\hat{\mathcal{J}}) + \frac{1}{\alpha}\frac{\partial}{\partial x^j}[\alpha W(v^j - \beta^j/\alpha)\hat{\mathcal{J}}] - \\
&\frac{1}{\alpha}\frac{\partial}{\partial x^j}\Big[\alpha\sqrt{\gamma}\Big\{\gamma^{jk} + W\Big(\frac{W}{W+1}v^j - \beta^j/\alpha\Big)v^k\Big\}D\partial_k\mathcal{J}\Big] - \\
&\frac{1}{\alpha}\frac{\partial}{\partial t}(W\sqrt{\gamma}\bar{v}_{\hat{\imath}})De^{k\hat{\imath}}\partial_k\mathcal{J} + R_\epsilon - \frac{\partial}{\partial\epsilon}(\epsilon R_\epsilon) \\
&= \kappa_{\mathrm{a}}(\hat{\mathcal{J}}^{eq} - \hat{\mathcal{J}})\,.
\end{aligned}
\tag{2.37}
$$

The second, third and fourth terms in the above equation describe advection, diffusion, and aberration due to fluid acceleration, respectively. We simplify the equation by neglecting all spatial cross derivatives, which appear due to off-diagonal metric components $\gamma^{r\theta}, \gamma^{r\phi}$ and $\gamma^{\theta\phi}$. Since these off-diagonal components are typically strongly subdominant compared to the diagonal components, the corresponding error should remain small.

2.4   Numerical treatment of the transport

In this section, we describe the numerical method used to solve the neutrino transport equations together with the Einstein and hydrodynamics equations. The neutrino energy space is discretized into energy groups, and for each of these and for each neutrino species we solve the evolution equation for $\mathcal{J}$, eq. (2.37), which generally depends on three spatial dimensions. We use finite-difference methods for the spatial discretization on the same spatial grid as for the GR and hydrodynamics steps.

   The flow chart of our evolution algorithm is depicted in Fig. 2.1. After advancing the GR and hydrodynamics equations by one integration step, we calculate the opacity using updated hydrodynamics quantities as well as transport quantities from the previous time step. Next, we evolve the neutrino energy densities. During the transport steps, all hydrodynamics and GR quantities are kept fixed. Since the FLD equations are generally parabolic and the propagation speed of information is in principle infinity, many existing FLD codes employ a fully implicit time integration. However, with the computational cost roughly increasing with the number of grid points to the third power, unsplit, fully implicit integration schemes become particularly expensive in multi-dimensional applications, and they tend to scale poorly on large numbers of computational cores. In the present scheme we avoid this inconvenience by using operator splitting and treating parts of the equation explicitly. In the following subsections, we first estimate the relevant timescales to motivate the time-integration steps, and then we present the detailed discretization procedure employed at each step.

   For the calculation of the diffusion coefficient and the Eddington scalar and tensor, we follow Swesty and Myra (2009) (see their Appendix H.4). In particular, we compute a flux-limiter, $\lambda(R)$, and diffusion constant, D, separately for each coordinate direction. In what follows D_1, D_2, D_3 will denote the diffusion coefficients in the radial, polar, and azimuthal coordinate direction, respectively.

2.4.1   Relevant timescales and motivation of the integration scheme

Using simple dimensional estimates, we first identify the characteristic timescales on which the different terms in the FLD equation induce a change of $\mathcal{J}$. We denote
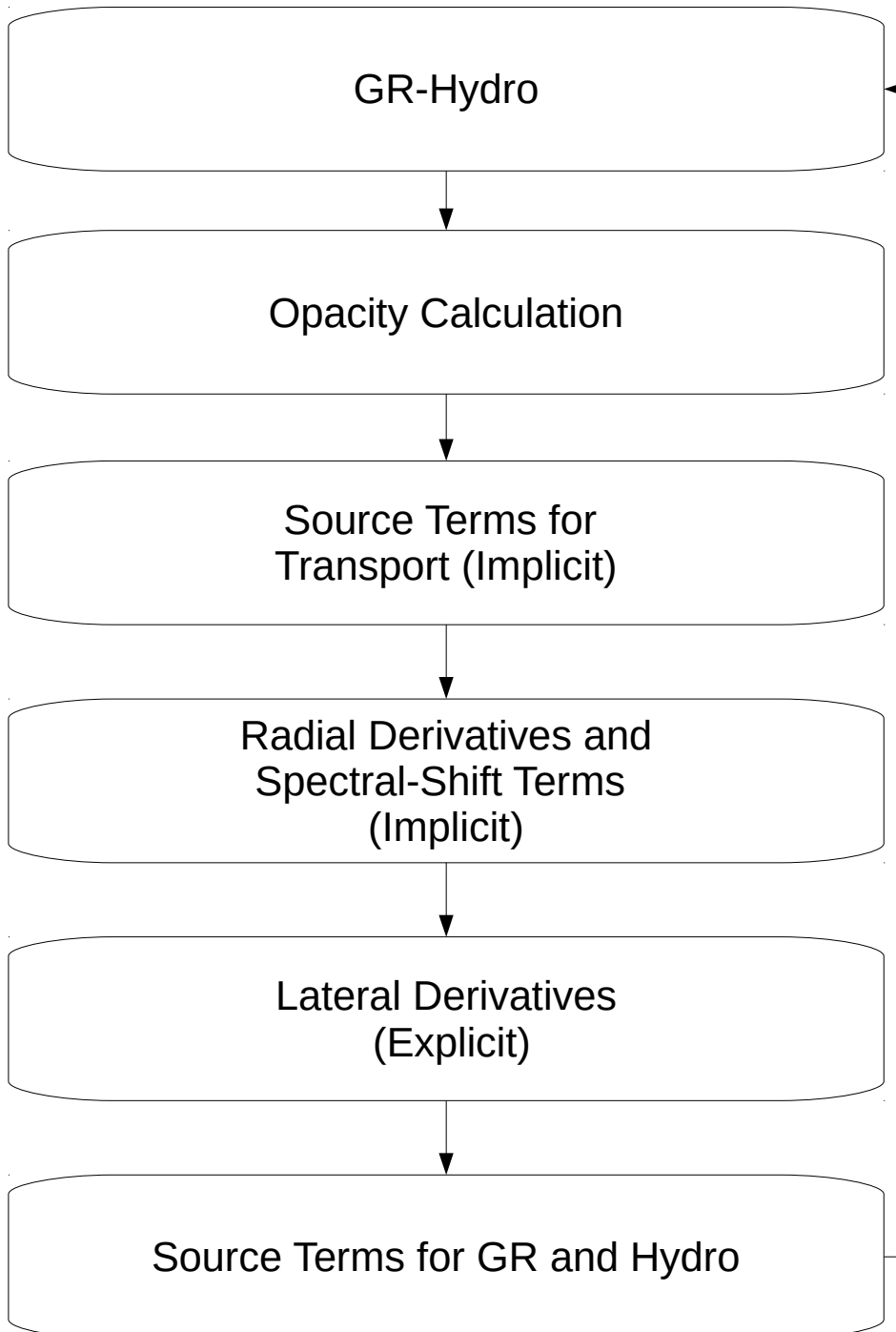
GR-Hydro

Opacity Calculation

Source Terms for
Transport (Implicit)

Radial Derivatives and
Spectral-Shift Terms
(Implicit)

Lateral Derivatives
(Explicit)

Source Terms for GR and Hydro

FIGURE 2.1: Flow Chart of transport algorithm.

the grid spacing for simplicity by Δx, keeping in mind that this quantity generally depends on the grid location. For clarity, in this section we explicitly include the speed of light, c.

Ignoring the energy derivatives, the FLD equation, eq. (2.37), is an advection-diffusion-reaction equation (e.g. Anderson, 2011). The velocity-dependent terms of eq. (2.37) are in this sense advection terms, the characteristic timescale of which is bounded from below by the light-crossing time of a grid cell,

$$t_{\text{light}} \quad = \quad \frac{\Delta x}{\text{c}}. \tag{2.38}$$

The reaction (i.e. neutrino source) terms are associated with timescales

$$t_{\text{source}} \quad = \quad \frac{1}{\text{c}\kappa_{\text{a}}} \tag{2.39}$$

that are typically much shorter than t_{light} inside a hot PNS and practically infinity far away from any neutrino sources. Finally, the characteristic timescale of the FLD-related terms can be estimated by

$$t_{\text{diff}} \quad = \quad \frac{\Delta x^2}{D}. \tag{2.40}$$

The timescale that is actually used for the integration, Δt, is according to eq. (2.11) always less than or equal to the light-crossing timescale of a grid cell, i.e. $\Delta t \lesssim t_{\text{light}}$. A useful quantity for assessing stability regimes of advection-diffusion equations is

$$r_{\text{diff}} \quad \equiv \quad \frac{\Delta t}{t_{\text{diff}}}, \tag{2.41}$$

in terms of which the condition for numerical stability is $r_{\text{diff}} \lesssim 0.5 - 1$ for conventional explicit integration schemes. Assuming $\Delta t \sim t_{\text{light}}$ and recalling that λ and $\kappa_{\text{t}}\Delta x$ denote the flux-limiter and the optical depth per grid cell, respectively, we can use

$$r_{\text{diff}} \quad \sim \quad \frac{\lambda}{\kappa_{\text{t}}\Delta x} \tag{2.42}$$

to obtain a crude estimate of r_{diff} for the (simplified) case of constant grid width of $\Delta x \sim \mathcal{O}(100\,\text{m})$: Inside the hot PNS we have $\lambda \approx 1/3$ and $\kappa_{\text{t}}\Delta x \gg 1$, and therefore we expect $r_{\text{diff}} \ll 1$. Far away from any neutrino source the Knudsen number roughly scales as $R \sim (\kappa_{\text{t}}\Delta x)^{-1}$, giving $\lambda \sim R^{-1} \sim \kappa_{\text{t}}\Delta x$ and hence $r_{\text{diff}} \sim \mathcal{O}(1)$. However, values of r_{diff} greater than the aforementioned limits can in principle still be achieved in the semi-transparent regime and for more complicated grid geometries.

Motivated by these time-step considerations, we decompose eqs. (2.37) into three parts and integrate each part in its own operator-split step: In the first step, we integrate the neutrino source terms implicitly using a Newton-Raphson scheme. Then we solve for the contributions from the radial derivatives and the spectral-shift terms (i.e. $R_\epsilon - \partial_\epsilon(\epsilon R_\epsilon)$) using an implicit Crank-Nicolson scheme. Finally, we obtain the contribution from the non-radial derivatives using the explicit Allen-Cheng method. Although this method is explicit, it remains stable for any value of r_{diff}; see Sect. **??** for exemplary tests and, e.g., Anderson (2011) for detailed comparisons with other methods. While the gain of using an explicit compared to an implicit scheme for this

step is an improvement in efficiency and scalability, the trade-off is some loss of accuracy at high values of $r_{\text{diff}} \gtrsim 1$. However, tests indicate (cf. Fig. 3.7 and the corresponding discussion in Sect. 3.3) that in the CCSN problem high values of $r_{\text{diff}} \gtrsim 0.5$ tend to appear only close to shock, where lateral neutrino fluxes are subdominant compared to radial fluxes.

2.4.2 Neutrino source terms

In the first step, we compute the contribution from the neutrino source terms in an implicit manner. We solve the following equations:

$$
\begin{aligned}
\frac{W}{\alpha}\partial_t \mathcal{J}_{\nu,\xi} &= \left[\kappa_a(\mathcal{J}^{\text{eq}} - \mathcal{J})\right]_{\nu,\xi}, \\
\frac{W}{\alpha}\rho\partial_t e(T, Y_e) &= -\sum_{\nu,\xi}\left[\kappa_a(\mathcal{J}^{\text{eq}} - \mathcal{J})\Delta\epsilon_\xi\right]_{\nu,\xi}, \\
\frac{W}{\alpha}\rho\partial_t Y_e &= -m_u\sum_\xi\left[\left[\kappa_a(\mathcal{J}^{\text{eq}} - \mathcal{J})\Delta\epsilon_\xi\right]_{\nu_e}\right. \\
&\quad\left. -\left[\kappa_a(\mathcal{J}^{\text{eq}} - \mathcal{J})\Delta\epsilon_\xi\right]_{\bar{\nu}_e}\right]_\xi.
\end{aligned}
\tag{2.43}
$$

The subscripts ν and ξ indicate the neutrino species and energy bin, respectively, and $\Delta\epsilon_\xi$ is the width of the energy bin centered at ϵ_ξ.

We discretize eq. (2.43) in time employing a backward Euler scheme and solve the resulting system of equations for the neutrino energy densities, $\mathcal{J}_{\nu,\xi}$, temperature, T and electron fraction, Y_e, using the Newton-Raphson method. We keep α, W, ρ, and κ_a constant during this step at values obtained after the GR-hydro step. The Jacobian of eq. (2.43) is determined numerically, and a direct matrix from the LAPACK library (Anderson et al., 1999) is used for inverting the Jacobian. The values of neutrino energy densities, $\mathcal{J}_{\nu,\xi}$, obtained in this step are used as initial values in the next step.

2.4.3 Radial derivatives and spectral-shift terms

In the next operator-split step, the following equation is solved:

$$
W\partial_t \hat{\mathcal{J}} + \mathcal{R}_r = 0,
\tag{2.44}
$$

where

$$
\begin{aligned}
\mathcal{R}_r &\equiv \partial_t(W)\hat{\mathcal{J}} + \partial_r[\alpha W(v^r - \beta^r/\alpha)\hat{\mathcal{J}}] - \\
&\partial_r\left[\alpha\sqrt{\gamma}\left\{\gamma^{rr} + W\left(\frac{W}{W+1}v^r - \beta^r/\alpha\right)v^r\right\}D_1\partial_r\mathcal{J}\right] - \\
&\partial_t(W\sqrt{\gamma}\bar{v}_{\hat{i}})De^{r\hat{i}}\partial_r\mathcal{J} + \alpha\left[\hat{R}_\epsilon - \frac{\partial}{\partial\epsilon}(\epsilon\hat{R}_\epsilon)\right].
\end{aligned}
\tag{2.45}
$$

contains the radial advection and diffusion terms, the radial acceleration term, and the spectral-shift terms. Equation (2.44) is integrated by using the implicit Crank-Nicolson method. The old time is denoted as t^n and the new time as t^{n+1}. The time indices for all GR and hydrodynamics quantities are omitted as they are kept fixed in all transport steps. Using superscripts n and $n + 1$ to label quantities defined before

and after this partial integration step, respectively, the discretized equation reads:

$$(W\sqrt{\gamma})\frac{\mathcal{J}_i^{n+1} - \mathcal{J}_i^n}{\Delta t} = \frac{1}{2}(\mathcal{R}_{r,i}^{n+1} + \mathcal{R}_{r,i}^n) \,. \tag{2.46}$$

Here, $\Delta t \equiv t^{n+1} - t^n$ and i denotes quantities measured at the cell center in the radial direction. In the following, we describe the constituents of $\mathcal{R}_{r,i}^{n+1}$, while the corresponding expressions for $\mathcal{R}_{r,i}^n$ are obtained by replacing $n + 1$ with n. For simplicity, we assume a uniform radial grid with constant cell size Δr; the generalization to non-uniform grids is straightforward.

The diffusion term is spatially discretized as:

$$\left[\partial_r(A^r D_1 \partial_r \mathcal{J})\right]^{n+1} = \frac{1}{\Delta r}\left[A_{i+1/2}^r D_{1,i+1/2}^n \frac{\mathcal{J}_{i+1}^{n+1} - \mathcal{J}_i^{n+1}}{\Delta r} \right.$$
$$\left. - A_{i-1/2}^r D_{1,i-1/2}^n \frac{\mathcal{J}_i^{n+1} - \mathcal{J}_{i-1}^{n+1}}{\Delta r}\right], \tag{2.47}$$

where

$$A^r \equiv \alpha\sqrt{\gamma}\left\{\gamma^{rr} + W\left(\frac{W}{W+1}v^r - \beta^r/\alpha\right)v^r\right\} \,. \tag{2.48}$$

Indices $i + 1/2$ and $i - 1/2$ denote the right and left cell interface of the i-th cell, respectively. If not mentioned otherwise, all cell interface values of hydrodynamic quantities and metric terms (contained in A^r and in other terms below) are calculated by linear interpolation of the cell centered values.

The fluid-acceleration term (fourth term in eq. (2.45)) is computed as:

$$\left[B^r D \partial_r \mathcal{J}\right]^{n+1} = \frac{B_i^r}{2}\left[D_{1,i+1/2}^n \frac{\mathcal{J}_{i+1}^{n+1} - \mathcal{J}_i^{n+1}}{\Delta r} \right.$$
$$\left. + D_{1,i-1/2}^n \frac{\mathcal{J}_i^{n+1} - \mathcal{J}_{i-1}^{n+1}}{\Delta r}\right], \tag{2.49}$$

where

$$B^r \equiv \partial_t(W\sqrt{\gamma}\bar{v}_{\hat{\imath}})e^{r\hat{\imath}} \,. \tag{2.50}$$

The time derivative in eq. (2.50) is calculated using values of the hydrodynamic and metric quantities before and after the initial GR-hydro step.

The advection term is discretized using an upwind-type method (see, e.g. A. Dorfi 1998; Rampp and Janka 2002) as:

$$\left[\partial_r(C^r \mathcal{J})\right]^{n+1} = \frac{1}{\Delta r}\left[C_{i+1/2}^r \mathcal{J}_{\iota(i+1/2)}^{n+1} - C_{i-1/2}^r \mathcal{J}_{\iota(i-1/2)}^{n+1}\right], \tag{2.51}$$

where

$$C^r \equiv \alpha\sqrt{\gamma}W(v^r - \beta^r/\alpha) \tag{2.52}$$

and

$$\iota(i + 1/2) \equiv \begin{cases} i, & \text{if } v_{i+1/2}^r > 0 \,, \\ i + 1, & \text{otherwise} \,. \end{cases} \tag{2.53}$$

The spectral-shift term, $R_\epsilon - \partial_\epsilon(\epsilon R_\epsilon)$, is discretized using the number-conservative scheme developed in Müller, Janka, and Dimmelmeier (2010). The terms with $\mathcal{H}^{\hat{j}}$ and $\mathcal{K}^{\hat{i}\hat{j}}$ that appear in R_ϵ are replaced by $f^{\hat{j}}\mathcal{J}$ and $\chi^{\hat{i}\hat{j}}\mathcal{J}$, respectively, and the flux factor, $f^{\hat{j}}$, and Eddington tensor, $\chi^{\hat{i}\hat{j}}$, are defined at instance t^n, while only $\mathcal{J}$ is defined at t^{n+1}.

The Crank-Nicolson method requires to solve a linear system of equations. Direct methods for solving linear systems are relatively expensive, we therefore use the iterative "Generalized Minimal Residual Method with Restart" (GMRES) along with the incomplete LU decomposition as a preconditioner from the NAG library[2] for this purpose. The values of neutrino energy densities, $\mathcal{J}$, obtained in this step are used as initial values in the next step.

2.4.4 Non-radial derivatives

Finally, we include the contribution from the remaining lateral advection and diffusion terms by integrating the equation

$$\partial_t(W\hat{\mathcal{J}}) + \partial_\theta[\alpha W(v^\theta - \beta^\theta/\alpha)\hat{\mathcal{J}}] + \partial_\phi[\alpha W(v^\phi - \beta^\phi/\alpha)\hat{\mathcal{J}}] +$$
$$\partial_\theta\left[\alpha\sqrt{\gamma}\left\{\gamma^{\theta\theta} + W\left(\frac{W}{W+1}v^\theta - \beta^\theta/\alpha\right)v^\theta\right\}D_2\partial_\theta\mathcal{J}\right] +$$
$$\partial_\phi\left[\alpha\sqrt{\gamma}\left\{\gamma^{\phi\phi} + W\left(\frac{W}{W+1}v^\phi - \beta^\phi/\alpha\right)v^\phi\right\}D_3\partial_\phi\mathcal{J}\right] = 0 \qquad (2.54)$$

using the explicit Allen-Cheng method (Allen, 1970), where D_2 and D_3 are the diffusion coefficients in polar and azimuthal direction, respectively.

The discretized version of eq. (2.54) is presented below exemplarily for a single dimension (representative of the θ- or ϕ-direction) and a uniform grid, whose points are labeled by k and spaced apart by Δy. The method consists of two steps, a predictor step and a corrector step. We again use n and $n+1$ to label quantities before and after the two substeps. The value of $\mathcal{J}$ obtained after the predictor step, $\mathcal{J}^*$, is used in the corrector step to determine $\mathcal{J}^{n+1}$. The predictor step is given by

$$\frac{(W\sqrt{\gamma})^n}{\Delta t}(\mathcal{J}_k^* - \mathcal{J}_k^n) = -\frac{1}{2\Delta y}(F_{k+1}\mathcal{J}_{k+1}^n - F_{k-1}\mathcal{J}_{k-1}^n)$$
$$+\frac{1}{\Delta y^2}(E_{k+1/2}(\mathcal{J}_{k+1}^n - \mathcal{J}_k^*) - E_{k-1/2}(\mathcal{J}_k^* - \mathcal{J}_{k-1}^n)) \qquad (2.55)$$

and the corrector step by

$$\frac{(W\sqrt{\gamma})^n}{\Delta t}(\mathcal{J}_k^{n+1} - \mathcal{J}_k^n) = -\frac{1}{2\Delta y}(F_{k+1}\mathcal{J}_{k+1}^* - F_{k-1}\mathcal{J}_{k-1}^*)$$
$$+\frac{1}{\Delta y^2}(E_{k+1/2}(\mathcal{J}_{k+1}^* - \mathcal{J}_k^{n+1}) - E_{k-1/2}(\mathcal{J}_k^{n+1} - \mathcal{J}_{k-1}^*)), \qquad (2.56)$$

where we defined

$$F = \alpha\sqrt{\gamma}W(v^j - \beta^j/\alpha),$$
$$E = \alpha\sqrt{\gamma}\left\{\gamma^{jj} + W\left(\frac{W}{W+1}v^j - \beta^j/\alpha\right)v^j\right\}D, \qquad (2.57)$$

---

[2]www.nag.co.uk

with j denoting the considered direction, θ or ϕ. The values $\mathcal{J}^{n+1}$ obtained in this step are the final values at the new time t^{n+1}. These values are used to calculate the neutrino source terms for the hydrodynamics equations (cf. eqs. (2.26) and for the metric equations (2.27) which are used in the next GR-Hydro step.

2.4.5 Boundary conditions

For our spherical polar coordinate system, we use the standard boundary conditions in angular directions, namely reflecting boundary conditions in polar direction and periodic boundary conditions in azimuthal direction. For the outer radial boundary, we typically use the "free" boundary condition, meaning that the flux is set according to free-streaming conditions, $D\partial_r \mathcal{J} = \mathcal{J}$. For the inner radial boundary, the user may choose a "flat" boundary condition, given by $D\partial_r \mathcal{J} = 0$, or a "fixed" boundary condition, for which $\mathcal{J}$ is set to some predefined value.

Chapter 3

Test Problems

In this section, we discuss various setups for testing and validating the transport scheme. In Sects. 3.1 and 3.2, we will consider 1D and 2D tests with simplified radiation-matter interactions, and in Sect. 3.3 we examine fully dynamic 1D core-collapse supernova simulations with a microphysical equation of state and realistic neutrino-matter interactions. For future reference, we define the L1 and L2 error norm as

$$
\begin{aligned}
\text{L1} - \text{error} &\equiv \frac{1}{N} \sum_i \frac{|\mathcal{J}_i^{\text{num}} - \mathcal{J}_i^{\text{an}}|}{\mathcal{J}_i^{\text{an}}} \,, \\
\text{L2} - \text{error} &\equiv \frac{1}{N} \sqrt{\sum_i \left(\frac{\mathcal{J}_i^{\text{num}} - \mathcal{J}_i^{\text{an}}}{\mathcal{J}_i^{\text{an}}} \right)^2} \,,
\end{aligned}
\tag{3.1}
$$

where the sums run over all N grid cells, and $\mathcal{J}^{\text{num}}$ and $\mathcal{J}^{\text{an}}$ denote the numerical and analytical solution for the radiation energy density, respectively.

3.1 1D test problems

We first consider 1D toy-model problems, namely the diffusion of a Gaussian pulse and a differentially expanding isothermal atmosphere.

3.1.1 Diffusion of Gaussian pulse with Crank-Nicolson

We set up a well-known test problem consisting of a Gaussian-shaped pulse of radiation that diffuses through a medium with constant scattering opacity, κ_{s}. The problem is chosen to test the basic working capability of the code, in particular the correct implementation of the implicit Crank-Nicolson method used for the radial diffusion terms. Diffusion of a Gaussian-shaped pulse with constant scattering opacity has the analytical solution (e.g. Swesty and Myra, 2009; Kuroda, Takiwaki, and Kotake, 2016):

$$
\mathcal{J}^{\text{an}}(\tilde{r}) = \left(\frac{\kappa_{\text{s}}}{t} \right)^{d/2} \exp \left(\frac{-3\kappa_{\text{s}}\tilde{r}^2}{4t} \right)
\tag{3.2}
$$

in $d = 1, 2, 3$ dimensions, where $\tilde{r}$ is the distance to the center of the pulse. In the present 1D case, a constant scattering opacity of $\kappa_{\text{s}} = 10^3$ is used. The pulse is initialized at time $t = 10^{-9}$ such that its peak coincides with the center of our computational domain, which has a total length of 2. In our spherical polar coordinate system, we mimic the 1D Cartesian grid by locating the computational domain at some very large radius $r \sim 10^4$. The domain is divided into $N = \{128, 256, 512\}$ cells

TABLE 3.1: Gaussian pulse test using the implicit Crank-Nicolson method (cf. Sect. 3.1.1). For each CFL factor and grid resolution the L2-error is given together with the ratio of the current L2-error to that resulting with half the resolution. The L2-error decreases quadratically with the number of grid points, consistent with the 2nd-order accuracy of the Crank-Nicolson method.

CFL	resolution, N	L2 error	error ratio
1.0	128	0.258	
	256	0.054	4.751
	512	0.013	4.023
10.0	128	0.259	
	256	0.055	4.711
	512	0.013	4.062

TABLE 3.2: Gaussian pulse test using the explicit Allen-Cheng method (cf. Sect. 3.1.2). For each value of r_{diff} the L2-error is given together with the ratio of the current L2-error to that resulting with twice the value of r_{diff}. The L2-error decreases linearly with r_{diff}, consistent with the 1st-order temporal accuracy of the Allen-Cheng method.

r_{diff}	resolution, N	L2 error	error ratio
1.6	200	0.0583	
0.8	200	0.0359	1.623
0.4	200	0.0206	1.742
0.2	200	0.0089	2.314
0.1	200	0.0037	2.405

and a single radiation energy bin is evolved. We employ a "flat" boundary condition for the inner boundary and a "free" boundary condition for the outer boundary, following Swesty and Myra (2009). We consider two choices for the CFL value (cp. eq. (2.11)), 1 and 10. The problem is stopped at $t = 2 \times 10^{-9}$. In Table 3.1, the L2-error and the ratio of the L2-error for two consecutive resolutions are shown. We obtain a second-order accuracy for both CFL values, which is in agreement with the formal accuracy of the Crank-Nicolson Method. The test confirms the basic functionality of the code and validates the correct implementation of the Crank-Nicolson scheme used for the diffusion terms.

3.1.2 Diffusion of Gaussian pulse with Allen-Cheng

As described in Sect. 2.4, we use the implicit Crank-Nicolson scheme only for the radial diffusion and advection terms, while for all lateral terms we employ the explicit Allen-Cheng method. In this test problem, we want to check if the Allen-Cheng method is implemented correctly and produces reasonable results, and if it remains stable at conditions where conventional explicit schemes crash.

The setup is similar as in Sect. 3.1.1, except now we use a diffusion coefficient of $D = 10^{-3}$, a single resolution of 200 points, and we evolve the problem from time $t = 1$ to $t = 2$. The only characteristic timescale of this problem is the diffusion timescale $t_{\text{diff}} = \Delta x^2/D$, hence the performance of the integration method can be characterized entirely by the ratio $r_{\text{diff}} = \Delta t/t_{\text{diff}}$, where Δt is the employed time step. We conduct several simulations varying the value of r_{diff} by changing Δt.

As can be seen in Table 3.2, the L2-error decreases roughly linearly with decreasing time step in agreement with the formal temporal accuracy of the Allen-Cheng method. Moreover, the test demonstrates that for $r_{\text{diff}} > 0.5$ the Allen-Cheng method
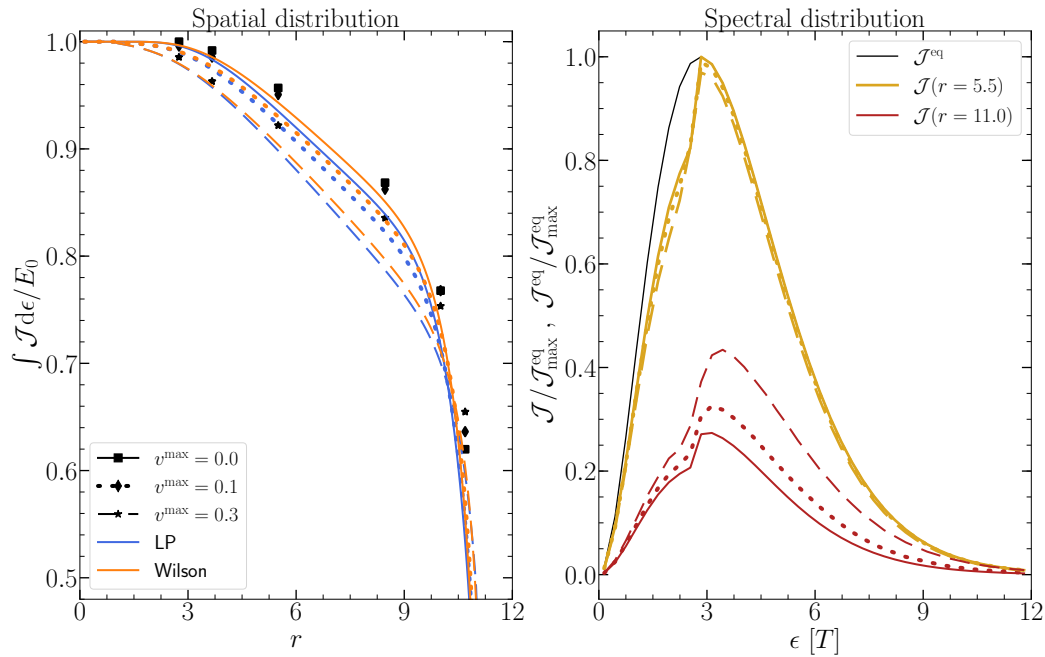
FIGURE 3.1: Differentially expanding atmosphere (cf. Sect. 3.1.3). In the left plot, the energy-integrated energy density, $E(r) \equiv \int \mathcal{J}(r,\epsilon)\, \mathrm{d}\epsilon$, normalized by $E_0 = \int \mathcal{J}(r = 0,\epsilon)\, \mathrm{d}\epsilon$ is shown against radius for $v^{\mathrm{max}} = 0$ (solid lines), 0.1 (dotted lines), 0.3 (dashed lines), where blue (orange) lines denote solutions obtained with the LP (Wilson) flux-limiter. The markers show the reference solution by Mihalas (1980). In the right plot, the radiation spectra, normalized by the maximum of equilibrium distribution function, $\mathcal{J}_{\mathrm{max}}^{\mathrm{eq}}$, resulting with the Wilson limiter are plotted at radius $r = 5.5$ (golden lines) and 11 (red lines), together with the equilibrium distribution function (see eq. (3.5), normalized by $\mathcal{J}_{\mathrm{max}}^{\mathrm{eq}}$) at a temperature of $T = 1$ (black line).

indeed remains stable, and that, as expected, the accuracy decreases for higher values of r_{diff}. In Sect. 3.2.2, we will consider a similar test in two dimensions.

We compared the computing time required for solving this 1D test problem by the Crank-Nicolson and the Allen-Cheng method. We see that the Allen-Cheng method is two times faster than the Crank-Nicolson method with out any parallelization. The Crank-Nicolson method requires solving of the system of linear equations by an iterative method. Since our code is MPI parallel, the iterative method requires several collective communication[1] per iteration. The number of iterations needed for the convergence of the iterative solver depends on the size of the system of linear equations. On the other hand, the Allen-Cheng method only requires one point to point communication per time step. As a result, the Allen-Cheng method has better parallel efficiency.

3.1.3 Differentially expanding atmosphere

Next, we consider a differentially expanding, isothermal atmosphere in spherical symmetry having a temperature of $T = 1$ (Mihalas, 1980; Rampp and Janka, 2002; Just, Obergaulinger, and Janka, 2015) in order to check the correct implementation of the energy-bin coupling and velocity-dependent terms in our code. The velocity

---

[1] see, e.g. https://computing.llnl.gov/tutorials/mpi/

profile is given by

$$v_r(r) = v^{\max} \frac{r - r_{\min}}{r_{\max} - r_{\min}} \ . \tag{3.3}$$

in the region $[r_{\min}, r_{\max}]$ and by $v_r = 0$ elsewhere. We consider three cases with $v^{\max} = \{0.0, 0.1, 0.3\}$. The radius- and energy-dependent absorption opacity is given by:

$$\kappa_{\mathrm{a}} = \begin{cases} \frac{10a}{r^2} \exp\left(-\frac{(\epsilon - \epsilon_0)^2}{\Delta^2}\right) + \frac{a}{r^2}\left(1 - \exp\left(-\frac{(\epsilon - \epsilon_0)^2}{\Delta^2}\right)\right) & , \ \epsilon \leq \epsilon_0 \ , \\ \frac{10a}{r^2} & , \ \epsilon > \epsilon_0 \ , \end{cases} \tag{3.4}$$

and the equilibrium distribution by:

$$\mathcal{J}^{\mathrm{eq}} = \frac{8\pi\epsilon^3}{\exp(\epsilon/T) - 1} \ . \tag{3.5}$$

Here, k_{b} is the Boltzmann constant, respectively. The parameters in the aforementioned prescriptions are given by $\{r_{\min}, r_{\max}, \epsilon_0, \Delta, a\} = \{1.0, 11.0, 3.0\, T, 0.2\, T, 10.9989\}$. We use 400 grid points to discretize the simulation domain within $[0.1, 15]$, and employ 40 energy bins to cover the radiation energy range $[0, 11.8\, T]$. At $r = 0.1$ the "flat" boundary condition is applied and at $r = 15$ the free-streaming boundary condition. Each simulation is performed using a CFL value of 0.5 and is stopped once stationarity is reached. We perform a simulation for each of the three values of $v^{\max}$ as well as for both the LP and the Wilson limiter (cf. eqs. (2.31).

In the left plot of Fig. 3.1 we show radial profiles of the energy-integrated radiation energy density in the comoving frame, $E(r) \equiv \int \mathcal{J}(r, \epsilon)\, \mathrm{d}\epsilon$, normalized by $E_0 = \int \mathcal{J}^{\mathrm{eq}}(r = 0, \epsilon)\, \mathrm{d}\epsilon$. In agreement with the reference solution (taken from Mihalas, 1980 and indicated by markers), E shows a gradual decrease with growing expansion velocities at a given radius $r \lesssim 10$, which is because of Doppler redshifting in the comoving frame. At higher radii, $r \gtrsim 10$, cases with higher velocities show, again in agreement with the reference solution, higher values of E, mainly due the cumulative effect of reduced absorption rates in the underlying layers where E is reduced.

We notice that radiation in the FLD solutions departs from equilibrium and transitions into free-streaming conditions at somewhat lower radii than radiation in the reference solution. However, the L1-error of the FLD solution with respect to the reference solution is still rather small, namely 4% for the LP limiter and 3% for the Wilson limiter. In this test, the Wilson limiter reproduces the reference solution slightly better than the LP limiter.

In the right plot of Fig. 3.1, the radiation energy density spectra, normalized by the maximum of equilibrium distribution function, $\mathcal{J}^{\mathrm{eq}}_{\max}$, are shown at radii $r = 5.5$ and 11.0, representative of optically thick and thin conditions, respectively, along with the equilibrium spectrum at $r = 5.5$. The jump in the spectra is associated with the jump in the absorption opacity at energy $\epsilon = \epsilon_0$. Due to radiation being redshifted on its way to the surface, the jump in the spectra around ϵ_0 is smeared out, all the more for higher values of $v^{\max}$.

The good results of this test prove that our FLD code can handle the transition of radiation from diffusion to free-streaming, and they indicate that the velocity-dependent terms describing Doppler effects are implemented properly.
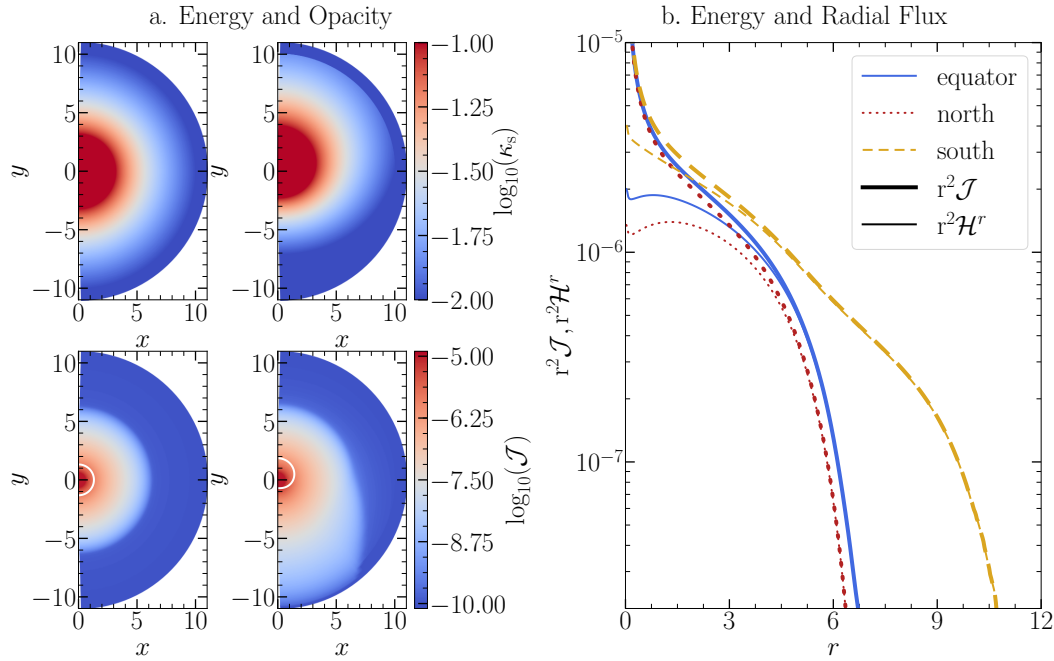
FIGURE 3.2: Hemispheric difference test (cf. Sect. 3.2.1). Panel (a): The top (bottom) row shows color mappings of the logarithm of the scattering opacity (radiation energy density). The left (right) plots are for the case of spherically symmetric (dipole-shaped) opacity profiles. The angle-dependent locations r_0, at which the optical depth $\tau(r_0, \theta) = -\int_\infty^{r_0} \kappa_s(r, \theta) dr$ reaches $2/3$, are marked by white lines in the bottom plots. (b) The $r^2\mathcal{J}$ (thick lines) and $r^2\mathcal{H}^r$ (thin lines) is shown at the equator (solid line), north pole (dotted line) and south pole (dashed line) for the dipolar opacity case.

3.2 2D test problems

In this section, we have a look at two-dimensional (2D) toy-model problems in order to check basic multi-dimensional features of our transport solver.

3.2.1 Hemispheric difference test

We first discuss a simple configuration to test the basic ability of the code to deal with multiple dimensions without becoming unstable or producing numerical artefacts. We consider radiation diffusing out of a static scattering atmosphere. The absorption opacity vanishes everywhere.

In the first of two versions of this test, the scattering opacity, κ_s, has a spherically symmetric profile, given by

$$\kappa_s(r) = \begin{cases} \frac{1}{r^2} & , r \leq r_{max}, \\ 10^{-10} & , r > r_{max}, \end{cases} \tag{3.6}$$

with $r_{max} = 10$, while in the second version we consider a dipole-shaped opacity profile by multiplying the opacity with the factor $(1 + 0.5\cos\theta)$. We use 400×64 uniformly spaced grid points to cover the simulation domain for $(r, \theta) \in [0.01, 11.0] \times [0, \pi]$. A single energy group is used and the CFL value is set to 0.5.

In panel (a) of Fig. 3.2, the two top plots show the scattering opacity, while the two bottom plots depict, at an exemplary time of $t = 3.888 \times 10^{-10}$, the radiation energy density. The case of spherically symmetric (dipole-shaped) opacity is shown left
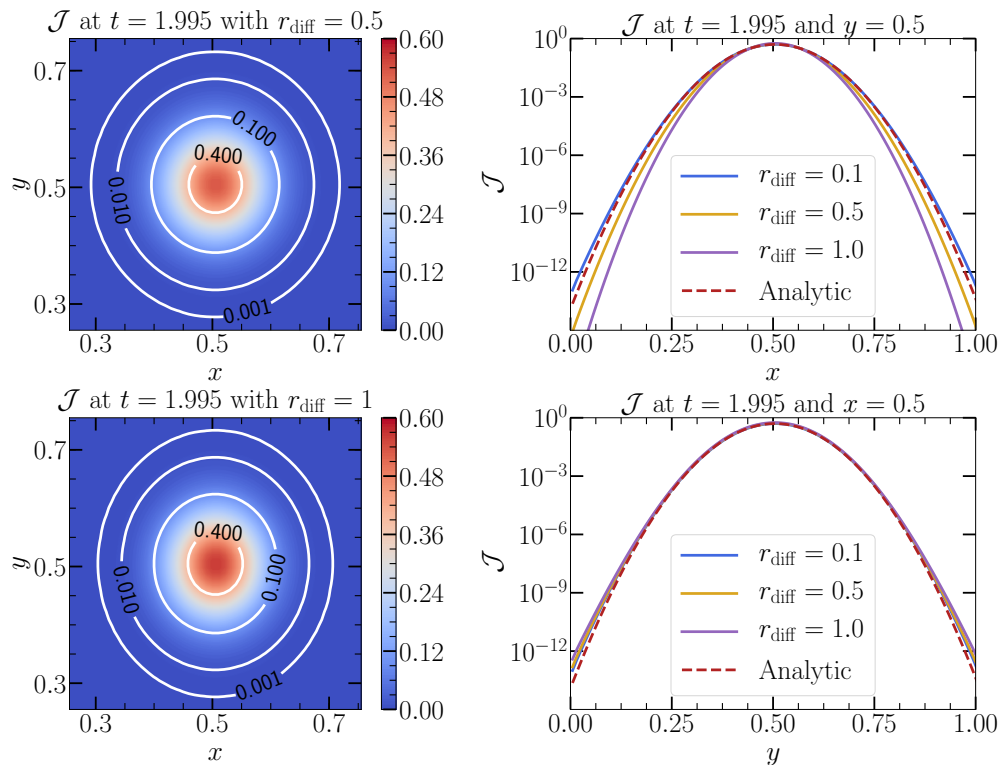
FIGURE 3.3: Two-dimensional diffusion of a Gaussian pulse (cf. Sect. 3.2.2). The Allen-Cheng method is applied along the x-direction and the Crank-Nicolson method along the y-direction. On the left side, contour plots of the radiation energy density are shown for the case of $r_{\mathrm{diff}} = 0.5$ (top) and $r_{\mathrm{diff}} = 1$ (bottom) at $t = 1.995$. On the right side, profiles of the radiation energy density are plotted along the x-direction at $y = 0.5$ (top) and along the y-direction at $x = 0.5$ (bottom). The numerical solutions for different r_{diff} are shown by solid lines and the analytical solution by dashed lines.

(right). We see that for the spherically symmetric opacity configuration the solution remains spherically symmetric, i.e. our mixed-type integration scheme combining the Crank-Nicolson and Allen-Cheng method does not lead to spurious asphericities. The relative pole-to-equator and pole-to-pole differences of $\mathcal{J}$ are $< 0.1\,\%$.

In the case of the dipole-shaped opacity, in which the southern hemisphere has lower scattering opacity than the northern hemisphere, we observe, as expected, also a hemispheric difference in the radiation energy density: A greater amount of radiation is able to escape out of the southern hemisphere compared to the northern hemisphere. In panel (b) of Fig. 3.2, radial profiles of the radiation energy density, $\mathcal{J}$, and radial flux density, $\mathcal{H}^r$, both multiplied by r^2, are shown along the $\theta = 0, \pi/2, \pi$ directions. For higher θ, we observe enhanced fluxes and energies, as well as a transition to free-streaming (i.e. $\mathcal{H}/\mathcal{J} \to 1$) at smaller radii. The stability of the conducted simulation and the plausible physics results demonstrate the basic functionality of the multidimensional version of our transport solver.

3.2.2 Diffusion of Gaussian pulse

We now investigate two-dimensional diffusion of a Gaussian pulse, which has been considered already in 1D in Sects. 3.1.1 and 3.1.2. In contrast to the test in Sect. 3.2.1, the diffusion test allows to compare with an analytical solution and, hence, we are

TABLE 3.3: Neutrino opacities used for the 1D CCSN simulations discussed in Sect. 3.3. "N" denotes nucleons and "A" and "A'" denote nuclei.

Reaction	Neutrino
$\nu + A \leftrightarrow \nu + A$	$\nu_e, \bar{\nu}_e$
$\nu + N \leftrightarrow \nu + N$	$\nu_e, \bar{\nu}_e$
$\nu_e + A \leftrightarrow e^- + A'$	$\nu_e, \bar{\nu}_e$
$\nu_e + n \leftrightarrow e^- + p$	$\nu_e, \bar{\nu}_e$
$\bar{\nu}_e + p \leftrightarrow e^+ + n$	$\nu_e, \bar{\nu}_e$
$\nu + \bar{\nu} \leftrightarrow e^- + e^+$	ν_x
$\nu + \bar{\nu} + N + N \leftrightarrow N + N$	ν_x

now able to check also on a quantitative level the proper functionality of the multi-dimensional transport, with a particular focus on the impact of the dimensional splitting with mixed explicit-implicit treatments.

We use Cartesian coordinates in a domain of size 1×1. A uniform grid with 100 points is employed in each direction, and one energy bin is used. The diffusion coefficient is set to $D = 10^{-3}$ and the problem is initialized at $t = 1$. We again define the characteristic time-step parameter $r_{\text{diff}} = D\Delta t / \Delta x^2$, where, Δt is the integration time step and Δx the grid spacing. The values of r_{diff} are varied between $\{0.1, 0.5, 1.0\}$, corresonding to CFL values of $\{1, 5, 10\}$, respectively. The Allen-Cheng scheme is applied along the x-direction and Crank-Nicolson scheme is applied along the y-direction. The simulation is stopped at $t = 1.995$.

The left panels in Fig. 4 show contour plots of the radiation energy density with $r_{\text{diff}} = 0.5$ (top) and $r_{\text{diff}} = 1$ (bottom) at the end of the simulation at time t = 1.995. The right column compares profiles along the lines at y = 0.5 (top) and x = 0.5 (bottom) of the numerical solution with that of the analytical solution, which is given by eq. (3.2) with $d = 2$ and $\tilde{r}^2 = (x - 0.5)^2 + (y - 0.5)^2$. We first note that the integration remains well-behaved and numerically stable, which is indicated by the circumstance that we see no spurious numerical features in the plotted data. Moreover, as one can see, the Gaussian pulse retains a circular shape up to a good degree, even for $r_{\text{diff}} = 0.5$, although a non-circular deformation is visible and becomes stronger for values of $r_{\text{diff}} \gtrsim 0.5$. The deformation is a result of the fact that for high values of r_{diff} the diffusion rates are somewhat reduced in x-direction, along which the explicit Allen-Cheng method is used. The error for higher values of r_{diff} increases much stronger in x-direction than in y-direction as expected, because the Allen-Cheng method is only first-order accurate while the Crank-Nicolson method is second-order accurate. However, large relative errors only appear at energy densities that are orders of magnitude smaller than the peak energy, such that the global error is still small. The test confirms that the dimensional splitting of our algorithm works well and that the Allen-Cheng method remains stable and reasonably accurate even for values $r_{\text{diff}} \sim 0.5 - 1$.

3.3 Spherically symmetric core collapse

In this section, we discuss spherically symmetric simulations with more realistic microphysics of the collapse and post-bounce evolution of a $20\,M_\odot$ stellar progenitor with solar metallicity (Woosley and Heger, 2007). We employ the SFHo nuclear equation of state (Hempel et al., 2012; Steiner, Hempel, and Fischer, 2013). The radial extent of our simulation domain is 10000 km, and we use 400 grid points, the widths
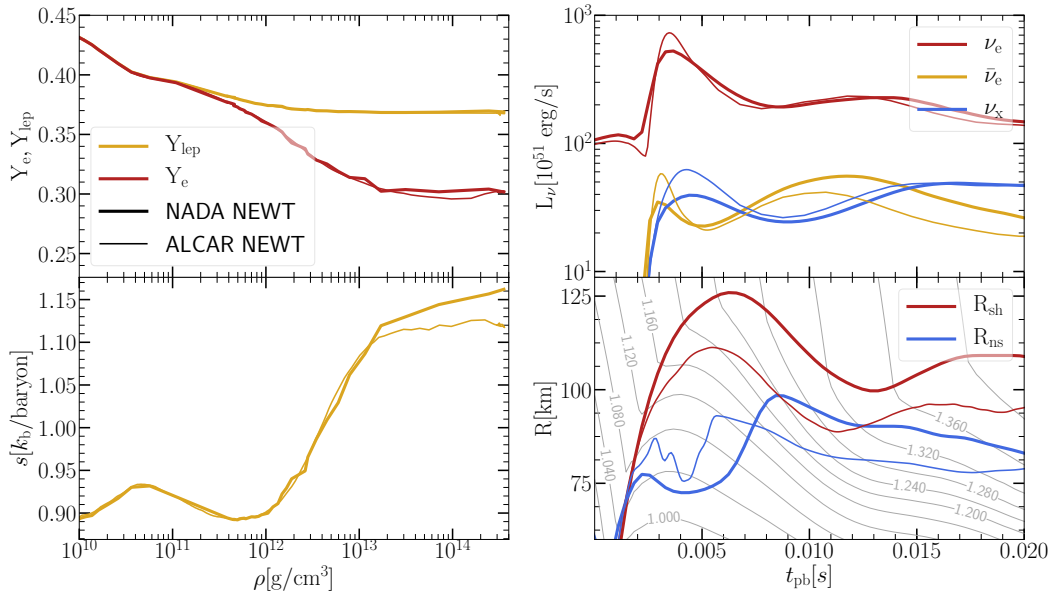
FIGURE 3.4: Properties obtained during the collapse (left) and shortly after bounce (right) in the NADA and ALCAR CCSN simulations of a 20 solar mass progenitor, both with Newtonian gravity (see Sect. 3.3). NADA (ALCAR) results are marked by thick (thin) lines. The top left plot shows the central electron fraction (red) and total lepton fraction (yellow) and the bottom left plot shows the central entropy per baryon as function of central density. The top right plot depicts as function of time the neutrino luminosities of ν_e (red), $\bar{\nu}_e$ (yellow), and ν_x (blue) measured in the comoving frame at a radius of 500 km. The bottom right plot shows the shock radii (red) and proto-neutron star radii (blue) together with contours of constant enclosed mass in units of the solar mass (gray).
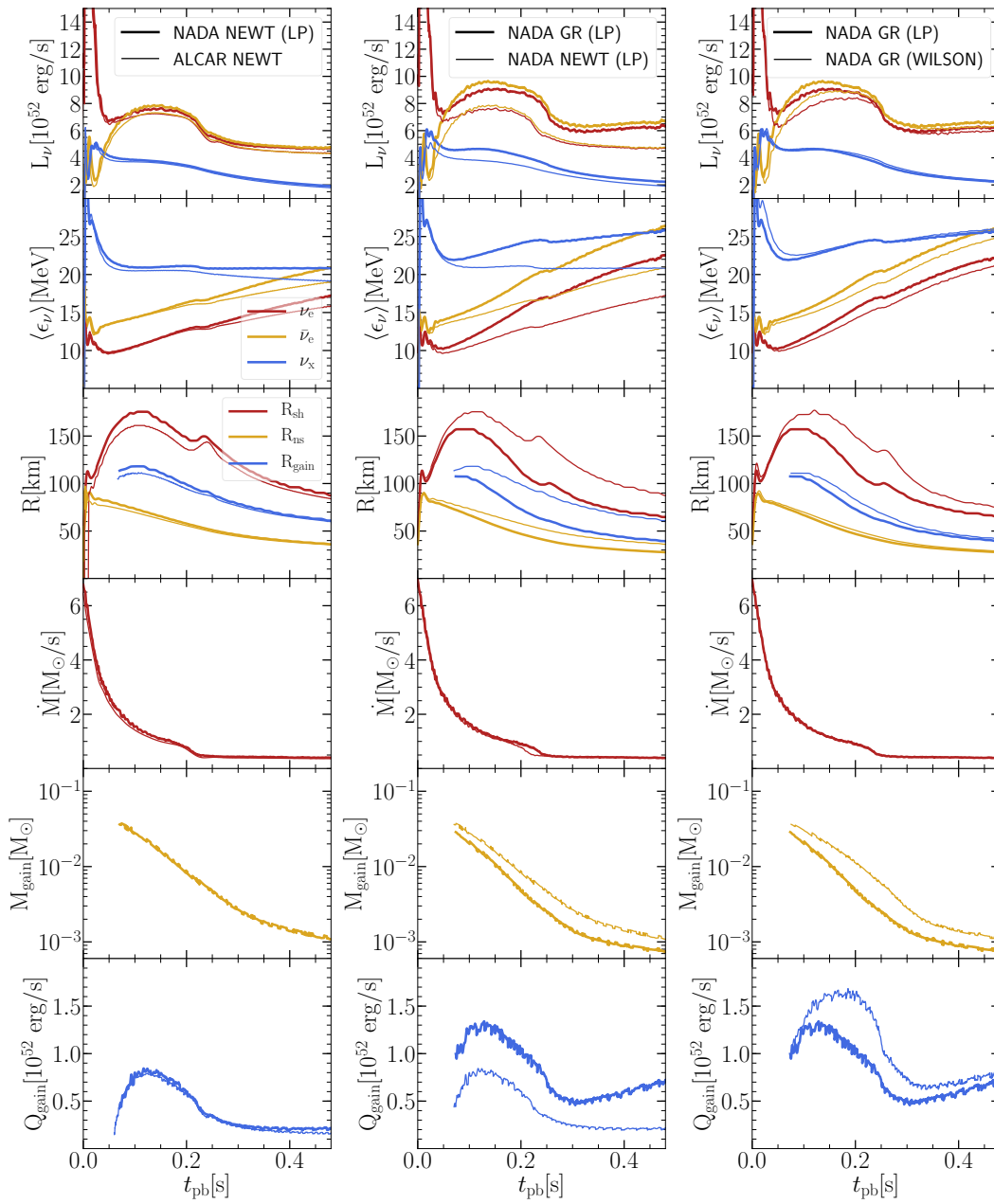
FIGURE 3.5: Comparison of global properties as functions of time for several CCSN simulations. Shown are results in the left column for the NADA (thick lines) and AL-CAR (thin lines) simulations that both use Newtonian gravity, in the middle column for NADA simulations with GR (thick lines) and Newtonian (thin lines) treatment of gravity, and in the right column for NADA simulations with GR gravity using different flux-limiters (cf. Sect. 2.3.2), namely the LP flux-limiter (thick lines) and the Wilson limiter (thin lines). From top to bottom the panels display the luminosities, the mean energies, the shock-, PNS-, and gain radii, the mass accretion rate measured at 500 km, the mass in the gain layer, and the total neutrino-heating rate in the gain layer.
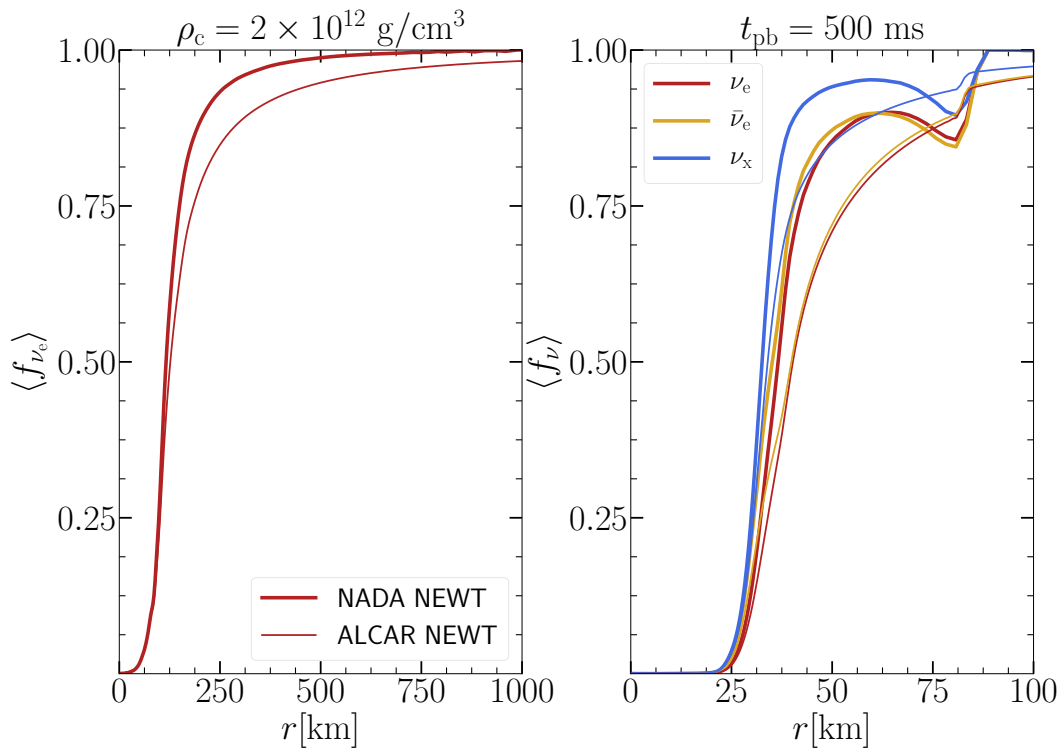
FIGURE 3.6: Comparison of the mean flux factors, eq. (3.9), as functions of radius between the NADA (thick lines) and ALCAR (thin lines) CCSN simulations using Newtonian gravity for different neutrino species ν_e (red), $\bar{\nu}_e$ (yellow), and ν_x (blue). The left panel (only for ν_e) shows the mean flux factors at a time during collapse when the central density reaches $2 \times 10^{12} \, \mathrm{g \, cm^{-3}}$, and the right plot at a post-bounce time of 500 ms. For all cases the transition to free-streaming (i.e. to high flux factors, $\langle f_\nu \rangle \gtrsim 0.5$), takes place at somewhat lower radii and higher densities for the NADA simulations, which employ the FLD approximation, compared to the ALCAR simulations, which make use of the M1 approximation.
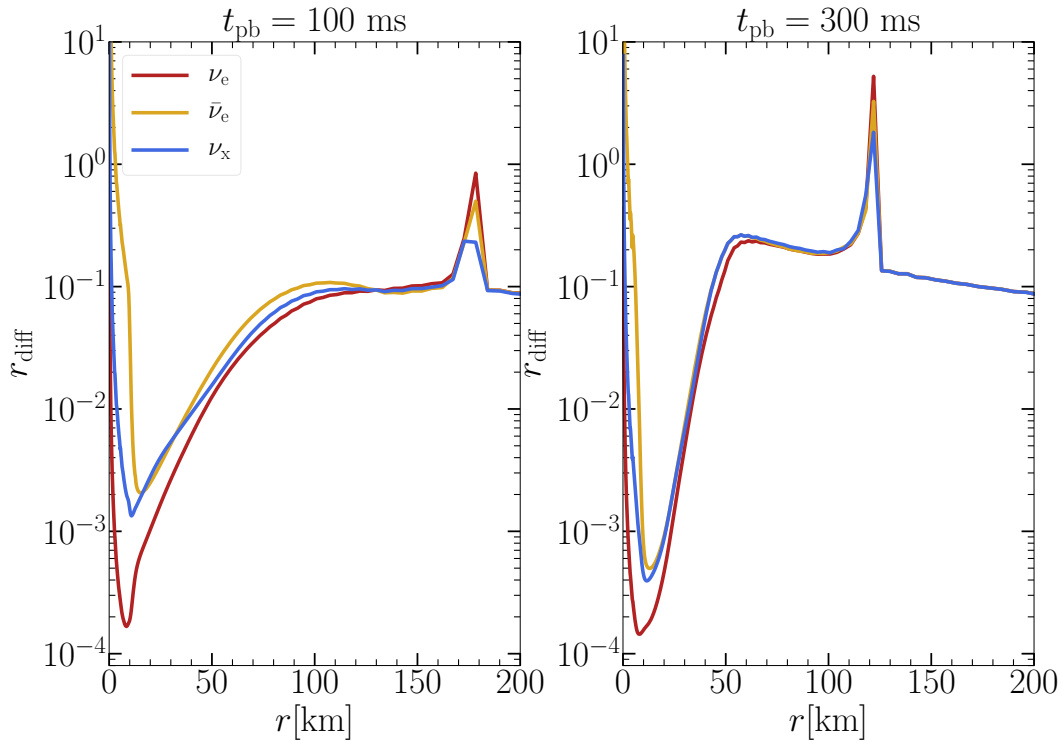
FIGURE 3.7: Estimate of the time-step parameter r_{diff} characterizing the accuracy of the explicit integration of lateral fluxes in the future case of a 2D axisymmetric simulation. We use data from the one-dimensional, Newtonian NADA simulation with LP limiter, employ eqs. (3.10) and (3.11), and assume an angular resolution of 1.4 degrees. The resulting r_{diff} is shown at post-bounce times of 100 ms (left) and 300 ms (right) for species ν_e (red), $\bar{\nu}_e$ (yellow), and ν_x (blue).

of which are constant up to 4 km and afterwards increase by 3 % from cell to cell. The energy grid is logarithmic, with 15 points covering energies from 0 to 400 MeV, where 400 MeV is the upper boundary of the last energy bin. We evolve electron neutrinos (ν_e), electron anti-neutrinos ($\bar{\nu}_e$), and ν_x neutrinos that are representative of the four heavy-lepton neutrinos. The neutrino reactions taken into account are listed in Table 3.3. Their formulation is mostly based on Bruenn (1985) and Rampp and Janka (2002), but additionally includes corrections due to weak magnetism and recoil (Horowitz, 2002). We also take into account nucleon-nucleon bremsstrahlung. Following the recipe suggested by O'Connor (2015), we neglect pair-processes for electron-type neutrinos and treat pair-processes for ν_x neutrinos with a prescription that is formally equivalent to emission/absorption.

We perform simulations with fully general relativistic hydrodynamics and transport, denoted by NADA GR, using each of the two flux-limiters, LP and Wilson (cf. eqs. (2.31)). However, in order to compare our code with a reference solution, we first discuss a simulation, called NADA NEWT, that is identical to NADA GR with the LP limiter, but that is conducted with a Newtonian treatment of gravity and special relativistic hydrodynamics. We compare this model to model ALCAR NEWT which is performed with the ALCAR code (Just, Obergaulinger, and Janka, 2015; Just et al., 2018). Model ALCAR NEWT contains exactly the same input physics, but it employs the M1 approximation for the neutrino transport and assumes non-relativistic hydrodynamics[2].

In the left column of Fig. 3.4, we compare characteristic properties of the collapse between models NADA NEWT and ALCAR NEWT, namely the electron fraction, Y_e, lepton fraction, Y_{lep}, and entropy per baryon at the stellar center as function of the central density, ρ. Neutrino trapping sets in once the central density reaches $\sim 2 \times 10^{12}\,\text{g cm}^{-3}$. After the onset of neutrino trapping, the lepton fraction remains constant with a value around 0.37 for both codes. The electron fraction roughly asymptotes at a central density of $\sim 2 \times 10^{13}\,\text{g cm}^{-3}$. The deleptonization slows down around $5 \times 10^{10} - 10^{11}\,\text{g cm}^{-3}$ in both models due to neutron shell blocking and a low abundance of free protons (e.g. Bruenn, 1985). After the onset of trapping because of a growing number of free nucleons and α-particles, the total entropy (stellar gas and neutrinos) is conserved because of the adiabatic subsequent evolution, but the entropy per baryon of the gas increases to $\approx 1.15\,k_b/\text{baryon}$. Overall, both simulations agree very well in their deleptonization behavior.

In the right column of Fig. 3.4, we show the neutrino luminosity as well as the shock- and PNS-radii as functions of time until 20 ms post bounce. For the present spherically symmetric case we define the comoving-frame luminosity as

$$L_\nu(r) \equiv 4\pi e^{4\phi} r^2 \int \mathcal{H}_\nu(r, \epsilon)\, \mathrm{d}\epsilon\,, \tag{3.7}$$

where $\phi = 0$ for the case of Newtonian gravity. The luminosity obtained with the NADA code agrees well with that of the ALCAR code. The integrated energy loss is $\sim$5 % higher in the NADA model than that in the ALCAR model within the first 20 ms of post-bounce evolution. The peak in the luminosities of ν_e and $\bar{\nu}_e$ around 10-15 ms post-bounce time is due to early expansion and subsequent compression of matter behind the shock. In the bottom-right plot of Fig. 3.4, we see mass shells between 0.8 to 1.16 $M_\odot$ undergo a early shock expansion until 4 ms post-bounce time and then fall back. The compression of matter produces extra neutrinos.

---

[2]Note that in the considered simulations the velocities are so low that no significant differences should arise from the different hydrodynamics treatment.

The left column of Fig. 3.5 provides various quantities as functions of time for the NADA NEWT and ALCAR NEWT simulations, namely the neutrino luminosities, L_ν, the neutrino mean energies,

$$\langle \epsilon_\nu \rangle (r) \equiv \frac{\int \mathcal{J}(r, \epsilon) \, \mathrm{d}\epsilon}{\int \mathcal{J}(r, \epsilon) \, \epsilon^{-1} \, \mathrm{d}\epsilon} \, , \tag{3.8}$$

the mass-accretion rates above the shock at 500 km, $\dot{M}$, the total masses in the gain layer, M_{gain}, and the total neutrino-heating rates, Q_{gain}. The luminosities and mean energies, as well as actually all remaining quantities agree remarkably well between both codes. We notice slightly higher luminosities in the NADA runs and, particularly at late times, a secular drift towards higher mean energies in the NADA NEWT model. We speculate that this difference might be related to what we see in Fig. 3.6, where radial profiles of the mean flux factor,

$$\langle f_\nu \rangle (r) \equiv \frac{\int \mathcal{H}_\nu(r, \epsilon) \, \epsilon^{-1} \, \mathrm{d}\epsilon}{\int \mathcal{J}_\nu(r, \epsilon) \, \epsilon^{-1} \, \mathrm{d}\epsilon} \, , \tag{3.9}$$

are plotted: In the NADA simulation, the flux factors rise at slightly smaller radii than in the ALCAR simulation, which means that neutrinos are effectively released from deeper within the PNS and therefore at higher temperatures (see below for further discussion of Fig. 3.6). Nevertheless, the very good overall agreement between both codes is encouraging and confirms that the combined neutrino-hydro solver is working well and that the equation of state and the neutrino-interactions are implemented correctly.

In the middle column of Fig. 3.5, we compare the fully relativistic NADA GR simulation with the NADA NEWT model, using for both cases the LP limiter. The main impact of GR is to produce an effectively steeper gravitational potential. Hence, the core bounces $\approx 40 \, \mathrm{ms}$ earlier in the GR case compared to the Newtonian case. Subsequently, the GR treatment produces a considerably more compact PNS and post-shock configuration. As a consequence of the higher compactness, the temperatures at the PNS surface are increased, which results in significantly enhanced neutrino luminosities and mean energies. The enhancement is even strong enough to over-compensate for the lower masses in the gain layer and to yield considerably higher total neutrino-heating rates compared to the Newtonian model. The qualitative differences found here between Newtonian and general relativistic CCSN models are in good agreement with previous studies (e.g. Bruenn, De Nisco, and Mezzacappa, 2001; Marek et al., 2006; Müller, Janka, and Marek, 2012). We conclude that the coupling of the neutrino-hydrodynamics components of the code to the Einstein solver is working well, at least in spherical symmetry.

In order to test the sensitivity with respect to the chosen flux-limiter, we also compare the NADA GR simulation that uses the LP limiter against a similar simulation that employs the Wilson limiter; see the right column of Fig. 3.5 for the corresponding quantities as functions of time. Using the Wilson limiter instead of the LP limiter results in an overall less compact configuration, i.e. in higher values of the shock-, PNS-, and gain-radii, particularly at earlier times, $t_{\mathrm{pb}} \gtrsim 0.3 \, \mathrm{s}$, while later on the differences become smaller. The most likely reason is found when comparing the luminosities, which for electron-type neutrinos are significantly reduced during the first $\sim 0.2 - 0.3 \, \mathrm{s}$ of post-bounce evolution. The lower neutrino-cooling rates explain the larger PNS radii, and those also cause (e.g. Janka, 2012) larger gain- and shock-radii. The more powerful neutrino heating in the gain layer is thus mainly a result

of the increased mass in the gain layer compared to the case with the LP limiter.

In Fig. 3.6, we show the radial profile of the mean flux factor, eq. (3.9), for models NADA NEWT (with LP limiter) and ALCAR NEWT, at a time when the central density is $2 \times 10^{12}\,\mathrm{g\,cm^{-3}}$ (left plot) and at 300 ms post bounce (right plot). Although the M1 scheme used in ALCAR is not a fully accurate solution of the Boltzmann equation either, it is likely somewhat more reliable than the FLD solution (see, Just, Obergaulinger, and Janka 2015 for a comparison of FLD and M1 with a Boltzmann solver for static CCSN-related configurations). In both cases, we see that the FLD solution makes the transition to free-streaming conditions at smaller radii compared to the M1-based ALCAR solution. Furthermore, in the FLD scheme, the flux factor jumps to high values artificially strongly near sharp drops in the transport opacity (see, Janka 1992 for a detailed discussion). As a result, the mean flux factor abruptly becomes ≈ 1 at the shock, which lies at $r \approx 80-90\,\mathrm{km}$ in the right panel of Fig. 3.6. The results concerning the flux factor are consistent with previous investigations of the FLD scheme; see, Dgani and Janka (1992) who identify a "missing opacity" problem of FLD that can be solved, only in 1D however, by introducing an "artificial opacity". However, the otherwise good agreement between NADA NEWT and ALCAR NEWT suggests that the aforementioned deficiencies are small enough to affect the 1D dynamics at most at the few-percent level.

As a final point we discuss the time-integration accuracy of a (future) multi-dimensional CCSN simulation based on our 1D simulation data. As we recall from Sect. 2.4, the time integration of the transport equations is done implicitly for the source terms as well as the radial fluxes and energy derivatives, and explicitly for the lateral fluxes. We consider for the case of an axisymmetric simulation the resulting characteristic time-step parameter,

$$r_{\mathrm{diff}} = \langle D_\nu \rangle \Delta t / (r\Delta\theta)^2 \,, \tag{3.10}$$

i.e. the ratio of the employed integration time step, Δt, and the characteristic timescale associated with the lateral diffusion terms, $(r\Delta\theta)^2/\langle D_\nu \rangle$. We use the Δt employed in the 1D simulation and assume a reasonable value of 1.4 degree for $\Delta\theta$. The energy-averaged diffusion coefficient, $\langle D_\nu \rangle$, is calculated as

$$\langle D_\nu \rangle(r) = \frac{\int D_\nu(r,\epsilon)\,\mathcal{J}_\nu(r,\epsilon)\,\epsilon^{-1}\,\mathrm{d}\epsilon}{\int \mathcal{J}_\nu(r,\epsilon)\,\epsilon^{-1}\,\mathrm{d}\epsilon} \,. \tag{3.11}$$

The estimates of r_{diff}, shown in Fig. 3.7 for an early and a late post-bounce time, allow us to identify regions, $r_{\mathrm{diff}} \gtrsim 1$, in which the explicit Allen-Cheng method is potentially less accurate in describing the lateral neutrino propagation. We find that high values, $r_{\mathrm{diff}} \gtrsim 1$, are reached only near the center of the PNS and close to the shock. This is reassuring, because deeply within the PNS neutrinos are trapped and neutrino fluxes are strongly dominated by advection fluxes, while at large radii in the vicinity of the shock lateral neutrino fluxes are anyway small compared to radial fluxes. Hence, our estimate indicates that the explicit treatment of lateral terms in multi-dimensional simulations will only have minor consequences on the dynamical evolution.

Chapter 4

Core-Collapse Supernova Simulations of Very Massive Stars

In this chapter, we describe the core collapse simulations considering progenitors of 60, 80 and 115 $M_\odot$ of very massive stars.

4.1 Numerical Setup

The core-collapse simulation of the very massive star was conducted using the general-relativistic hydrodynamics and transport code NADA (Baumgarte et al., 2013; Montero, Baumgarte, and Müller, 2014) in two dimension. It is a finite difference code with spherical polar coordinates. The code solves the BSSN formulation of Einstein equations using the second order partial implicit Runge-Kutta method (Montero and Cordero-Carrión, 2012). In current study, we solve the BSSN equation under the assumption of spherically symmetric metric. We use the "$1 + \log$" condition for the lapse function and the non-advective hyperbolic Gamma-driver for the shift vector (Baumgarte, Montero, and Müller, 2015).

We use the generalized Valancia formalism for the hydrodynamics equations (Montero, Baumgarte, and Müller, 2014). The finite difference high resolution shock capturing method is used to solve the hydrodynamics equation. We use the PPM method (Colella and Woodward, 1984) for the reconstruction of primitive variable at the cell interface. The approximate Riemann solver HLL (see, e.g. Toro 2009) is used for the numerical flux calculation at the cell interface. The second order Runge-Kutta method (see, e.g. Anderson 2011) for the time integration of the hydrodynamics equations. We use a spherical core of 3 km to avoid extreme time step size restriction imposed by Courant-Friedrichs-Lewy condition in the spherical polar coordinates. The tabulated equation of state SFHo (Hempel et al., 2012; Steiner, Hempel, and Fischer, 2013) is used for this study.

We employed the multi-dimensional multi-energy group flux limited diffusion (FLD) scheme to solve the neutrino transport equation (see, chapter 2, for details). The FLD equation is solved in the comoving frame. We used a mixed implicit-explicit method to solve the FLD equation. The number of neutrino energy bin used in this study is 16, spanning 2.5 MeV to 500 MeV. The energy bins are geometrically spaced. We evolve the neutrino transport for electron neutrino ν_e, electron anti-neutrino $\bar{\nu}_e$ and muon and tau neutrino and their anti-neutrino under a single species ν_x. The neutrino reactions considered are shown in the Table 3.3. Details of neutrino opacity can be found in Rampp and Janka (2002) and Bruenn (1985) and references cited in those articles. The pair-process and Bremsstrahlung for ν_x is treated using the recipe from O'Connor (2015).

TABLE 4.1: Progenitor Properties. We tabulate the remnant mass of progenitor, M_{rem}, just before core collapse, the iron-core mass, M_{Fe}, compactness of progenitor, $\xi_{2.5}$, given by equation (4.1), total angular momentum of remnant, J_{rem}, and iron core, J_{Fe}, the Kerr parameter of remnant, a_{rem}, given by equation (4.2), the post-bounce time when shock expansion starts, t_{sh-exp}, and the post-bounce time when BH is formed, t_{BH}. For details, see Table 5 of Woosley 2017.

Model	M_{rem} $[M_\odot]$	M_{Fe} $[M_\odot]$	$\xi_{2.5\,M_\odot}$	J_{rem} $[10^{50}\ \mathrm{erg\ s}]$	J_{Fe} $[10^{48}\ \mathrm{erg\ s}]$	a_{rem}	t_{sh-exp} [s]	t_{BH} [s]
C115	79.46	2.44	0.89				0.210	0.400
NR80Ar	47.77	2.74	0.84				0.220	0.350
R80Ar	47.77	2.74	0.84	14	7.2	0.07	0.220	0.350
C60C	46.44	2.35	0.77	105	37	0.55		0.510

We used an uniform grid in the angular direction with an angular resolution of 1.4 degree and a non-uniform grid in the radial direction with 500 grid points. The $\Delta r/r$ is 1% in the gain region. We use a reflecting boundary condition at the center for all GR-hydro-transport quantities. The outer boundary is at 10^9 cm. We employed a inflow boundary condition at the outer boundary for the hydrodynamics equations. For the Einstein equations, the Sommerfeld boundary condition (Baumgarte et al., 2013) is applied at the outer boundary. The free-streaming boundary condition is applied for the transport equation at the outer boundary (see, chapter 2). A reflecting boundary condition is used at the poles for all quantities.

4.2   Progenitor Properties

In this section, we describe different properties of very massive star progenitors used in this study (see, e.g. Vink 2015 for definition of very massive stars). We conducted core-collapse simulation of several very massive star progenitors from the stellar evolution calculation of Woosley (2017). The stellar evolution was conducted by the KEPLER code (see, e.g. Heger, Langer, and Woosley 2000; Woosley, Heger, and Weaver 2002; Heger, Woosley, and Spruit 2005; Sukhbold et al. 2016). A very massive star possibly can experience pulsational pair instability after the carbon burning phase. In the post-carbon burning period electron-positron pair is produced if a star have high enough temperature ($> 3 \times 10^9$ K). During the pair creation thermal energy is converted to rest mass energy of the pair which otherwise would have contributed to the pressure of the star. As a result, the adiabatic index drops below 4/3. Due to lack of pressure support the star contracts and the temperature rises. The temperature rise causes rapid burning of carbon, oxygen and, in some cases, even silicon. The energy release from the burning increases the pressure and slows down the collapse. If enough energy is released the star can experience rebound and explosion is possible. These phenomenon is called the pulsational pair instability and happens when the Helium core mass is approximately above 35 $M_\odot$. If the energy release from the burning is high, so that, the whole star explode in a single pulse, then it is called "pair-instability supernova". The star with Helium core mass approximately above 65 $M_\odot$ undergoes pair-instability supernova. If the energy release is not enough to unbind the whole star in a single pulse, star can experience multiple cycle of expansion and contraction. It is called "pulsational pair-instability supernova". Due to pulsation the star loses its outer Hydrogen and in some cases the Helium envelops. We refer to Woosley and Heger (2015), for a review on the topic of pulsation pair-instability in the very massive star.
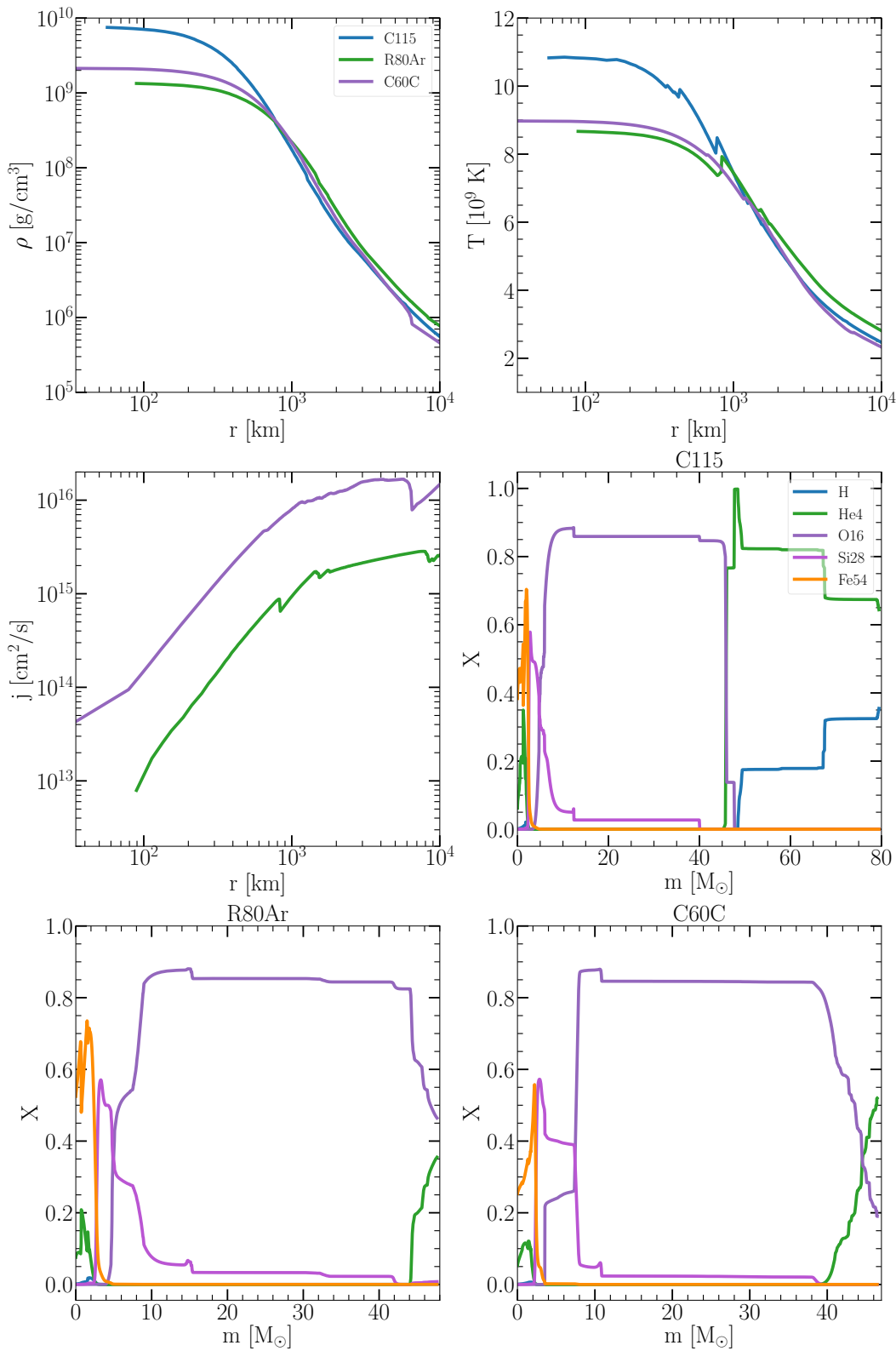
FIGURE 4.1: Progenitor Property. In the top row, we show the initial radial profile of baryonic density (left) and temperature (right) for different progenitor models. In the middle row, we show the initial radial profile of specific angular momentum (left) for different progenitor models and the abundance of different nuclei against mass coordinate for C115 model. In the bottom row, the initial abundance is shown against the mass coordinate for R80Ar model (left) and C60C model (right).
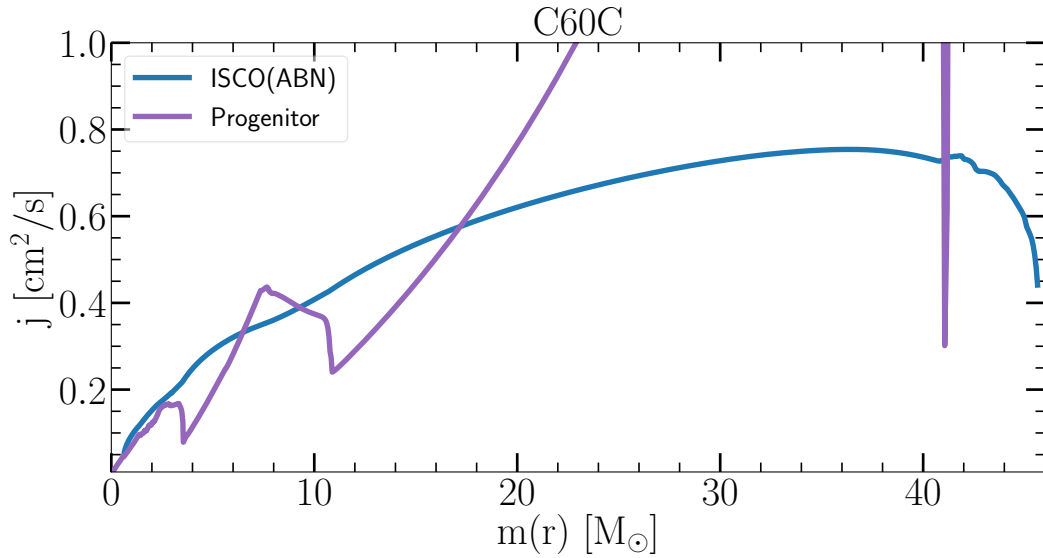
FIGURE 4.2: Specific angular momentum of the ISCO and the corresponding specific angular momentum of the C60C model progenitor. An accretion disk can be formed on mass coordinates where angular momentum of progenitor is higher than that of ISCO.

We studied the non-rotating 115 $M_\odot$ model (hereafter, C115) and rotating 80 $M_\odot$ and 60 $M_\odot$ model (hereafter, R80Ar and C60C respectively). We also studied the 80 $M_\odot$ model without rotation (hereafter, NR80Ar). All model have zero-age-main-sequence (ZAMS) metallicity of 10% $Z_\odot$. The C60C model has undergone chemically homogeneous evolution due to efficient mixing induced by the rapid rotation (see, e.g. Woosley and Heger 2006). Some of the properties of the progenitors are shown in Table 4.1 (for details, see Table 5 of Woosley 2017). Table 4.1 shows the remnant mass, M_{rem}, after pulsational mass losses, the iron-core mass, M_{Fe}, the compactness parameter, $\xi_{2.5\ M_\odot}$, the specific angular momentum of remnant, J_{rem}, the iron-core specific angular momentum, J_{Fe} and the Kerr parameter of the remnant, a_{rem}, after pulsational mass losses. The compactness parameter is defined as in O'Connor and Ott (2011):

$$\xi_M = \frac{M/M_\odot}{R(M_{bary} = M)/1000\ \text{km}},$$ (4.1)

and the Kerr parameter is defined as,

$$a_{rem} = \frac{J_{rem}c}{GM_{rem}^2}.$$ (4.2)

The progenitors have iron-core of mass in the range of 2.35-2.74 $M_\odot$ (see, Table 4.1). The values of compactness of the progenitors are very high. The Fig. 4.1 shows the density, ρ, temperature, T, and specific angular momentum, j, profile along the radius for different progenitors. It also shows the abundance of different species against the mass coordinate. The rotating model R80Ar and C60C has the specific angular momentum of about 2.85×10^{15} cm^2/s and 1.68×10^{16} cm^2/s in the silicon shell. The C115 model has lost the hydrogen envelop. The R80Ar and C60C model has oxygen envelop mixed with helium.

The rapidly rotating C60C model can possibly form an accretion disk, after its inner core have collapsed to a BH. In Fig. 4.2, shows the specific angular momentum

of C60C model and the specific angular momentum of innermost stable circular orbit (ISCO) of the kerr BH against mass coordinate, m(r). We use the rotating BH potential from Artemova, Bjoernsson, and Novikov (1996) for the calculation of specific angular momentum of ISCO. If the specific angular momentum of the progenitor at certain m(r) is higher than the specific angular momentum of ISCO, an accretion disk can be formed at that m(r). In Fig. 4.2, we see the specific angular momentum of the C60C progenitor is greater than that of ISCO at $m(r) > 18 \, M_\odot$. Therefore, the C60C model has the potential to form an accretion disk around a BH.

4.3 Definition

In this section, we show definitions of different diagnostic quantities used for the analysis of the simulation results. The mass accretion rate at a radius *r* is defined as:

$$\dot{M}(r) = r^2 e^{4\phi} \int d\Omega \, W\rho(v^r - \beta^r/\alpha) \, , \tag{4.3}$$

where, $\phi, \beta^r, \alpha, \rho, v^r, W$ are the conformal factor, radial component of the shift vector, the lapse function, the baryonic density, the radial fluid velocity and lorentz factor, respectively and $d\Omega = 2\pi d(\cos\theta)$. The mass of a shell is defined as:

$$m(r) = \int dV \, W\rho \, . \tag{4.4}$$

Here, $dV = dr r^2 e^{6\phi} d\Omega$. The integral spans over the width of the mass shell in radial direction and from 0 to π in the polar direction. Similarly, the total angular momentum along the rotation axes is calculated by:

$$J_z^{tot}(r) = \int dV \, e^{-2\phi} W^2 \rho h v_z \, , \tag{4.5}$$

where *h* is the specific enthalpy given by $c^2 + e + P/\rho$. ϵ, P, v_z are the specific internal energy with out rest mass, the pressure and the covariant component of fluid velocity along the rotating axes, respectively. The mass in the gain layer is given by:

$$M_{gain} = \int_{R_g(\theta)<r<R_{sh}(\theta)} dV \, W\rho \, , \tag{4.6}$$

and the specific angular momentum in the gain layer along the rotation axes is given by:

$$j_{gain} = \frac{1}{M_{gain}} \int_{R_g(\theta)<r<R_{sh}(\theta)} dV \, e^{-2\phi} W^2 \rho h v_z \, . \tag{4.7}$$

We assume the surface density of PNS is $10^{11} \, g/cm^3$. The rotational period of PNS is given by:

$$T_{NS} = \frac{2\pi I_{NS}}{J_{NS}}, \tag{4.8}$$

where I_{NS} and J_{NS} are the moment of inertia and the total angular momentum of the PNS. The angular average of any quantity X is given by:

$$\langle X \rangle (r) \equiv \frac{\int d\Omega X W \rho}{\int d\Omega W \rho} \ . \tag{4.9}$$

The energy is calculated using the below formula following Müller, Janka, and Marek (2012):

$$e_{\text{tot}} = \alpha(\rho h W^2 - P) - \rho W c^2 \ , \tag{4.10}$$

The turbulent kinetic energy is given by:

$$e_{\text{turb}} = \rho \sum_{i=r,\theta,\phi} (v_i - \langle v_i \rangle)^2 \ . \tag{4.11}$$

The total energy in the gain layer is given by:

$$E_{\text{gain}}^{\text{tot}} = \int_{R_g(\theta)<r<R_{sh}(\theta)} dV \, e_{\text{tot}} \ . \tag{4.12}$$

Here, R_g and R_{sh} are the gain and shock radius, respectively. Similarly the turbulant energy in the gain layer is given by:

$$E_{\text{gain}}^{\text{turb}} = \int_{R_g(\theta)<r<R_{sh}(\theta)} dV \, e_{\text{turb}} \ . \tag{4.13}$$

We define the diagnostic energy in the gain layer by:

$$E_{\text{gain}}^{\text{diag}} = \int_{R_g(\theta)<r<R_{sh}(\theta)} dV \, e_{\text{tot}} \, \Theta(e_{\text{tot}}), \tag{4.14}$$

where Θ is the Heaviside step function. The overburden energy is calculated using below formula:

$$E^{\text{ob}} = \int_{R_{sh}(\theta)<r<R_{\text{out}}} dV \, e_{\text{tot}} \ , \tag{4.15}$$

where R_{out} is the outer radius of the star. The Luminosity is given by the below formula:

$$L_\nu(r) = e^{4\phi} r^2 \int d\Omega \int d\epsilon \mathcal{H}_\nu(r,\theta,\epsilon) \ . \tag{4.16}$$

The mean neutrino energy is defined as:

$$\langle \epsilon_\nu \rangle (r,\theta) \equiv \frac{\int \epsilon \mathcal{J}_\nu(r,\theta,\epsilon) \, \epsilon^{-1} d\epsilon}{\int \mathcal{J}_\nu(r,\theta,\epsilon) \, \epsilon^{-1} d\epsilon} \ , \tag{4.17}$$

and the RMS neutrino energy is defined as:

$$\langle \epsilon_\nu^2 \rangle (r,\theta) \equiv \frac{\int \epsilon^2 \mathcal{J}_\nu(r,\theta,\epsilon) \epsilon^{-1} d\epsilon}{\int \mathcal{J}_\nu(r,\theta,\epsilon) \epsilon^{-1} d\epsilon} \ . \tag{4.18}$$

Here, $\mathcal{J}_\nu$ and $\mathcal{H}_\nu$ are the energy density and energy density flux of neutrino, respectively. The spherical harmonics decomposition of the shock radius R_{sh} is done using

below formula:

$$a_l \equiv \frac{2l+1}{2} \int_0^\pi R_{sh}(\theta) P_l(\cos\theta) d(\cos\theta). \tag{4.19}$$

The heating efficiency is given by:

$$\eta \equiv \frac{Q_{gain}}{L_{\nu_e}(r = 500\ \text{km}) + L_{\bar{\nu}_e}(r = 500\ \text{km})}, \tag{4.20}$$

here, $\dot{Q}_\nu$ is the total heating rate by neutrinos in the gain layer. The Brunt-Väisälä frequency is calculated by,

$$N_{BV}^2 \equiv \frac{\alpha C_L}{\rho h e^{4\phi}} \frac{\partial \alpha}{\partial r}, \tag{4.21}$$

where C_L is given by:

$$C_L \equiv \frac{\partial \rho(1+\epsilon)}{\partial r} - \frac{1}{c_s^2} \frac{\partial P}{\partial r}. \tag{4.22}$$

The advection timescale through the gain layer is defines as:

$$\tau_{adv} = \frac{M_{gain}}{\dot{M}(r = 500\ \text{km})}, \tag{4.23}$$

The heating timescale in the gain layer is given by the following formula:

$$\tau_{heat} = \frac{|E_{gain}^{tot}|}{Q_{gain}}, \tag{4.24}$$

The χ parameter is given by:

$$\chi = \frac{\tau_{adv}}{\tau_{conv}}. \tag{4.25}$$

Here, τ_{conv} is convection timescale in the gain layer. The convection timescale in the gain layer is calculated using the Brunt-Väisälä frequency where $N_{BV} < 0$. We calculate the quadrupole amplitude, A_{20}^{E2}, according to the formula (see, e.g. Obergaulinger, Aloy, and Müller 2006):

$$\begin{aligned}
A_{20}^{E2} = {} & \frac{G}{c^4} \frac{16\pi^{3/4}}{\sqrt{15}} \int_{-1}^{+1} dz \int_0^\infty r^2 dr \rho \Big[v_r v_r (3z^2 - 1) + v_\theta v_\theta (2 - 3z^2) \\
& - v_\phi v_\phi - 6 v_r v_\theta z \sqrt{1 - z^2} - r \partial_r \Phi (3z^2 - 1) + 3 \partial_\theta \Phi z \sqrt{1 - z^2} \Big],
\end{aligned} \tag{4.26}$$

where, $z = \cos\theta$ and Φ is the gravitational potential. The dimensionless strain, h_+, measured by an observer at a distance R and at an inclination angle Θ is given by:

$$h_+ = \frac{1}{8} \frac{\sqrt{15}}{\pi} \sin^2\Theta \frac{A_{20}^{E2}}{R}. \tag{4.27}$$

In this work, we assume the observe is located at equatorial plane ($\sin^2\Theta = 1$).

4.4   Results: before black hole formation

In this section, we will discuss the result of our CCSN simulations. The model C115, NR80Ar and R80Ar behave rather similarly. First, We will discuss the time evolution of these three model. Later, we will discuss about the rapidly rotating C60C model. In the top left plot of Fig. 4.3, the time evolution of the shock radius is show. We see the rapid shock expansion after the bounce stops around 30 ms post-bounce time (t_{pb}) at a radius around 130 km for C115, NR80Ar and R80Ar model. We observe the prompt proto-neutron star (PNS) convection created by the lepton number gradient last until 20-25 ms post-bounce time. Since the rotation in the model R80Ar is weak, we do not see impact of rotation on the prompt proto-neutron star convection in R80Ar model. We see the stagnated shocks start to expand at around 210 ms post-bounce time for above mentioned models.

In the top right plot of Fig. 4.3, we see the time evolution of the mass accretion rate at a radius of 500 km. The mass accretion rate of C115, NR80Ar and R80Ar model are similar. The mass accretion rates of all the mentioned model remain at high value of 2-3 $M_\odot$/s in between 100 ms and 250 ms post-bounce time.

The rapid contraction of the proto-neutron star (see the right plot in the second row of Fig. 4.3) along with high mass accretion rate (see the top right plot of Fig. 4.3), which decreases the advection timescale through the gain layer, trigger the standing accretion shock instability (SASI) (see, e.g. Blondin and Mezzacappa 2007; Foglizzo et al. 2007). Since we are conducting the simulation in 2D, we observe only the polar sloshing SASI activities (see, e.g. Fernández et al. 2014 for detail discussion of SASI in 2D dimensional CCSN simulation). The SASI causes the expansion of the shock along the polar axis and brings more materials behind the shock. These material acts as a fresh fuel and produces electron type neutrinos by the electron and positron capture on the free neutron and proton, respectively. The SASI activities continue until around 180-200 ms post-bounce time. Afterward, due to strong neutrino heating in the gain layer (see the right plot in the second row of Fig. 4.4), convection dominates over the SASI. In the third row from the top of Fig. 4.4, the right plot shows the χ parameter in the gain layer. The χ parameter, which is the ratio of the advection timescale and the growth timescale of the convection, obtains a value larger than 3 around the time when the neutrino heated convection in the gain layer becomes dominant over SASI (see, e.g. Foglizzo, Scheck, and Janka 2006; Fernández et al. 2014 for discussion about the χ parameter).

During the SASI activity period, the high entropy hot bubbles created at the both poles flow down to the equatorial plane and merge together, forming large high entropy bubble. The large equatorial hot bubble helps to push the shock in radially outward direction.

In Fig. 4.3, we also show the spherical harmonics decomposition of the shock radius according to equation (4.19). We show the $l = 1, 2, 3$ component normalized by the mean shock radius, a_0, in the third row right plot, bottom row left and right plot of Fig. 4.3, respectively. we see that due to SASI, the shock is highly deformed. The dipole ($l = 1$) and quadruple ($l = 2$) component of the shock is about 25%. We also see that the quadruple component of the PNS radius (thin line) is close to zero for C115, NR80Ar and R80Ar model.

In the top row of Fig. 4.5, we show the neutrino luminosities at 500 km for different type of neutrinos. The neutrino luminosity can be divided into two parts, the diffusive part and the accretion part. The diffusive part is due to the diffusion of neutrino out of the PNS. The infalling matter releases the gravitational binding energy while settling down onto the surface of the PNS and a part of the released
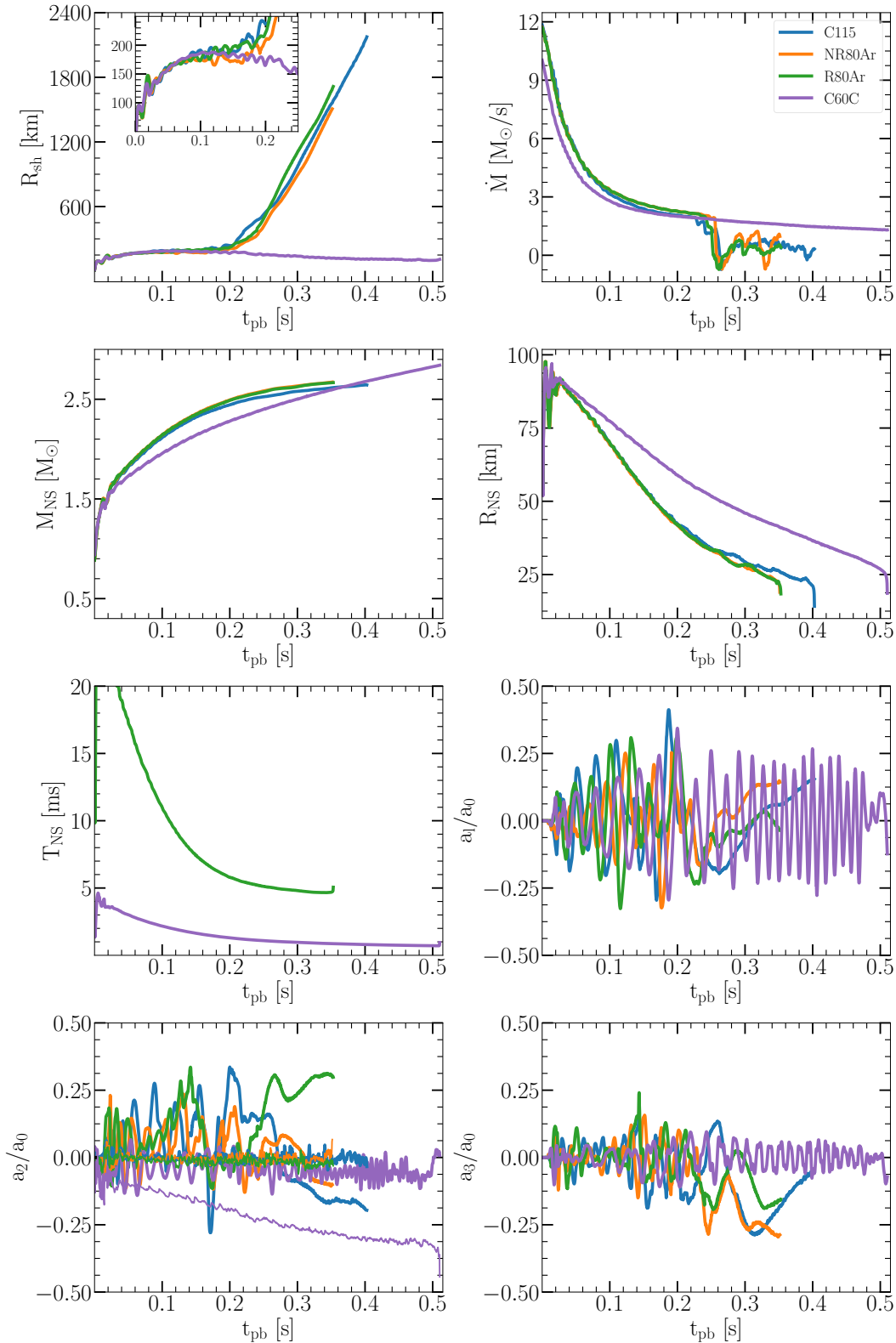
FIGURE 4.3: Shock and neutron star properties. In the top row, we show the time evolution of shock radius (left) and mass accretion rate at r = 500 km (right) for different models. In the second row, we show the time evolution of mass (left) and radius (right) of PNS. In the third row, we show the time evolution of rotational period of PNS (left) and dipole (l=1) component of shock radius (right). In the bottom row, we show the time evolution of quadruple component (l=2) of shock (thick) and PNS (thin) in the left plot and the right plot shows the l=3 component of the shock radius. The C115, NR80Ar, R80Ar and C60C model is represented by blue, orange, green and violet line, respectively.
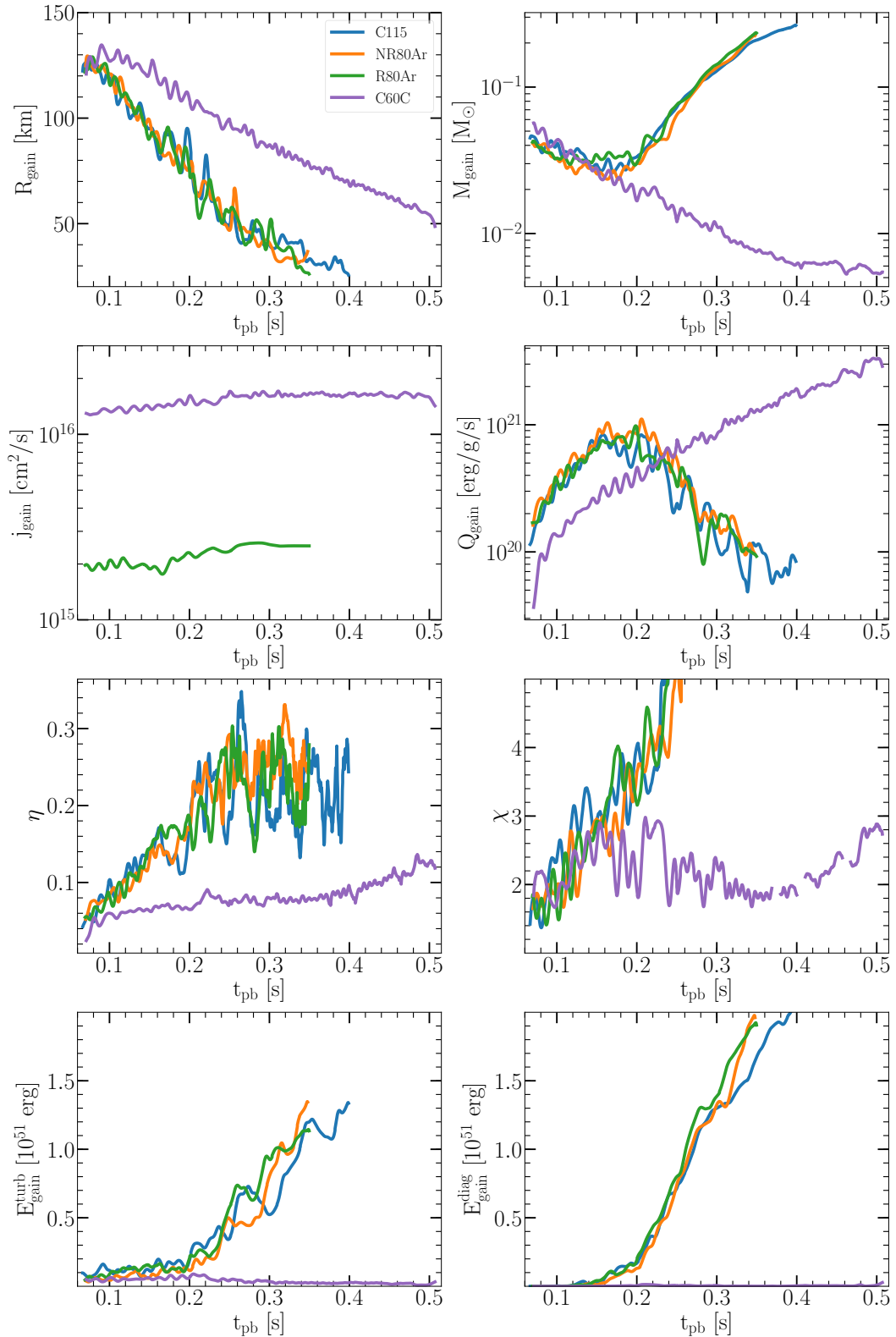
FIGURE 4.4: Gain region properties. In the top row, we show the time evolution of gain radius (left) and gain layer mass (right) for different models. In the second row, we show the time evolution of gain layer specific angular momentum (left) and gain layer heating (right). In the third row, we show the time evolution of heating efficiency (left) and χ parameter (right) in the gain layer. In the bottom row, we show the time evolution of turbulant energy in the left plot and the right plot shows the diagnostic energy of the shock-heated material. The C115, NR80Ar, R80Ar and C60C model is represented by blue, orange, green and violet line, respectively.
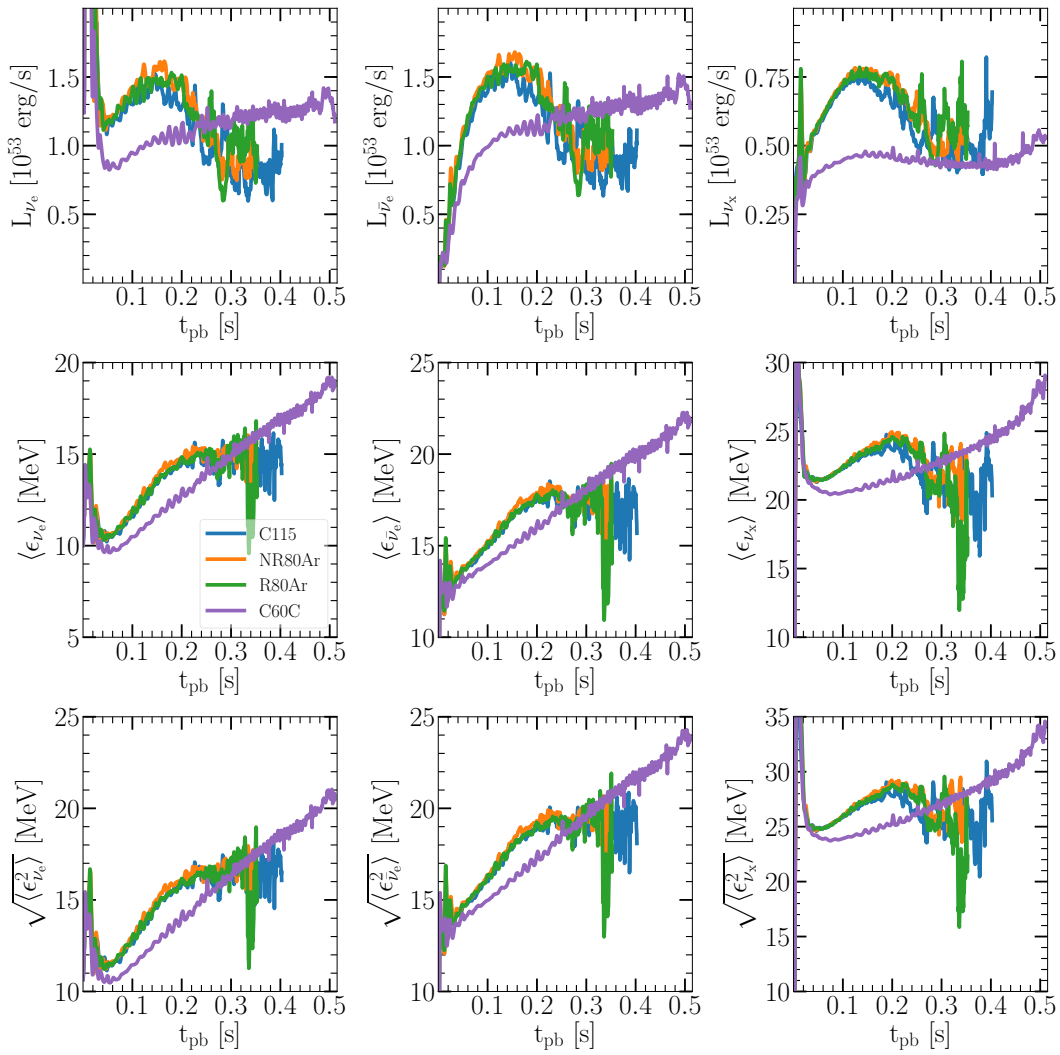
FIGURE 4.5: Neutrino properties. The top row shows the time evolution of luminosities at r = 500 km for ν_e (left), $\bar{\nu}_e$ (middle) and ν_x (right). The middle row shows the time evolution of mean neutrino energies and the bottom row shows the RMS neutrino energies at r = 500 km.
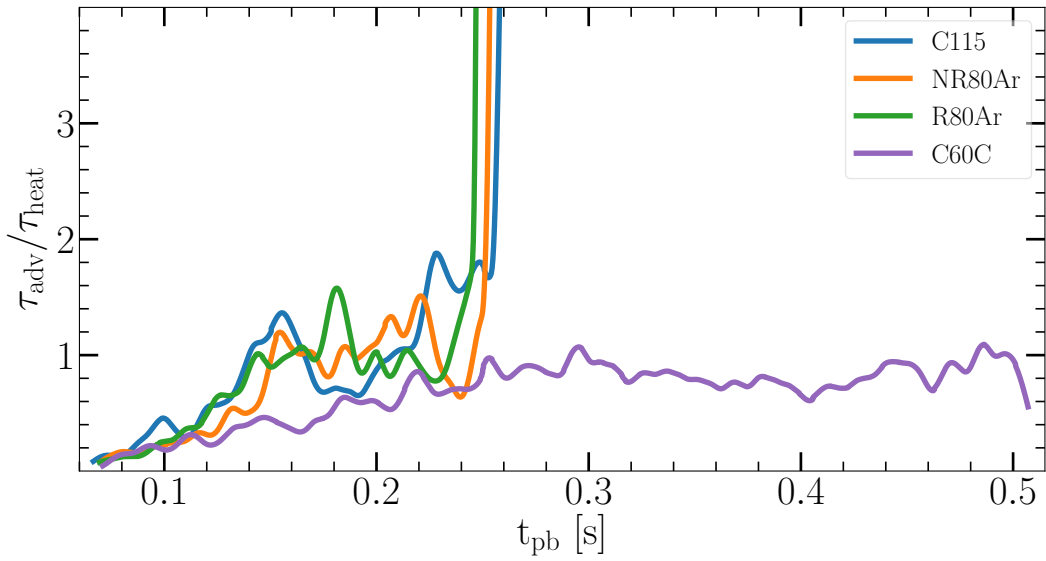
FIGURE 4.6: The ratio of the advection timescale τ_{adv} to heating timescale τ_{heat} in the gain region for different models. The steady shock expansion starts around $t_{\text{pb}} = 0.210$ ms for C115 model and around $t_{\text{pb}} = 0.220$ ms for NR80Ar and R80Ar model. At similar time the timescale ratio crosses 1 for model with shock expansion. The timescale ratio remains below or around 1 for C60C model where no steady shock expansion occur.
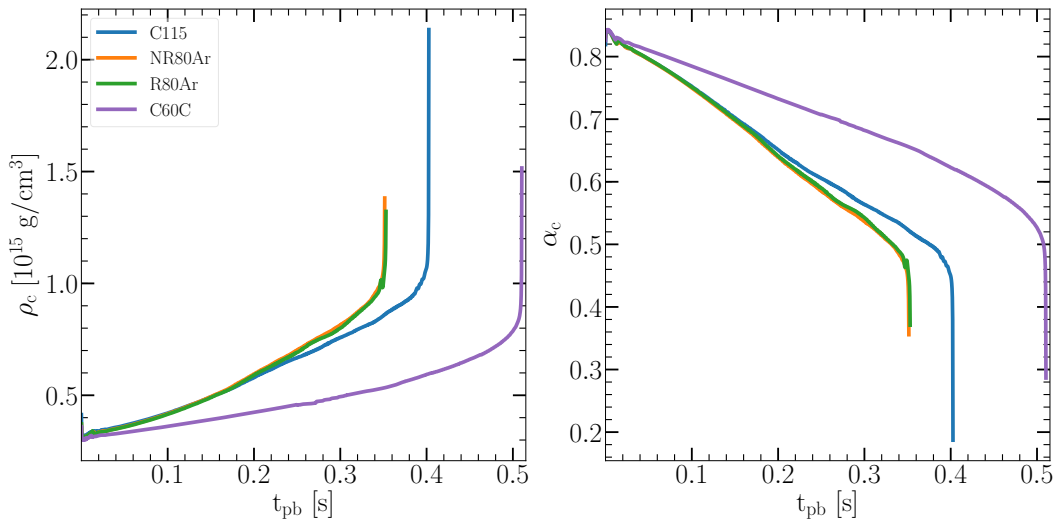
FIGURE 4.7: The time evolution of central baryonic density (left plot) and lapse function. The central density and lapse function show steep rise at the time of BH formation.
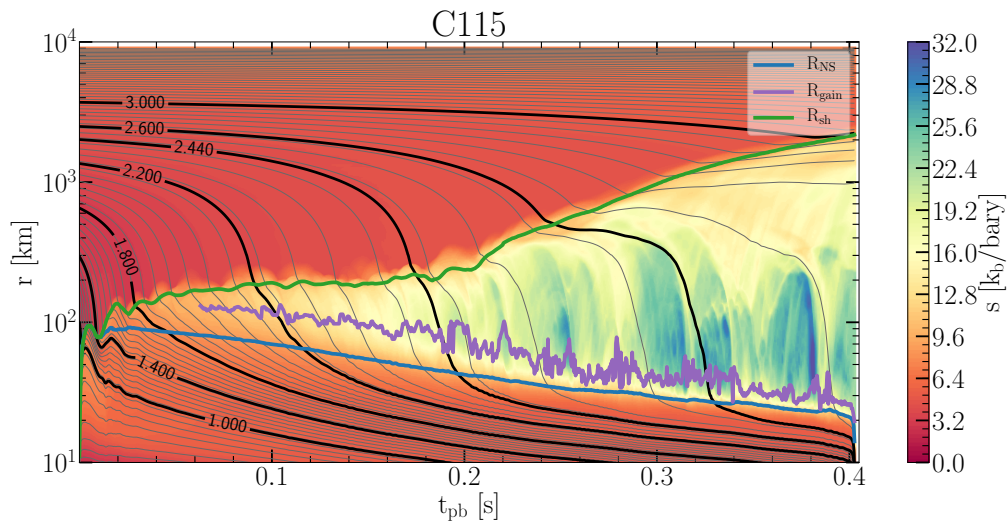
FIGURE 4.8: Mass shell plot of C115 model at different times. The iron core mass is 2.44 M$_\odot$. The entropy per baryon of the gas is color coded.
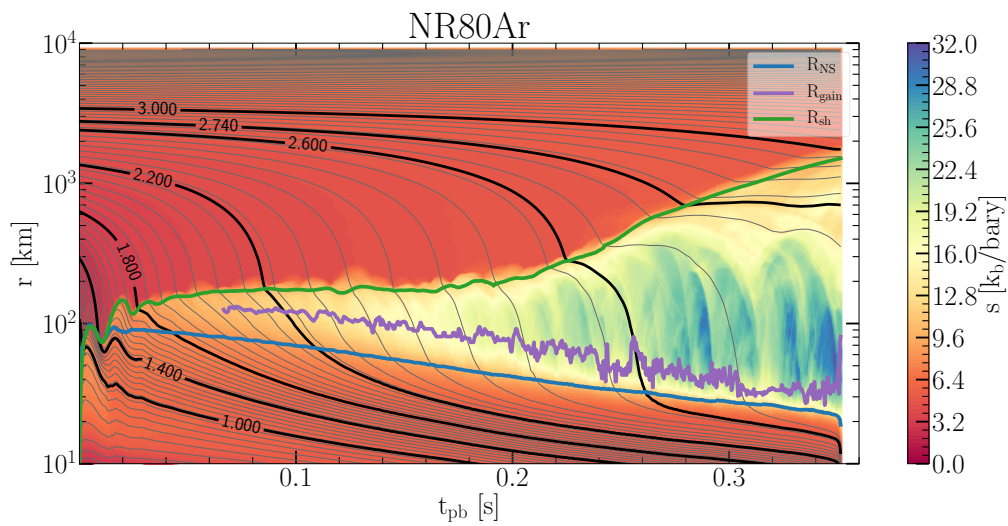
FIGURE 4.9: Mass shell plot of NR80Ar model at different times. The iron core mass is 2.74 M$_\odot$. The entropy per baryon of the gas is color coded.
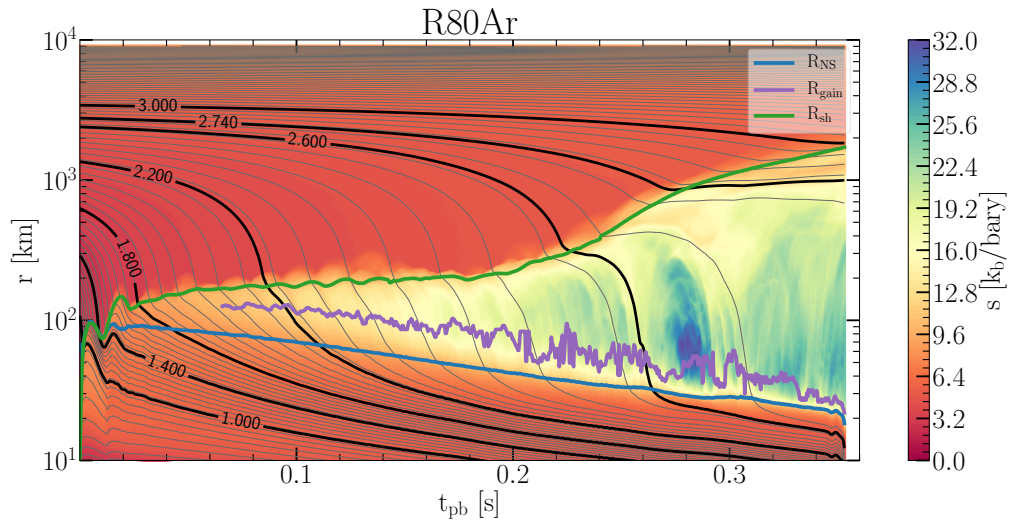
FIGURE 4.10: Mass shell plot of R80Ar model at different times. The iron core mass is 2.74 M$_\odot$. The entropy per baryon of the gas is color coded.
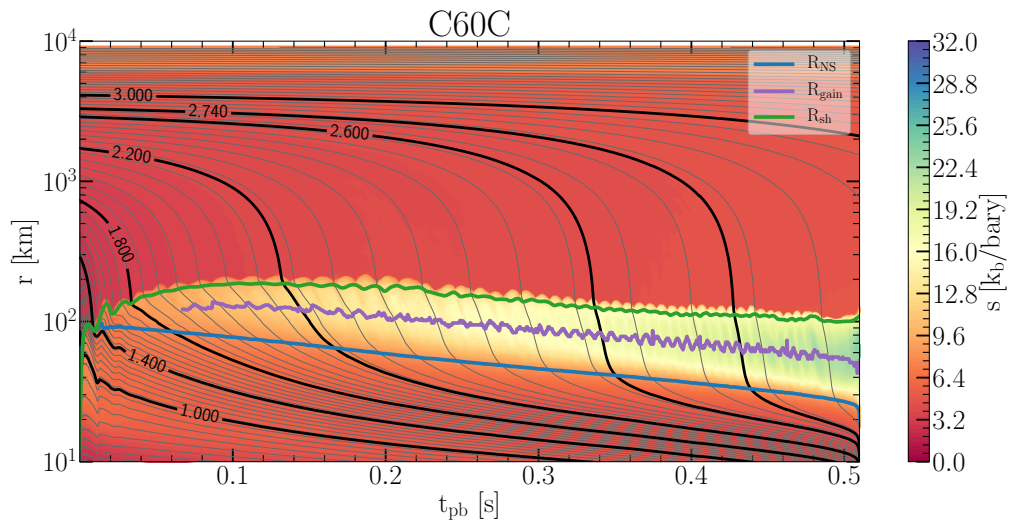
FIGURE 4.11: Mass shell plot of C60C model at different times. The iron core mass is 2.35 M$_\odot$. The entropy per baryon of the gas is color coded.
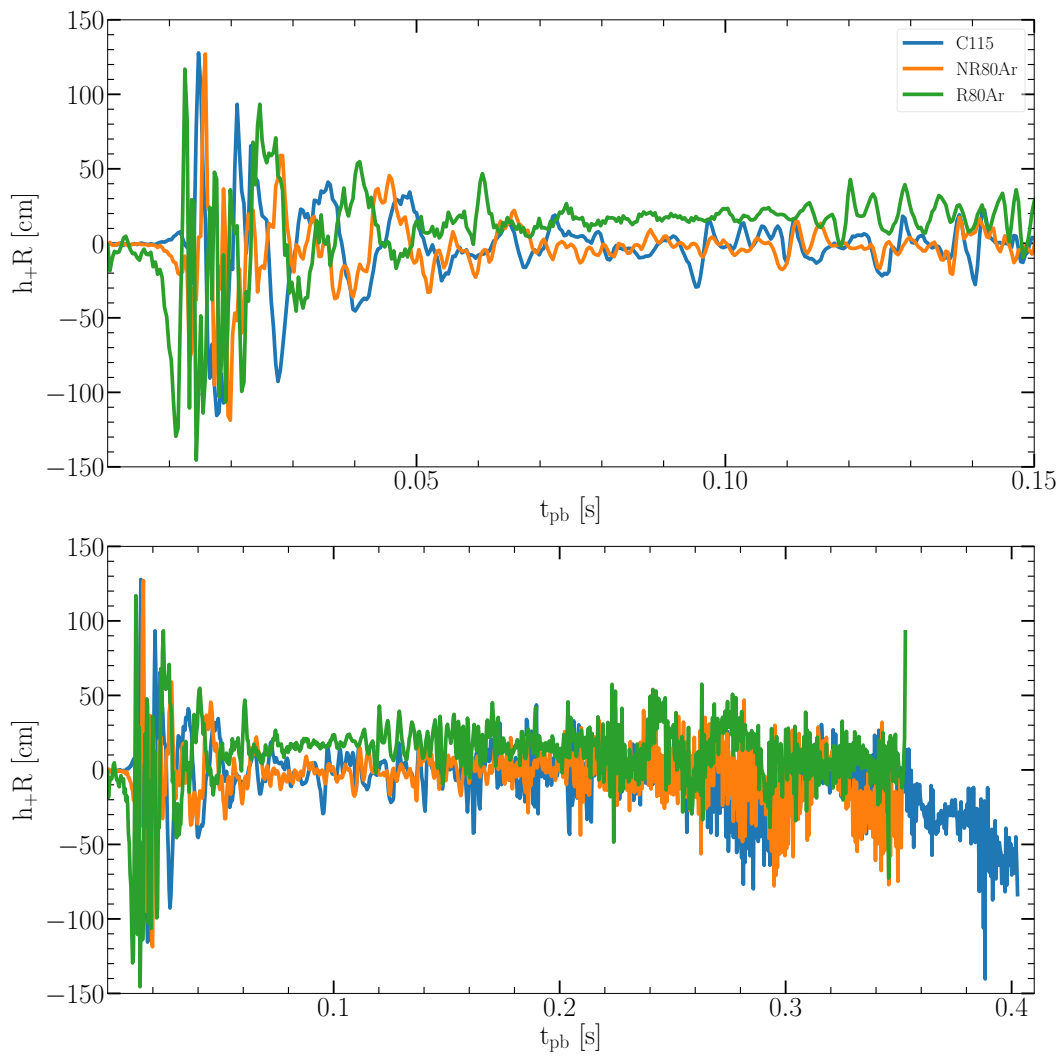
FIGURE 4.12: Gravitational waves. We show the dimensionless strain multiplied by the observer distance for C115, NR80Ar and R80Ar model. The top plot shows only the first 150 ms post-bounce time and the bottom plot shows whole time evolution.
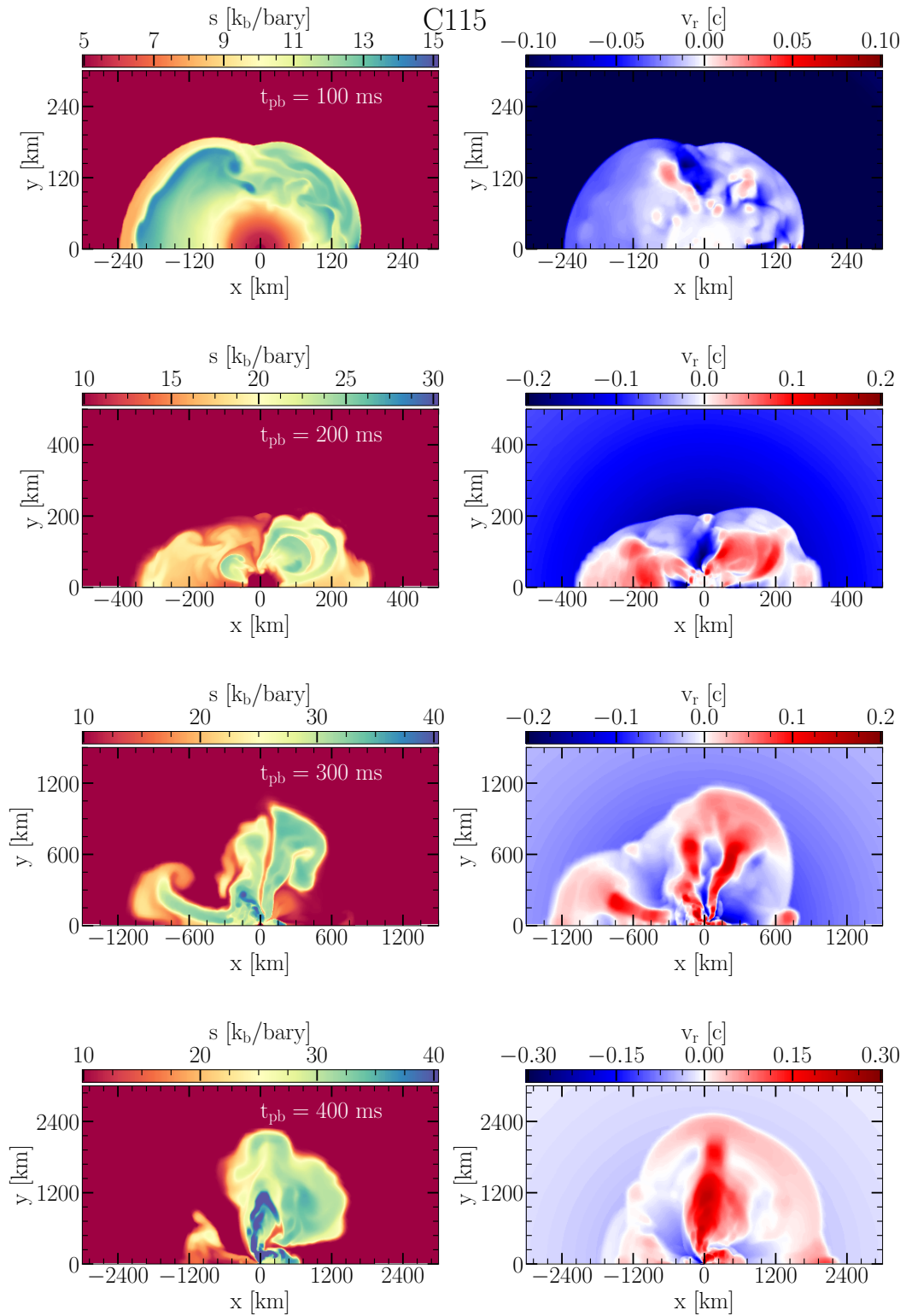
FIGURE 4.13: Plot of entropy per baryon (left column) and radial velocity (right column) of the gas for the model C115 at different times.
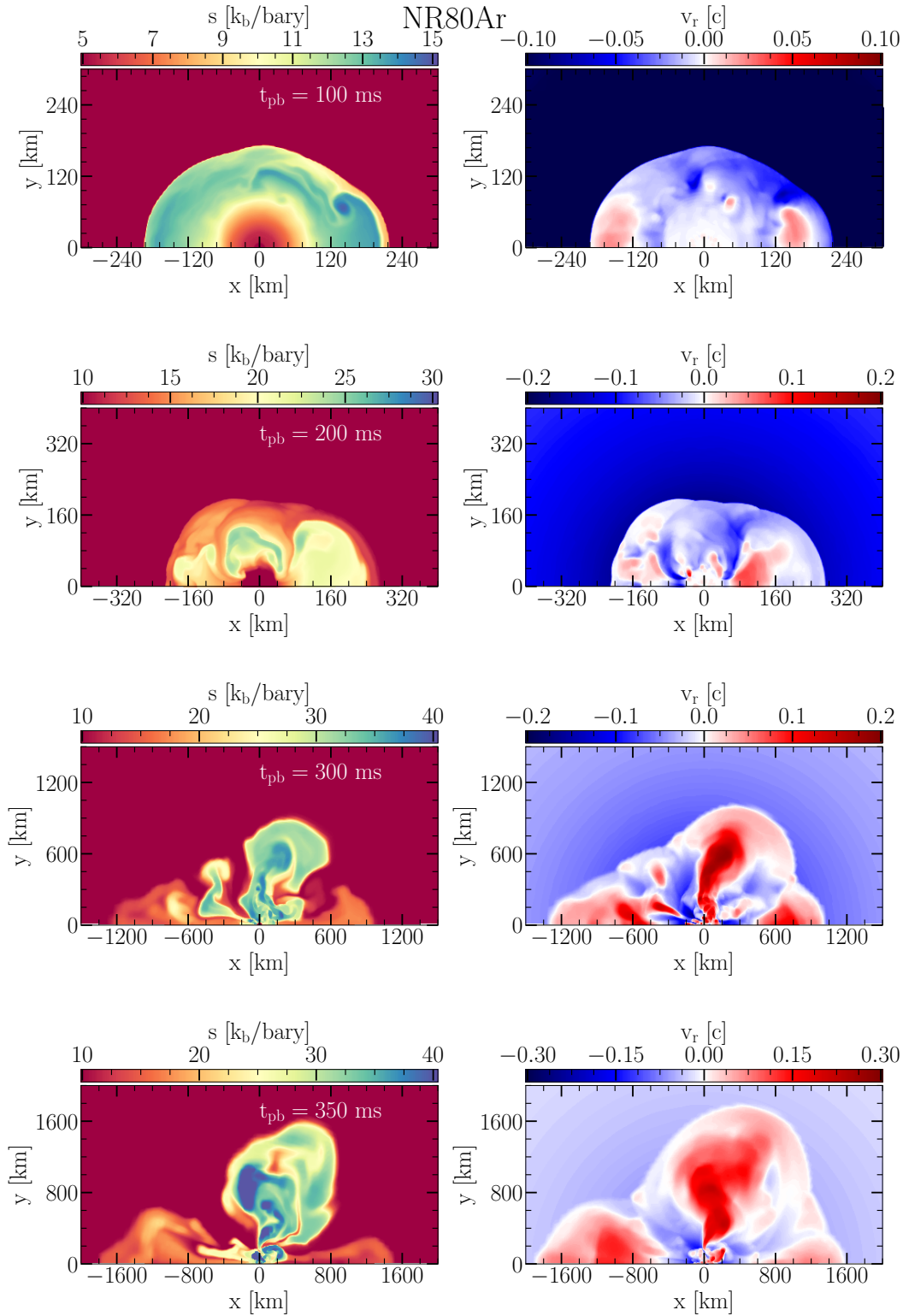
FIGURE 4.14: Plot of entropy per baryon (left column) and radial velocity (right column) of the gas for the model NR80Ar at different times.
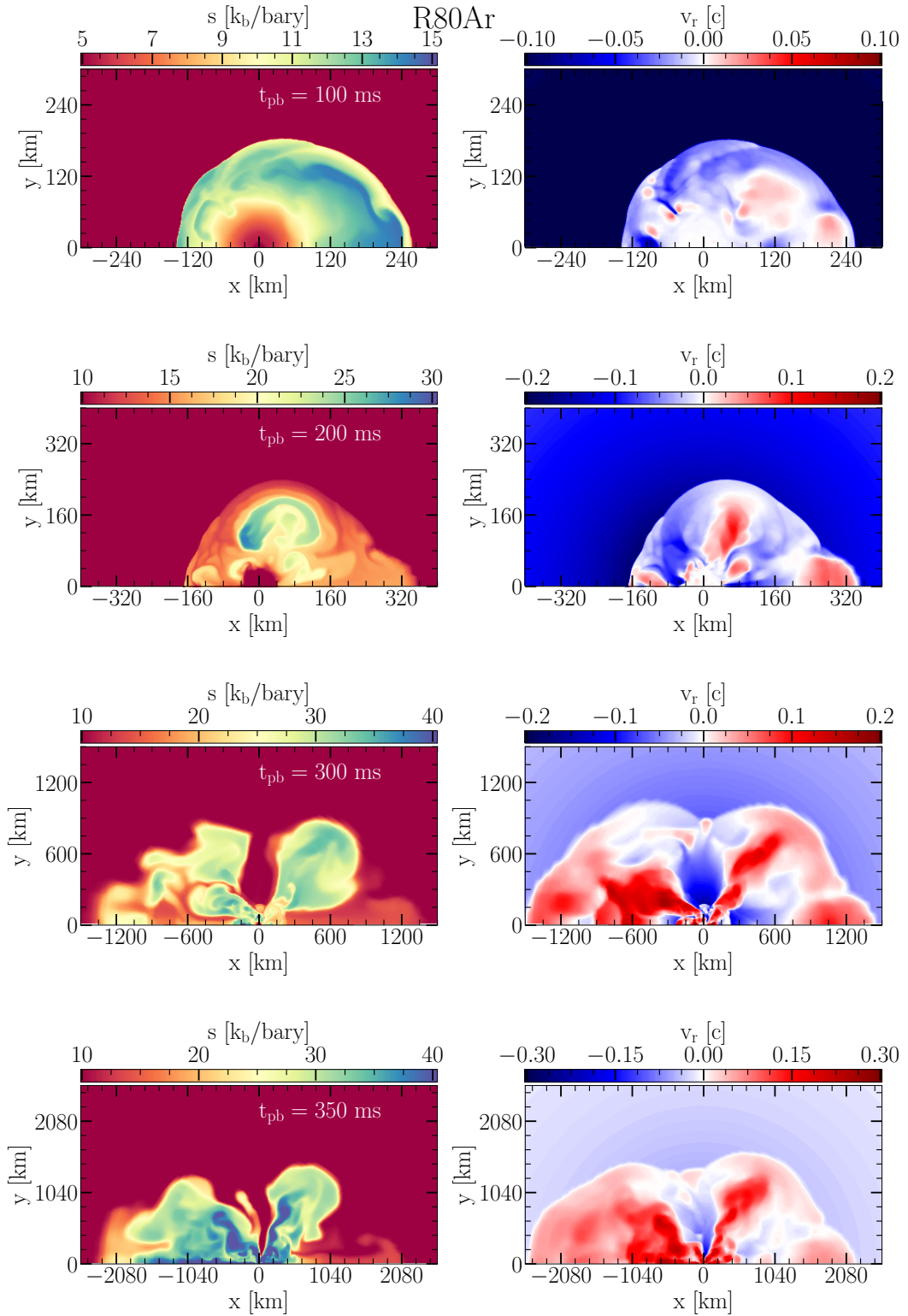
FIGURE 4.15: Plot of entropy per baryon (left column) and radial velocity (right column) of the gas for the model R80Ar at different times.
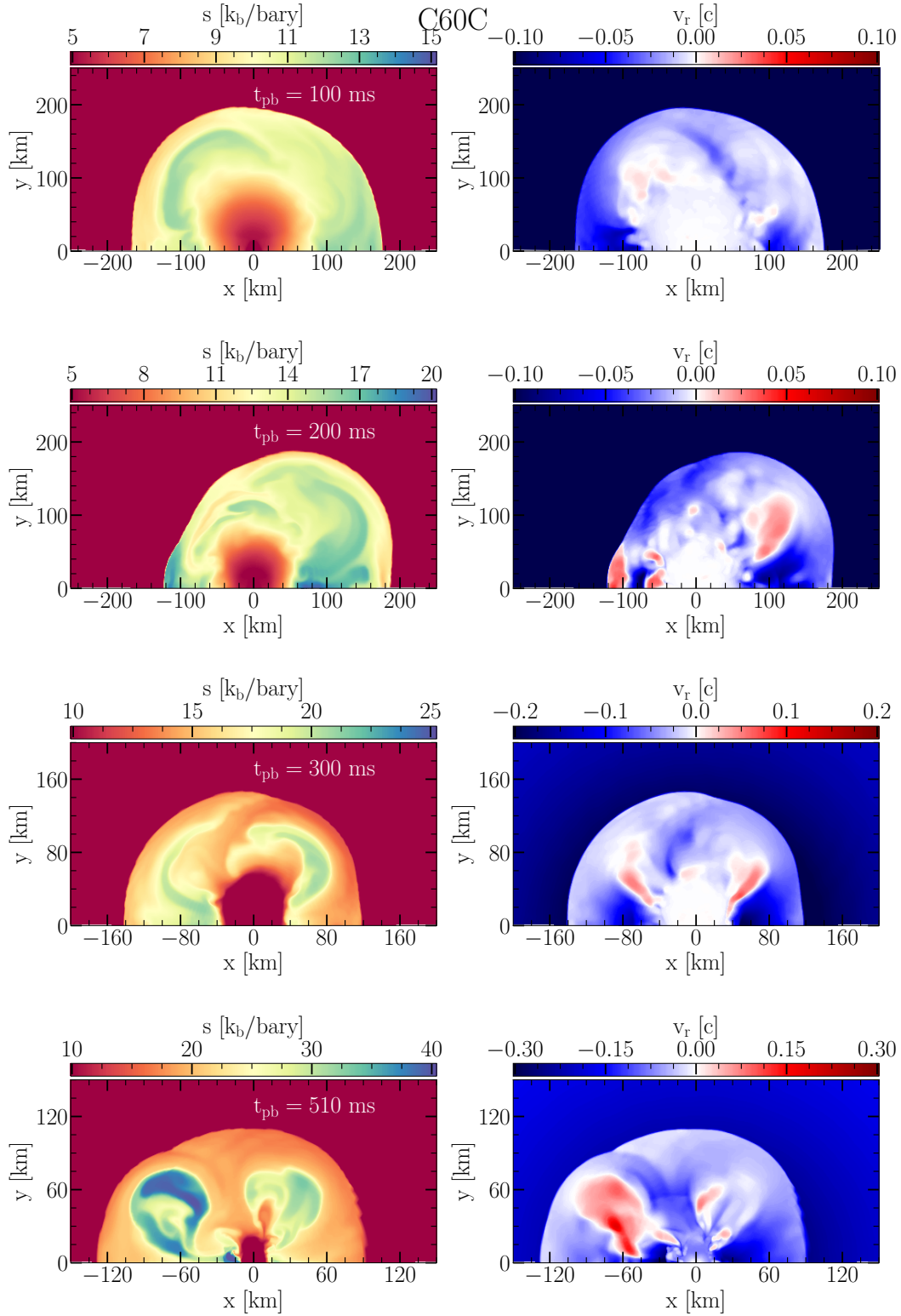
FIGURE 4.16: Plot of entropy per baryon (left column) and radial velocity (right column) of the gas for the model C60C at different times.

energy produces accretion luminosity, L_{acc}. The high neutrino luminosities comes from the high mass accretion of the mentioned model. The accretion luminosity is proportional to the mass accretion rate and the gravitational potential energy of the PNS (see, e.g. Müller and Janka 2014).

$$L_{acc} = \zeta \frac{G\, M_{NS}\, \dot{M}}{R_{NS}}, \tag{4.28}$$

where M_{NS}, R_{NS} are the PNS mass and radius, respectively and $\dot{M}$ is the mass accretion rate. The value of proportionality constant ζ is around 0.45 for all mentioned models. In the top row of Fig. 4.5, we show the neutrino luminosities. The luminosities are about 150 erg/s for the electron type neutrinos in between 100 and 200 ms post-bounce time. In the middle and bottom row of Fig. 4.5, we show the mean and RMS energies of different neutrino species. we observe the rise of neutrino mean and RMS energies which is in agreement with the rapid rise of the PNS mass and rapid contraction of PNS radius (see the left and right plot in the second row of Fig. 4.3).

The gain layer, where the net neutrino heating takes place, is formed at around 70 ms post-bounce time at a radius of around 130 km (see the top left plot of Fig. 4.4). In the right plot of second row of Fig. 4.4, we see the neutrino heating in the gain layer rises to a high value of approximately 6×10^{20} erg/g/s within 150 ms post-bounce time and remains around that high value between 150-200 ms. Since the progenitors have massive iron cores (see Table. 4.1) and due to large shock radius of 200 km, initially the gain layer has large mass of around 5×10^{-2} $M_\odot$ (see the top left plot of Fig. 4.4). The heating per unit mass in the gain layer, Q_{gain}^+, can be coined as (see Müller, Janka, and Marek 2012):

$$Q_{gain}^+ \propto \frac{L_\nu\, \langle \epsilon_\nu^2 \rangle}{R_{gain}^2}, \tag{4.29}$$

where L_ν, $\langle \epsilon_\nu^2 \rangle$ are the luminosity and RMS energy of electron type neutrinos, respectively and M_{gain}, R_{gain} are the gain layer mass and radius, respectively. The high and growing neutrino luminosities and RMS energies and also the high gain layer mass and rapid contraction of the gain radius altogether causes the rise of gain layer heating to a high value. In the right plot of third row of Fig. 4.4, the heating efficiency, defined according to equation (4.20), in gain layer is shown. We observe a high heating efficiency of 10-20%. Due to high heating, the heating timescale, τ_{heat}, in the gain layer eventually becomes shorter then the advection timescale, τ_{adv}, of matter passing through the gain layer. As a result, the shock starts expanding and the mean shock radius crosses 300 km around 210 ms post-bounce time for all above mentioned models. The ratio of the advection and heating timescale crosses 1 around same time as we can see in Fig. 4.6.

The matter behind the shock gains additional energy from the recombination of the free nucleons into α-particle when the shock crosses 300 km. The shock expands rather spherically. Accretion of matter behind the shock continues through several down-flow channels. We observe strong outflow of matter along the poles and equatorial plane. The neutrino heated hot bubble has low density and high temperature associated with high entropy. The hot bubble raises to a higher radial distance due to buoyancy force. The shock velocity increases after the start of shock expansion. Its reaches a steady value of around 10000 km/s within 50 ms after the start of shock expansion.

The mass accretion rate drops after the shock expansion sets in and continues at a smaller rate as we can see from the top right plot of Fig. 4.3. In the right plot of second row of Fig. 4.4, we see the neutrino heating of the shock-heated material continues at a lower rate of $1 - 2 \times 10^{21}$ erg/g/s after shock expansion.

The maximum mass supported by the SFHo equation of state at zero temperature is around 2.059 $M_\odot$ (Steiner, Hempel, and Fischer, 2013). The hot PNS gets additional thermal pressure support to sustain mass above 2.059 $M_\odot$. The PNS mass continues to increase and when the baryonic mass of the PNS crosses 2.66 $M_\odot$ a black hole is formed around 400 ms post-bounce time for the C115 model and 350 ms for the 80 $M_\odot$ rotating and non-rotating models. We see the rotation of the 80 $M_\odot$ model do not impact the black hole formation time, as the weak rotation of this model do not change the mass accretion rate of the PNS.

The interface between the iron core and the Si shell for the C115 model crosses the shock around 180 ms post-bounce time (see the mass shell 2.44 $M_\odot$ in Fig. 4.8), which is before the initiation of the shock expansion (around 210 ms post-bounce time). On the other hand, for the NR80Ar and R80Ar model, the interface crosses the shock around 280 ms post-bounce time (see the mass shell 2.74 $M_\odot$ in Fig. 4.9 and 4.10), which is after the shock expansion have started (around 220 ms post-bounce time). After the shock has crossed 1000 km, the shock deposits enough energy into the crossing mass shells and the crossing mass shells expand outward as can be observed from Fig. 4.9 and 4.10.

In the bottom row of Fig. 4.4, we see the turbulent energy (left plot) and the diagnostic energy (right plot) of the shock-heated material increases steadily after the shock expansion. The diagnostic energy of the shock-heated material for C115 model at the BH formation is around 2.1×10^{51} erg and the overburden energy is around -6.8×10^{51} erg. At the time of BH formation the magnitude of overburden energy is still greater than the diagnostic energy of the shock-heated material. Therefore, it is necessary to conduct simulation after BH formation to see if the diagnostic energy of the shock-heated material can overcome the overburden energy of the material outside shock and the shock expansion leads to successful shock breakout (see, e.g. Bruenn et al. 2013 for discussion about overburden energy and its relevance to explosion). The diagnostic energy for NR80Ar and R80Ar model at the time of BH formation is around 1.9×10^{51} erg and 1.98×10^{51} erg, respectively. The overburden energy is around -9.63×10^{51} erg and -9.54×10^{51} erg, respectively.

The mass accretion rate on to the PNS is slightly higher in the NR80Ar and R80Ar model compared to C115 model. The Rossby number in the gain layer for the rotating R80Ar is around 5-10. We do not see strong impact of the rotation in the post-bounce dynamics for the R80Ar model, which is expected from the high Rossby number in the gain layer. The rotating R80Ar and non-rotating NR80Ar model have similar time evolution. The rotation in the model R80Ar is not strong enough to cause deformation of the PNS as we can see from the quadruple component of the PNS radius deformation (thin line in the bottom-left plot of Fig. 4.3). In the left plot of third row of Fig. 4.3, we see the rotational period decreases from 20 ms (at core bounce) to 5 ms at the black hole formation time for the R80Ar model.

In Fig. 4.12, we show the dimensionless strain of the gravitational wave, h_+, multiplied by the observer distance R for C115, NR80Ar and R80Ar model. The top plot show early 150 ms post-bounce time and the bottom plot shows the whole time evolution of the dimensionless strain. In the early phase ($t_{pb} < 30$ ms), we see the gravitational wave due to prompt PNS convection. Afterwards, we see the low frequency gravitational wave due to SASI sloshing motion. The SASI motion stops around $t_{pb} = 150$ ms and the hot-bubble convection due to strong neutrino heating starts to

dominate the fluid motion. Therefore, we see the high frequency gravitational wave characterizing hot-bubble convection. After the start of shock expansion, the C115 and NR80Ar model has strong outflow of material in the equatorial plane and the shock-heated material have oblate shape as we can see from Fig. 4.13 and 4.14. This aspherical shock expansion leads to "memory" signature in the gravitational wave strain (see, e.g. Favata 2010 for a review about the gravitation wave memory effect). As a result, we see the negative value of dimensionless strain for C115 and NR80Ar model. The dimensionless strain is positive for R80Ar model because in this model the shock-heated material has prolate shape (strong outflow along the polar axes) as we can see from Fig. 4.15 (see, e.g. Murphy, Ott, and Burrows 2009 for discussion about gravitational wave produced by different fluid instabilities in 2D).

The C60C model is rapidly rotating. This model gains some centrifugal support against gravity due to its rapid rotation. As a result the PNS has larger mean radius in C60C model. In the bottom-right plot of Fig. 4.3, we see the quadruple component of the PNS radius for C60C model (thin violet line) has large values, 10-25% of the mean radius of the PNS. The PNS has a oblate shape. The C60C model also has slightly lower mass accretion rate (see the top-right plot of Fig. 4.3) in the early phase ($t_{pb} <$ 100ms). In the top-left plot of Fig. 4.3, the early shock expansion after bounce stops at 120-130 km at 20 ms post-bounce time. Afterwards, the shock steadily expands to approximately 190 km and then the shock starts to contract. In the right plot of third row of Fig. 4.4, we see neutrino heating efficiency, η, remains at lower values compared to models where shock expansion occur (e.g. C115, NR80Ar, R80Ar). The shock is not revived by neutrino heating in this model. The SASI sloshing motion survives in this model until the BH formation, which is reflected in the value of χ parameter in the right plot of third row of Fig. 4.4. The χ parameter remain below 3 until the BH formation. In the top-right plot of Fig. 4.3, we see the mass accretion rate continues at a high value. Eventually, a BH is formed around 510 ms post-bounce time when the baryonic mass of the PNS is around 2.88 $M_\odot$. The PNS can support additional mass due to high temperature and rapid rotation. High temperature creates thermal pressure support and rapid rotation creates centrifugal support against gravity. In the left plot of third row of Fig. 4.3, we see the rotational period of PNS is around 3-4 ms at the time of BH formation. The kerr parameter of the newly born BH can be estimated as:

$$a_{BH} = \frac{J_{NS,BHF}\, c}{G\, M_{NS,BHF}^2}, \tag{4.30}$$

where $J_{NS,BHF}$, $M_{NS,BHF}$ are the total angular momentum and mass of the PNS at the time of BH formation. We obtained a value of 0.66 for a_{BH}.

4.5   Results: after black hole formation

We continued our simulation after BH formation. For this study, we used NR80Ar model and applied Cowling approximation (kept metric fixed with time). We conducted the simulation until $\sim$ 1 s post-bounce time. The initial gravitating mass of the BH is around 2.58 $M_\odot$. In the left plot of Fig. 4.17, we see the BH mass increases with time and at the end of simulation BH has accreted 0.6 $M_\odot$ baryonic mass. The left plot of middle row of Fig. 4.17 shows the mass accretion at 500 km radial distance. The mass accretion rate remains at a high value of $\sim$ 0.8 $M_\odot$/s and the accretion flow near BH is supersonic.
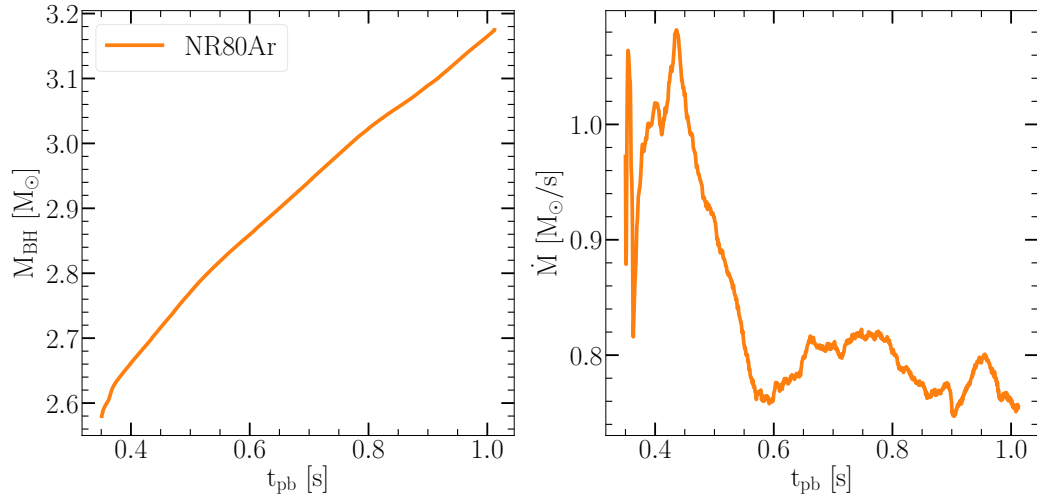
FIGURE 4.17: Time evolution of the black hole mass (left plot) and mass accretion rate at a radial distance of 500 km (right plot).
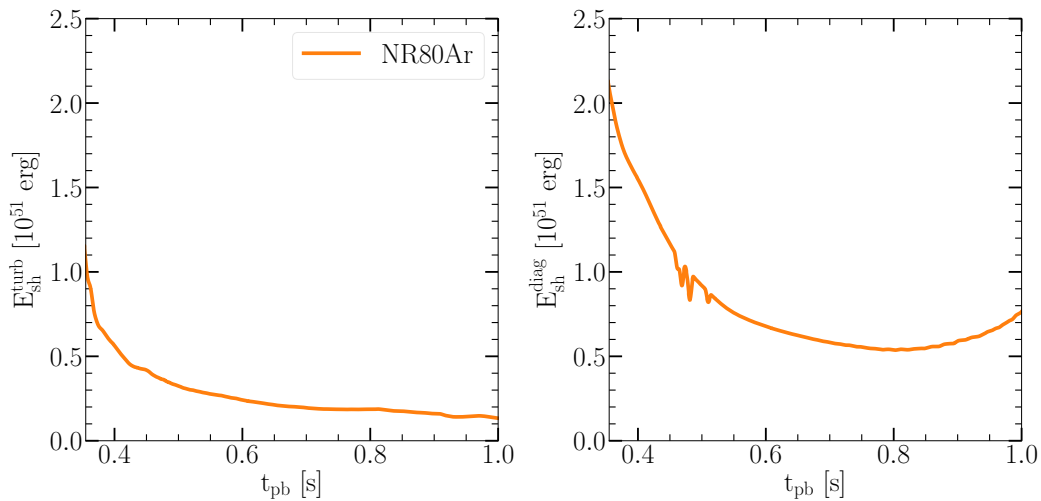
FIGURE 4.18: Time evolution of the turbulent kinetic energy (left plot) and the diagnostic energy (right plot) of shock-heated material after BH formation.
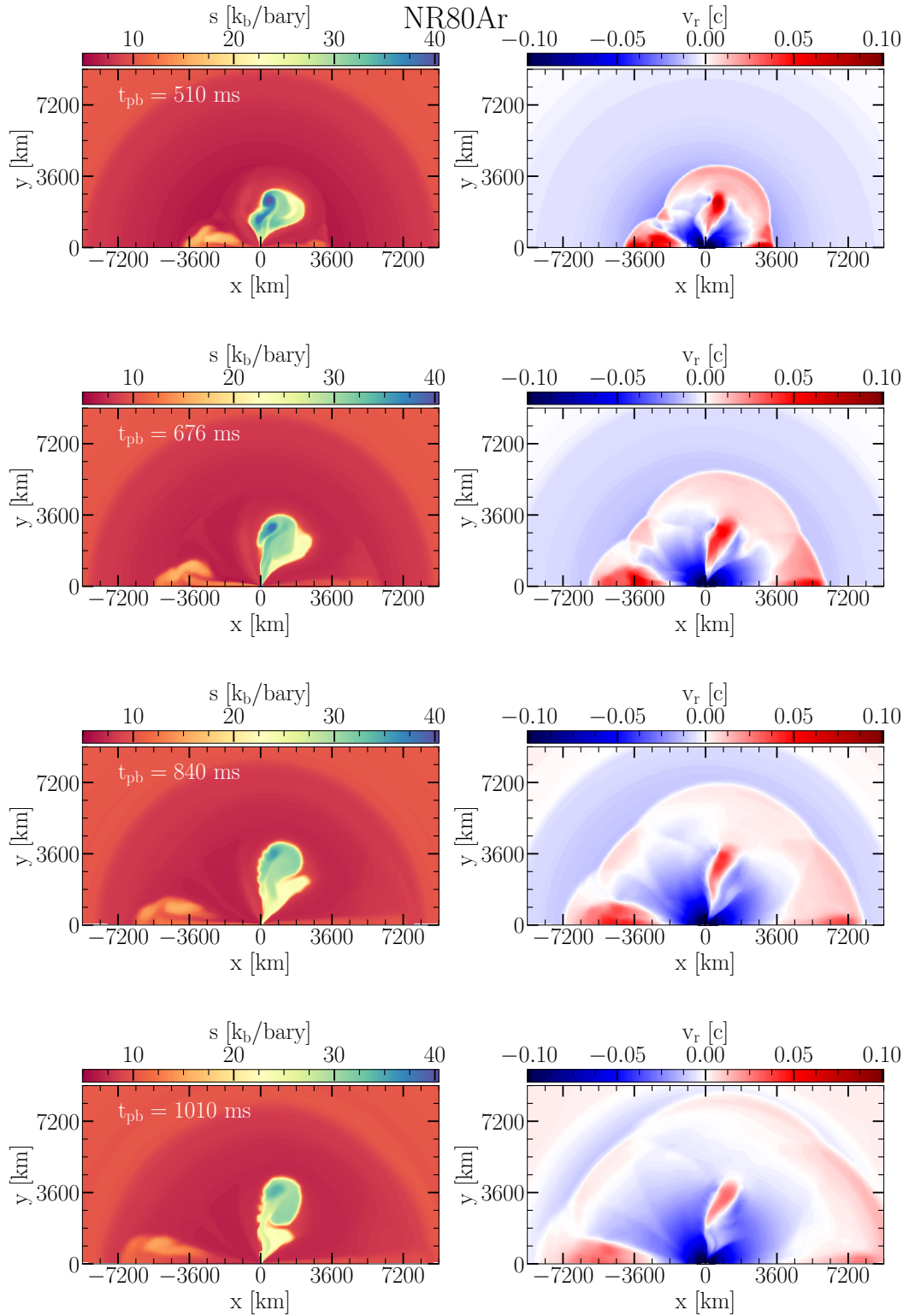
FIGURE 4.19: Entropy (left column) and radial velocity (right column) plot of the NR80Ar model at different times after BH formation.
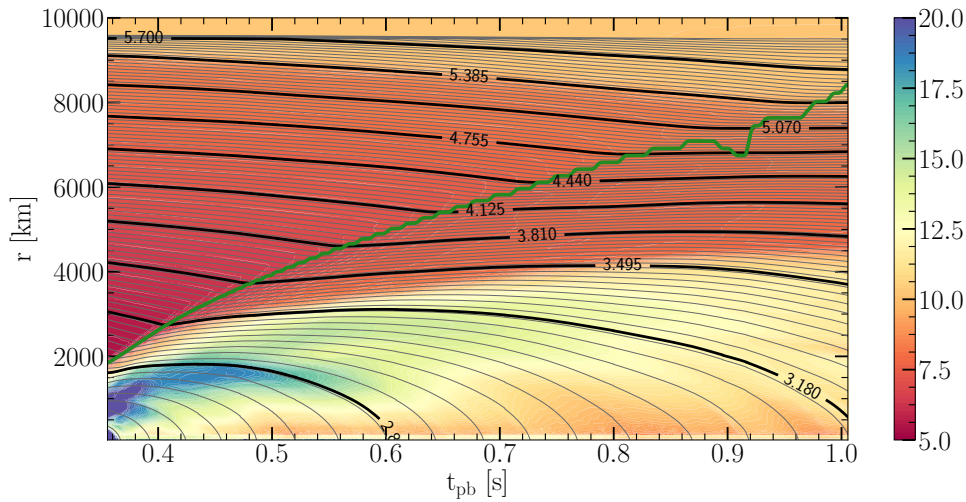
FIGURE 4.20: Mass shell plot of NR80Ar model at different times after BH formation.

In Fig. 4.18, we see that the turbulent kinetic energy (left plot) and the diagnostic energy of shock-heated material after BH formation decline. At the end of simulation, the diagnostic energy is around 0.8×10^{51} erg, which is lower than the overburden energy (-7.7×10^{51} erg) of material ahead of the shock.

In Fig. 4.20, we show the mass shell plot for NR80Ar model after BH formation along with shock radius. As a mass shell crosses the expanding shock, the shock transfer enough energy to that mass shell and infalling mass shell expands initially. Eventually, expansion of mass shell is stopped and it falls back onto BH. When the shock reaches 7000 km, infalling mass shells through the shock no longer experience expansion. The shock becomes spherical as it propagates outward. The steady shock velocity of around 9500 km/s is maintained after BH formation. The information about BH formation at the center propagate via rarefaction wave which travel at sound's speed. In our simulation, we observe the shock-heated material has a sound speed of around 9000 km/s. Until the end of the simulation, the rarefaction wave has not reached the shock. The shock continued to expand until the end of simulation and average shock radius has a value of 8500 km (still inside Si-O shell). A long-term simulation is required to see the final fate of the shock, does it continue to grow or fall back into the BH?

In Fig. 4.19, we show the entropy (left) and the radial velocity (right) of NR80Ar model at 510, 676, 840 and 1010 ms post-bounce time. After the BH formation, the outflow of matter from the central object is stopped but the equatorial and polar hot-bubbles (high entropy material) continue to expand. Density of the hot-bubbles is lower compared to its surrounding. As a result, the hot-bubbles experiences buoyancy force and rise radially outward. We see strong accretion flows surrounding the rising hot-bubbles. The expanding hot bubbles have high pressure compared to their surrounding material. The expanding bubbles transfer energy and momentum to the surrounding material through mechanical work. Chan et al. (2018) claimed based on their simulation after BH formation, that the surrounding material can obtain radially outward velocity if sufficient energy and momentum is transferred from the initial neutrino heated hot-bubble. Eventually, the original neutrino heated hot-bubble falls back to BH but the shock continues to expand in Chan et al. (2018). At the end of our simulation, the hot-bubbles have not fallen into BH. Although, matter continues to fall into BH from the bottom of hot-bubble. The outer radius of

the equatorial hot-bubble is around 5000 km at the end of our simulation. Further long-term simulation is required to see whether the equatorial hot-bubble can rise outward as the density of surrounding material drops.

As mentioned before, we conduct our simulation after BH formation in Cowling approximation. As a result, we underestimate gravitational force, which in turn favors shock expansion. The Cowling approximation also prohibits us from continuing the simulation further as the mass of BH has increased by 20%.

Another approximation we made is that we conduct our simulation in two dimension. The difference between 2D and 3D explosion dynamics after shock revival have been studied by (Müller, 2015). In two dimension, the equatorial outflow will represent (see, Fig. 4.19) a toroidal shape if it is mapped to three dimension. As a result, the equatorial outflow in two dimension have to do more mechanical work, which is proportional to surface area of outflow, compared to a three-dimensional equatorial outflow. The two-dimensionality of the equatorial outflow disfavors its expansion.

Chapter 5

Conclusion

In this work, we presented a new code to solve multi-dimensional neutrino-transport in spherical polar coordinates and coupled to fully general relativistic hydrodynamics code (Baumgarte et al., 2013; Montero, Baumgarte, and Müller, 2014). The transport solver assumes the flux-limited diffusion approximation and evolves the neutrino energy densities as measured in the frame comoving with the fluid. In order to improve the computational efficiency and parallel scalability compared to a scheme that solves the multi-dimensional FLD equations in a single, unsplit step, we employ operator splitting such that different parts of the equations (and different coordinate directions) are dealt with in separate, consecutive steps. The source terms as well as the radial- and energy-derivatives are integrated implicitly, while the non-radial derivatives are integrated explicitly using the Allen-Cheng method (Allen, 1970).

We tested the algorithm and its implementation by investigating several problems in 1D and 2D and comparing to reference solutions. The tests demonstrate that the code runs stably and it robustly handles diffusion, transition to free-streaming, energy-bin coupling, multi-dimensional transport, microphysical neutrino interactions, and the coupling to GR-hydro. We confirmed that the Allen-Cheng method is, in contrast to conventional explicit schemes, unconditionally stable even if the diffusion timescale of a grid cell is shorter than the time step used for integration. However, estimates showed that such situations are expected to appear in multidimensional CCSN simulations only near the center of the PNS or close to the shock, i.e. at locations where lateral neutrino fluxes are strongly subdominant.

In terms of physics ingredients the most sophisticated tests performed here consider the core collapse and post-bounce evolution of a massive star in spherical symmetry. We compared a Newtonian version of this configuration with the results of the M1 code ALCAR (Just, Obergaulinger, and Janka, 2015; Just et al., 2018) and found that most global properties agree remarkably well, namely within $5 - 10\,\%$ for some quantities (e.g., the maximum shock radius and even better for most other quantities). We also compared the Newtonian simulation with its GR counterpart and were able to confirm the tendency of GR (e.g. Bruenn, De Nisco, and Mezzacappa, 2001; Marek et al., 2006; Müller, Janka, and Marek, 2012; O'Connor and Couch, 2018) to lead to an overall more compact post-bounce configuration along with higher neutrino luminosities and mean energies. A final comparison of the GR simulation using the Levermore-Pomraning (LP) flux-limiter with another GR simulation using the Wilson limiter revealed quite significant differences. But we see good agreement of the LP simulation with the ALCAR simulation.

We applied our newly developed general relativistic radiation hydrodynamics code for core-collapse simulations of very massive stars ($\sim 100 M_\odot$; see, Vink 2015 for definition of very massive star). We used very massive star progenitors with ZAMS masses of 60, 80 and 100 $M_\odot$ from (Woosley, 2017), denoted by C60C, R80Ar and C115, respectively. The 60 $M_\odot$ mass progenitor is rapidly rotating and 80 $M_\odot$

mass model has slow rotation. We have also conducted a simulation of this 80 $M_\odot$ progenitor without rotation (model NR80Ar) to discriminate the effect of rotation. The 115 $M_\odot$ mass progenitor is non-rotating.

All models studied in this work have high mass accretion rate of the new born NS. Strong SASI activity (see, e.g. Foglizzo, Scheck, and Janka 2006 for discussion about SASI) is seen in all models. Due to the high mass accretion rates, the neutrino luminosities are high, which in turn causes strong neutrino heating. The shock is revived because of thus strong neutrino heating with the aid of hydrodynamical instabilities in model C115, NR80Ar and R80Ar (see Fig. 4.3). Before shock revival all these models show convective activity. Rotation does not have strong impact on the dynamics of the 80 $M_\odot$ mass model. However, the shock-heated material have a prolate shape in rotating model (see Fig. 4.15) and is slightly oblate in non-rotating model (see Fig. 4.14). As a result, the gravitational wave (GW) amplitudes have opposite sign in these two models (see Fig. 4.12) after explosion due to the GW memory effect (see, e.g. Favata 2010). The rapidly rotating C60 model does not show shock revival and eventually a rotating BH is formed with Kerr parameter of 0.66. After shock revival in C115, NR80Ar and R80Ar model, BHs are formed due to continuous accretion through accretion downdrafts. At the time of BH formation, the revived shock is at $\sim$ 2000 km and expands with a velocity of 10,000 km/s.

We continued our simulation after BH formation in model NR80Ar. We see that the mass-accretion rate into the BH is around 0.8 $M_\odot$/s and the accretion into the BH is supersonic. The shock continues to expand after BH formation. As the shock expands, it becomes more spherical (see Fig. 4.19). At the end of simulation, the shock is around 8500 km. The mass shells falling through the shock get heated by the shock and expand initially but eventually fall towards the BH (see Fig. 4.20). The high-entropy bubbles continue to rise after BH formation due to buoyancy forces as they have lower density compared to their surrounding material. The expanding high-pressure hot-bubbles transfer energy to the surrounding material by expansion work. The information about BH formation at the center propagates through fluid medium by a rarefaction wave. At the end of simulation this rarefaction wave has not reached the shock.

At the end of simulation of model NR80Ar, the shock is at 8500 km, still inside Si-O layer. Further continuation of the simulation is required to see the final fate of the shock and of the shock-heated material, whether they fall back into the BH or expand through the outer layers of the star causing shock breakout and the ejecta of some near-surface matter in an explosion-like event. Simulations after BH formation are also required to see the evolution of the shock for model C115 and the rotating model R80Ar and rapidly rotating model C60C. A Long-term simulation of C60C model is needed to see whether an accretion disk is formed around the BH. If an accretion disk is indeed formed, it might serve as a central engine of collapser model (see, e.g. Woosley 1993; MacFadyen and Woosley 1999).

Recently, Bollig et al. (2017) have shown the muonization, which is neglected in this study, of hot PNS matter can soften the equation of state, hence triggering faster contraction of the PNS. As a result, neutrino luminosities and mean energies increase, leading to enhanced heating in gain layer. Muonization can affect both shock revival and BH formation. This effect is more pronounced in more massive and thus hotter PNSs. Hence, muonization might have strong impact in CCSNe of very massive stars where more massive and hotter PNS are formed. So, a study with muons and muon type neutrinos of CCSN of very massive star is required.

In previous years, several 3D simulations of CCSN have been conducted by different groups (see, e.g. Lentz et al. 2015; Melson et al. 2015; Melson, Janka, and

Marek 2015; Roberts et al. 2016; OConnor and Couch 2018; Summa et al. 2018). The dynamics of the shock and flow geometry can be quite different in 2D and 3D (see. e.g. Hanke et al. 2013; Müller 2015). In 3D, spiral SASI mode can develop in addition to sloshing SASI motions. Since our models show strong SASI activity, inclusion of spiral mode instabilities may alter the outcome of simulations. Also, the outflow in 2D after shock revival represents a toroidal structure because of the assumed axisymmetry in 2D. As a result, the hot-bubbles need to do overestimated pressure-volume work for their expansion and their buoyant rise is disfavored. Hence, a 3D study of CCSNe of very massive stars is needed.

Appendix A

Derivation of energy equation in co-moving frame

The transport equation used in our code evolves the energy density, $\mathcal{J}$, measured in an orthonormal comoving frame. This Appendix shows how this evolution equation can be obtained from corresponding equations evolving the lab-frame moments, E and F^i. The lab-frame equations are derived and discussed in Shibata et al. (2011), Endeve, Cardall, and Mezzacappa (2012), and Cardall, Endeve, and Mezzacappa (2013). In Table A.1 we summarize the meaning of various quantities used here and where to find more information about them. The lab-frame equations contain the quantities, G, I^a, P^{ab}, Q^{abc}, which are related to the third-moment tensor,

$$\mathcal{U}^{abc} \equiv \epsilon^3 \int l^a l^b l^c f(x^\mu, p^{\hat{\mu}}) \mathrm{d}\Omega \, , \tag{A.1}$$

by

$$\mathcal{U}^{abc} = G n^a n^b n^c + I^a n^b n^c + I^b n^a n^c + I^c n^a n^b + P^{ab} n^c + P^{bc} n^a + P^{ac} n^b + Q^{abc}. \tag{A.2}$$

We start from the lab-frame neutrino-energy equation as given in conservative form by equations (171), (91-93), (146), (147), and (173) of Cardall, Endeve, and Mezzacappa (2013):

$$\frac{1}{\sqrt{-g}} \frac{\partial}{\partial t} (\sqrt{\gamma} \mathcal{E}) + \frac{1}{\sqrt{-g}} \frac{\partial}{\partial x^j} \{\sqrt{\gamma}(\alpha \mathcal{F}^j - \beta^j \mathcal{E})\} + \mathcal{F}^j \frac{\partial \ln \alpha}{\partial x^j} - \mathcal{S}^{jk} K_{jk} - \frac{1}{\epsilon^2} \frac{\partial}{\partial \epsilon} (\epsilon^2 F^\epsilon)$$

$$= -n_\mu \frac{1}{\epsilon} \int p^\mu C \mathrm{d}\Omega \, . \tag{A.3}$$

The definition of different symbols can be found in Table A.1. Here,

$$
\begin{aligned}
F^\epsilon \quad \equiv \quad & W\{I_j \frac{\partial v^j}{\partial \tau} + P_j^{\ k} \frac{\partial v^j}{\partial x^k} + \frac{1}{2} P^{jk} v^l \frac{\partial \gamma_{jk}}{\partial x^l} + (I^j - G v^j) \frac{\partial \ln \alpha}{\partial x^j} - P^{jk} K_{jk} + v^j I_k \frac{1}{\alpha} \frac{\partial \beta^k}{\partial x^j}\} \\
& + (I_j v^j - G) \frac{\partial W}{\partial \tau} + (P_k^{\ j} v^k - I^j) \frac{\partial W}{\partial x^j} \, ,
\end{aligned}
\tag{A.4}
$$

with $\frac{\partial}{\partial \tau} \equiv n^a \frac{\partial}{\partial x^a}$. Equations (A.3) and (A.4) are copied directly from Cardall, Endeve, and Mezzacappa (2013), who employs slightly different definitions than us concerning the power of ϵ in the prefactor of the angular moments and third-moment projections. We now switch to our notation by doing the replacements $\epsilon^2\{\mathcal{E}, \mathcal{F}^i, \mathcal{S}^{ij}, \mathcal{L}^{ijk}\} \rightarrow \{\mathcal{E}, \mathcal{F}^i, \mathcal{S}^{ij}, \mathcal{L}^{ijk}\}$ and $\epsilon\{G, I^i, P^{ij}, Q^{ijk}\} \rightarrow \{G, I^i, P^{ij}, Q^{ijk}\}$. Moreover, we multiply

TABLE A.1: Meaning of various quantities used in Appendix A and where to find their computation. The quantities G, I^a, P^{ab}, Q^{abc} used here are denoted by $\mathcal{G}, \mathcal{I}^a, \mathcal{P}^{ab}, \mathcal{Q}^{abc}$ in Endeve, Cardall, and Mezzacappa (2012) and by $\mathcal{Z}, \mathcal{Y}^a, \mathcal{X}^{ab}, \mathcal{W}^{abc}$ in Cardall, Endeve, and Mezzacappa (2013), respectively. Also, note that all angular moments (projections of $\mathcal{U}^{abc}$) in Endeve, Cardall, and Mezzacappa (2012) and Cardall, Endeve, and Mezzacappa (2013) are defined with a factor ϵ^{-2} (ϵ^{-1}) compared to ours.

$\mathcal{J}$	zeroth moment of distribution function in comoving-frame	equation (2.19)
$\mathcal{H}^i$	first moment of distribution function in comoving-frame	equation (2.19)
$\mathcal{K}^{ij}$	second moment of distribution function in comoving-frame	equation (2.19)
$\mathcal{L}^{ijk}$	third moment of distribution function in comoving-frame	equation (2.19)
ε	zeroth moment of distribution function in lab-frame	equation (2.22)
F^i	first moment of distribution function in lab-frame	equation (2.22)
S^{ij}	second moment of distribution function in lab-frame	equation (2.22)
G	zeroth projection of U^{abc} measured in lab-frame	equation (125) of Cardall, Endeve, and Mezzacappa (2013)
I^i	first projection of U^{abc} measured in lab-frame	equation (126) of Cardall, Endeve, and Mezzacappa (2013)
P^{ij}	second projection of U^{abc} measured in lab-frame	equation (127) of Cardall, Endeve, and Mezzacappa (2013)
Q^{ijk}	third projection of U^{abc} measured in lab-frame	equation (128) of Cardall, Endeve, and Mezzacappa (2013)

eq. (A.3) by $\epsilon^2\sqrt{\gamma}$ and introduce the notation $\hat{X} \equiv \sqrt{\gamma}X$ for any quantity X to obtain:

$$\frac{1}{\alpha}\frac{\partial}{\partial t}(\hat{\mathcal{E}}) + \frac{1}{\alpha}\frac{\partial}{\partial x^j}(\alpha\hat{\mathcal{F}}^j - \beta^j\hat{\mathcal{E}}) + \hat{\mathcal{F}}^j\frac{\partial\ln\alpha}{\partial x^j} - \hat{\mathcal{S}}^{jk}K_{jk} - \frac{\partial}{\partial\epsilon}(\epsilon\hat{F}^\epsilon)$$
$$= -n_\mu\sqrt{\gamma}\epsilon\int p^\mu C d\Omega\,, \tag{A.5}$$

where the formal definition of F^ϵ is still given by eq. (A.4). Multiplying eq. (A.5) by W and using the product rule (i.e. $W\frac{\partial f}{\partial x} = \frac{\partial(Wf)}{\partial x} - f\frac{\partial W}{\partial x}$) one finds

$$\frac{1}{\alpha}\frac{\partial}{\partial t}(W\hat{\mathcal{E}}) + \frac{1}{\alpha}\frac{\partial}{\partial x^j}\{W(\alpha\hat{\mathcal{F}}^j - \beta^j\hat{\mathcal{E}})\} + W\hat{\mathcal{F}}^j\frac{\partial\ln\alpha}{\partial x^j} - W\hat{\mathcal{S}}^{jk}K_{jk} - \frac{\partial}{\partial\epsilon}(W\epsilon\hat{F}^\epsilon)$$
$$- \frac{1}{\alpha}\hat{\mathcal{E}}\frac{\partial W}{\partial t} - \frac{1}{\alpha}(\alpha\hat{\mathcal{F}}^j - \beta^j\hat{\mathcal{E}})\frac{\partial W}{\partial x^j} = -n_\mu W\sqrt{\gamma}\epsilon\int p^\mu C d\Omega\,. \tag{A.6}$$

We now extract the lab-frame energy-momentum equation from eqs. (172), (95-97), (149), (150), and (174) of Cardall, Endeve, and Mezzacappa (2013), again keeping their notation first:

$$\frac{1}{\sqrt{-g}}\frac{\partial}{\partial t}(\sqrt{\gamma}\mathcal{F}_i) + \frac{1}{\sqrt{-g}}\frac{\partial}{\partial x^j}\{\sqrt{\gamma}(\alpha\mathcal{S}^j{}_i - \beta^j\mathcal{F}_i)\} + \mathcal{E}\frac{\partial\ln\alpha}{\partial x^i} - \mathcal{F}_j\frac{1}{\alpha}\frac{\partial\beta^j}{\partial x^i}$$
$$- \frac{1}{2}\mathcal{S}^{jk}\frac{\partial\gamma_{jk}}{\partial x^i} - \frac{1}{\epsilon^2}\frac{\partial}{\partial\epsilon}(\epsilon^2 S_i^\epsilon) = \gamma_{i\mu}\frac{1}{\epsilon}\int p^\mu C d\Omega\,, \tag{A.7}$$

where

$$S_i^\epsilon \equiv W\{P_{ij}\frac{\partial v^j}{\partial\tau} + Q_{ij}{}^k\frac{\partial v^j}{\partial x^k} + \frac{1}{2}Q_i{}^{jk}v_l\frac{\partial\gamma_{jk}}{\partial x^l} + (P_i{}^j - I_iv^j)\frac{\partial\ln\alpha}{\partial x^j} - Q_i{}^{jk}K_{jk} + v^jP_{ik}\frac{1}{\alpha}\frac{\partial\beta^k}{\partial x^j}\}$$
$$+ (P_{ik}v^k - I_i)\frac{\partial W}{\partial\tau} + (Q_{ik}{}^jv^k - P_i{}^j)\frac{\partial W}{\partial x^j}\,. \tag{A.8}$$

Switching to our notation by doing the same replacements as for the energy equation above, we obtain:

$$\frac{1}{\alpha}\frac{\partial}{\partial t}(\hat{\mathcal{F}}_i) + \frac{1}{\alpha}\frac{\partial}{\partial x^j}\{(\alpha\hat{\mathcal{S}}^j_i - \beta^j\hat{\mathcal{F}}_i)\} + \hat{\mathcal{E}}\frac{\partial\ln\alpha}{\partial x^i} - \hat{\mathcal{F}}_j\frac{1}{\alpha}\frac{\partial\beta^j}{\partial x^i} - \frac{1}{2}\hat{\mathcal{S}}^{jk}\frac{\partial\gamma_{jk}}{\partial x^i} - \frac{\partial}{\partial\epsilon}(\epsilon\hat{S}_i^\epsilon)$$
$$= \gamma_{i\mu}\sqrt{\gamma}\epsilon\int p^\mu C d\Omega\,, \tag{A.9}$$

where the formal definition of S_i^ϵ is still given by eq. (A.8). We multiply eq. (A.9) by W and contract with v^i, to end up with

$$\frac{1}{\alpha}\frac{\partial}{\partial t}(Wv^i\hat{\mathcal{F}}_i) + \frac{1}{\alpha}\frac{\partial}{\partial x^j}\{Wv^i(\alpha\hat{\mathcal{S}}^j_i - \beta^j\hat{\mathcal{F}}_i)\} + Wv^i\hat{\mathcal{E}}\frac{\partial\ln\alpha}{\partial x^i} - Wv^i\hat{\mathcal{F}}_j\frac{1}{\alpha}\frac{\partial\beta^j}{\partial x^i}$$
$$- W\frac{1}{2}\hat{\mathcal{S}}^{jk}v^i\frac{\partial\gamma_{jk}}{\partial x^i} - W\frac{\partial}{\partial\epsilon}(v^i\epsilon\hat{S}_i^\epsilon) - v^i\hat{\mathcal{F}}_i\frac{1}{\alpha}\frac{\partial W}{\partial t} - v^i(\alpha\hat{\mathcal{S}}^j_i - \beta^j\hat{\mathcal{F}}_i)\frac{1}{\alpha}\frac{\partial W}{\partial x^j}$$
$$- W\hat{\mathcal{F}}_i\frac{1}{\alpha}\frac{\partial v^i}{\partial t} - W(\alpha\hat{\mathcal{S}}^j_i - \beta^j\hat{\mathcal{F}}_i)\frac{1}{\alpha}\frac{\partial v^i}{\partial x^j} = \gamma_{i\mu}v^iW\sqrt{\gamma}\epsilon\int p^\mu C d\Omega\,. \tag{A.10}$$

Subtracting eq. (A.10) from eq. (A.6) we get

$$
\frac{1}{\alpha}\frac{\partial}{\partial t}(W(\hat{\mathcal{E}}-v^i\hat{\mathcal{F}}_i)) + \frac{1}{\alpha}\frac{\partial}{\partial x^j}[W\{(\alpha\hat{\mathcal{F}}^j-\beta^j\hat{\mathcal{E}})-v^i(\alpha\hat{\mathcal{S}}_i^j-\beta^j\hat{\mathcal{F}}_i)\}]
$$

$$
+W(\hat{\mathcal{F}}^j-v^j\hat{\mathcal{E}})\frac{\partial\ln\alpha}{\partial x^j} + Wv^i\hat{\mathcal{F}}_j\frac{1}{\alpha}\frac{\partial\beta^j}{\partial x^i} - W\hat{\mathcal{S}}^{jk}(K_{jk}-\frac{1}{2}v^i\frac{\partial\gamma_{jk}}{\partial x^i}) - \frac{1}{\alpha}(\hat{\mathcal{E}}-v^i\hat{\mathcal{F}}_i)\frac{\partial W}{\partial t}
$$

$$
-\frac{1}{\alpha}\{(\alpha\hat{\mathcal{F}}^j-\beta^j\hat{\mathcal{E}})-v^i(\alpha\hat{\mathcal{S}}_i^j-\beta^j\hat{\mathcal{F}}_i)\}\frac{\partial W}{\partial x^j} + W\hat{\mathcal{F}}_i\frac{1}{\alpha}\frac{\partial v^i}{\partial t} + W(\alpha\hat{\mathcal{S}}_i^j-\beta^j\hat{\mathcal{F}}_i)\frac{1}{\alpha}\frac{\partial v^i}{\partial x^j}
$$

$$
-\frac{\partial}{\partial\epsilon}\{W\epsilon(\hat{F}^\epsilon-v^i\hat{S}_i^\epsilon)\} = -W\sqrt{\gamma}\epsilon(n_\mu+\gamma_{i\mu}v^i)\int p^\mu C d\Omega . \tag{A.11}
$$

We further rewrite $n^\mu\frac{\partial}{\partial x^\mu} = \frac{\partial}{\partial\tau}$ with $n^\mu = (1/\alpha, -\beta^i/\alpha)$, $W(n_\mu+\gamma_{i\mu}v^i) = u_\mu$, $-u_\mu p^\mu = \epsilon$, and redefine $\epsilon^2 C \to C$:

$$
\frac{1}{\alpha}\frac{\partial}{\partial t}(W(\hat{\mathcal{E}}-v^i\hat{\mathcal{F}}_i)) + \frac{1}{\alpha}\frac{\partial}{\partial x^j}[W\{\alpha(\hat{\mathcal{F}}^j-v^i\hat{\mathcal{S}}_i^j)-\beta^j(\hat{\mathcal{E}}-v^i\hat{\mathcal{F}}_i)\}]
$$

$$
+W(\hat{\mathcal{F}}^j-v^j\hat{\mathcal{E}})\frac{1}{\alpha}\frac{\partial\alpha}{\partial x^j} + Wv^i\hat{\mathcal{F}}_j\frac{1}{\alpha}\frac{\partial\beta^j}{\partial x^i} - W\hat{\mathcal{S}}^{jk}(K_{jk}-\frac{1}{2}v^i\frac{\partial\gamma_{jk}}{\partial x^i})
$$

$$
-(\hat{\mathcal{E}}-v^i\hat{\mathcal{F}}_i)\frac{\partial W}{\partial\tau} - (\hat{\mathcal{F}}^j-v^i\hat{\mathcal{S}}_i^j)\frac{\partial W}{\partial x^j} + W\hat{\mathcal{F}}_i\frac{\partial v^i}{\partial\tau} + W\hat{\mathcal{S}}_i^j\frac{\partial v^i}{\partial x^j}
$$

$$
-\frac{\partial}{\partial\epsilon}\{W\epsilon(\hat{F}^\epsilon-v^i\hat{S}_i^\epsilon)\} = \sqrt{\gamma}\int C d\Omega . \tag{A.12}
$$

The term inside the energy derivative of eq. (A.12) is given by:

$$
\begin{aligned}
\epsilon W(F^\epsilon-v^iS_i^\epsilon) =& \ \epsilon W[W\{I_j\frac{\partial v^j}{\partial\tau} + P_j^k\frac{\partial v^j}{\partial x^k} + \frac{1}{2}P^{jk}v^l\frac{\partial\gamma_{jk}}{\partial x^l} + (I^j-Gv^j)\frac{\partial\ln\alpha}{\partial x^j} \\
&-P^{jk}K_{jk} + v^jI_k\frac{1}{\alpha}\frac{\partial\beta^k}{\partial x^j}\} + (I_jv^j-G)\frac{\partial W}{\partial\tau} + (P_k^jv^k-I^j)\frac{\partial W}{\partial x^j} \\
&-v^iW\{P_{ij}\frac{\partial v^j}{\partial\tau} + Q_{ij}^k\frac{\partial v^j}{\partial x^k} + \frac{1}{2}Q_i^{jk}v^l\frac{\partial\gamma_{jk}}{\partial x^l} + (P_i^j-I_iv^j)\frac{\partial\ln\alpha}{\partial x^j} \\
&-Q_i^{jk}K_{jk} + v^jP_{ik}\frac{1}{\alpha}\frac{\partial\beta^k}{\partial x^j}\} - v^i(P_{ik}v^k-I_i)\frac{\partial W}{\partial\tau} - v^i(Q_{ik}^jv^k-P_i^j)\frac{\partial W}{\partial x^j}] \\
=& \ \epsilon\Bigg\{W^2[(I_j-v^iP_{ij})\frac{\partial v^j}{\partial\tau} + (P_j^k-v^iQ_{ij}^k)\frac{\partial v^j}{\partial x^k} \\
&+\{(I^j-Gv^j)-v^i(P_i^j-I_iv^j)\}\frac{\partial\ln\alpha}{\partial x^j} + v^j(I_k-v^iP_{ik})\frac{1}{\alpha}\frac{\partial\beta^k}{\partial x^j} \\
&+(P^{jk}-v^iQ_i^{jk})(\frac{1}{2}v^l\frac{\partial\gamma_{jk}}{\partial x^l}-K_{jk})] \\
&+W\{(I_jv^j-G)-v^i(P_{ik}v^k-I_i)\}\frac{\partial W}{\partial\tau} \\
&+W\{(P_k^jv^k-I^j)-v^i(Q_{ik}^jv^k-P_i^j)\}\frac{\partial W}{\partial x^j}\Bigg\} . \tag{A.13}
\end{aligned}
$$

In order to express $\{G, I^i, P^{ij}, Q^{ijk}\}$ in terms of the lab-frame moments, $\{E, F^i, S^{ij}\}$, we use eqs. (74)-(80) of Endeve, Cardall, and Mezzacappa (2012), however with ϵ set

to 1 in their equations to account for the different definitions:

$$
\begin{aligned}
\epsilon W(F^\epsilon - v^i S_i^\epsilon) &= \epsilon \Bigg\{ W \Big[\mathcal{F}_j \frac{\partial v^j}{\partial \tau} + \mathcal{S}_j^{\ k} \frac{\partial v^j}{\partial x^k} + (\mathcal{F}^j - \mathcal{E} v^j) \frac{\partial \ln \alpha}{\partial x^j} \\
&\qquad + v^j \mathcal{F}_k \frac{1}{\alpha} \frac{\partial \beta^k}{\partial x^j} + \mathcal{S}^{jk} (\frac{1}{2} v^l \frac{\partial \gamma_{jk}}{\partial x^l} - K_{jk}) \Big] \\
&\qquad - (\mathcal{E} - v^i \mathcal{F}_i) \frac{\partial W}{\partial \tau} - (\mathcal{F}^j - \mathcal{S}_k^{\ j} v^k) \frac{\partial W}{\partial x^j} \Bigg\} . \\
&\equiv \epsilon R_\epsilon ,
\end{aligned}
\tag{A.14}
$$

where in the last line we defined R_ϵ used in the main text of this paper. While R_ϵ is expressed in eq. (A.14) in terms of the lab-frame moments, it can be re-expressed in terms of the comoving-frame moments using

$$
\begin{aligned}
\mathcal{E} - v^i \mathcal{F}_i &= \mathcal{J} + \bar{v}_{\hat{i}} \mathcal{H}^{\hat{i}}, \\
\mathcal{F}^i - \mathcal{S}_j^{\ i} v^j &= \frac{1}{W} e^i_{\hat{i}} \mathcal{H}^{\hat{i}} + v^i \mathcal{J} + W v^i \bar{v}_{\hat{i}} \mathcal{H}^{\hat{i}}, \\
\mathcal{F}^i - \mathcal{E} v^i &= W \Big(e^i_{\hat{i}} - \frac{W}{W+1} v^i \hat{v}_{\hat{i}} \Big) \Big(\mathcal{H}^{\hat{i}} + \hat{v}_{\hat{j}} \mathcal{K}^{\hat{i}\hat{j}} \Big)
\end{aligned}
\tag{A.15}
$$

as well as eqs. (2.22). Using the same transformations also for the remaining terms of eq. (A.12), we finally obtain the neutrino energy equation in terms of the comoving-frame neutrino moments as:

$$
\begin{aligned}
&\frac{1}{\alpha} \frac{\partial}{\partial t} [W(\hat{\mathcal{J}} + \bar{v}_{\hat{i}} \hat{\mathcal{H}}^{\hat{i}})] + \frac{1}{\alpha} \frac{\partial}{\partial x^j} [\alpha W (v^j - \beta^j/\alpha) \hat{\mathcal{J}}] \\
&+ \frac{1}{\alpha} \frac{\partial}{\partial x^j} [\alpha e^j_{\hat{i}} \hat{\mathcal{H}}^{\hat{i}}] + \frac{1}{\alpha} \frac{\partial}{\partial x^j} \Big[\alpha W \Big(\frac{W}{W+1} v^j - \beta^j/\alpha \Big) \bar{v}_{\hat{i}} \hat{\mathcal{H}}^{\hat{i}} \Big] + \\
&\hat{R}_\epsilon - \frac{\partial}{\partial \epsilon} (\epsilon \hat{R}_\epsilon) = \sqrt{\gamma} \int C d\Omega .
\end{aligned}
\tag{A.16}
$$

Appendix B

Derivation of FLD flux and transport equation

In this section, we show the derivation of the diffusive flux in the flat space-time given by the spatial metric, $\gamma^i_j = \delta^i_j$. The flat metric tetrad for spherical polar coordinate is given by $e^{k\hat{i}} = \mathrm{diag}(1, 1/r, 1/(r\sin\theta))$. We start with equation (A.9). We neglect the time and energy derivative terms. We also drop all the terms with velocity. Under these approximation equation (A.9) simplifies to,

$$\frac{\partial}{\partial x^j}(\hat{S}^j_i) - \frac{1}{2}\hat{S}^{jk}\frac{\partial\gamma_{jk}}{\partial x^i} = \gamma_{i\mu}\sqrt{\gamma}\epsilon\int p^\mu C d\Omega,$$

(B.1)

where

$$S^{ij} \equiv e^i_{\hat{i}}e^j_{\hat{j}}\mathcal{K}^{\hat{i}\hat{j}},$$

(B.2)

In the diffusion limit,

$$\mathcal{K}^{\hat{i}\hat{j}} = \frac{1}{3}\delta^{\hat{i}\hat{j}}\mathcal{J}.$$

(B.3)

For the elastic scattering the right hand side of equation (B.1) can be written as,

$$\epsilon\int p^\mu C d\Omega$$
$$= \epsilon^2\int l^\mu C d\Omega$$
$$= -\kappa_t\mathcal{H}^i.$$

(B.4)

Using equations (B.3) and (B.4) in the equation (B.1) one finds,

$$\frac{\partial}{\partial x^j}(\gamma^j_{\ i}\sqrt{\gamma}\mathcal{J}) - \frac{1}{2}\sqrt{\gamma}\gamma^{jk}\frac{\partial\gamma_{jk}}{\partial x^i}\mathcal{J} = -\sqrt{\gamma}3\kappa_t\mathcal{H}^i,$$
$$\frac{\partial}{\partial x^i}(\sqrt{\gamma}\mathcal{J}) - \frac{1}{2}\sqrt{\gamma}\gamma^{jk}\frac{\partial\gamma_{jk}}{\partial x^i}\mathcal{J} = -\sqrt{\gamma}3\kappa_t\mathcal{H}^i.$$

(B.5)

Using the Identity $\partial_i(\sqrt{\gamma}) = 1/2\sqrt{\gamma}\gamma^{jk}\partial_i\gamma_{jk}$ we get,

$$\frac{\partial}{\partial x^i}(\mathcal{J}) = -3\kappa_t\mathcal{H}^i,$$

$$\mathcal{H}^i = -\frac{1}{3\kappa_t}\frac{\partial}{\partial x^i}(\mathcal{J}),$$

$$\mathcal{H}^{\hat{i}} = -\frac{e^{i\hat{i}}}{3\kappa_t}\frac{\partial}{\partial x^i}(\mathcal{J}).$$

Now, introducing the flux-limiter λ and diffusion coefficient $D = \lambda/(3\kappa_t)$ we obtain the FLD flux,

$$\mathcal{H}^{\hat{i}} = -\frac{\lambda e^{i\hat{i}}}{3\kappa_t}\frac{\partial}{\partial x^i}(\mathcal{J}).$$

$$\mathcal{H}^{\hat{i}} = -De^{i\hat{i}}\frac{\partial}{\partial x^i}(\mathcal{J}).$$

$$(B.6)$$

Using the FLD flux in the equation (A.16) we obtain the FLD transport equation

$$\frac{1}{\alpha}\frac{\partial}{\partial t}[W(\hat{\mathcal{J}} + \bar{v}_{\hat{i}}\hat{\mathcal{H}}^{\hat{i}})] + \frac{1}{\alpha}\frac{\partial}{\partial x^j}[\alpha W(v^j - \beta^j/\alpha)\hat{\mathcal{J}}] - \frac{1}{\alpha}\frac{\partial}{\partial x^j}[\alpha\gamma^{ij}D\partial_i\mathcal{J}]$$

$$-\frac{1}{\alpha}\frac{\partial}{\partial x^j}\left[\alpha W\left(\frac{W}{W+1}v^j - \beta^j/\alpha\right)v^iD\partial_i\mathcal{J}\right] + R_\epsilon - \frac{\partial}{\partial\epsilon}(\epsilon R_\epsilon)$$

$$= \kappa_a(\hat{\mathcal{J}}^{eq} - \hat{\mathcal{J}})$$

$$(B.7)$$

Bibliography

A. Dorfi, Ernst (1998). "Radiation Hydrodynamics: Numerical Aspects and Applications". In: *Computational Methods for Astrophysical Fluid Flow: Saas-Fee Advanced Course 27 Lecture Notes 1997 Swiss Society for Astrophysics and Astronomy*. Ed. by O. Steiner and A. Gautschy. Berlin, Heidelberg: Springer Berlin Heidelberg, pp. 263–341. ISBN: 978-3-540-31632-9. DOI: 10.1007/3-540-31632-9_3. URL: https://doi.org/10.1007/3-540-31632-9_3.

Abdikamalov, E. et al. (2012). "A New Monte Carlo Method for Time-dependent Neutrino Radiation Transport". In: 755, 111, p. 111. DOI: 10.1088/0004-637X/755/2/111. arXiv: 1203.2915 [astro-ph.SR].

Allen, J. S. (1970). "Numerical Solutions of the Compressible Navier-Stokes Equations for the Laminar Near Wake". In: *Physics of Fluids* 13.1, p. 37. DOI: 10.1063/1.1692801. URL: https://doi.org/10.1063/1.1692801.

Anderson, Dale (2011). *Computational Fluid Mechanics and Heat Transfer, Third Edition (Series in Computational and Physical Processes in Mechanics and Thermal Sciences)*. CRC Press. ISBN: 1591690374. URL: https://www.xarg.org/ref/a/1591690374/.

Anderson, E. et al. (1999). *LAPACK Users' Guide*. Third. Philadelphia, PA: Society for Industrial and Applied Mathematics. ISBN: 0-89871-447-8 (paperback).

Artemova, I. V., G. Bjoernsson, and I. D. Novikov (1996). "Modified Newtonian Potentials for the Description of Relativistic Effects in Accretion Disks around Black Holes". In: 461, p. 565. DOI: 10.1086/177084.

Baron, E. et al. (1989). "General relativistic neutrino transport in stellar collapse". In: 339, pp. 978–986. DOI: 10.1086/167352.

Baumgarte, T. W., P. J. Montero, and E. Müller (2015). "Numerical relativity in spherical polar coordinates: Off-center simulations". In: 91.6, 064035, p. 064035. DOI: 10.1103/PhysRevD.91.064035. arXiv: 1501.05259 [gr-qc].

Baumgarte, T. W. et al. (2013). "Numerical relativity in spherical polar coordinates: Evolution calculations with the BSSN formulation". In: 87.4, 044026, p. 044026. DOI: 10.1103/PhysRevD.87.044026. arXiv: 1211.6632 [gr-qc].

Baumgarte, Thomas W. and Stuart L. Shapiro (2010). *Numerical Relativity: Solving Einstein's Equations on the Computer*. New York, NY, USA: Cambridge University Press. ISBN: 052151407X, 9780521514071.

Blondin, J. M. and A. Mezzacappa (2007). "Pulsar spins from an instability in the accretion shock of supernovae". In: 445, pp. 58–60. DOI: 10.1038/nature05428. eprint: astro-ph/0611680.

Blondin, J. M., A. Mezzacappa, and C. DeMarino (2003). "Stability of Standing Accretion Shocks, with an Eye toward Core-Collapse Supernovae". In: 584, pp. 971–980. DOI: 10.1086/345812. eprint: astro-ph/0210634.

Bollig, R. et al. (2017). "Muon Creation in Supernova Matter Facilitates Neutrino-Driven Explosions". In: *Physical Review Letters* 119.24, 242702, p. 242702. DOI: 10.1103/PhysRevLett.119.242702. arXiv: 1706.04630 [astro-ph.HE].

Bowers, R. L. and J. R. Wilson (1982). "A numerical model for stellar core collapse calculations". In: 50, pp. 115–159. DOI: 10.1086/190822.

Bruenn, S. W. (1985). "Stellar core collapse - Numerical model and infall epoch". In: 58, pp. 771–841. DOI: 10.1086/191056.

Bruenn, S. W., K. R. De Nisco, and A. Mezzacappa (2001). "General Relativistic Effects in the Core Collapse Supernova Mechanism". In: 560, pp. 326–338. DOI: 10.1086/322319. eprint: astro-ph/0101400.

Bruenn, S. W. et al. (2013). "Axisymmetric Ab Initio Core-collapse Supernova Simulations of 12-25 M Stars". In: 767, L6, p. L6. DOI: 10.1088/2041-8205/767/1/L6. arXiv: 1212.1747 [astro-ph.SR].

Bruenn, S. W. et al. (2018). "Chimera: A massively parallel code for core-collapse supernova simulation". In: *ArXiv e-prints*. arXiv: 1809.05608 [astro-ph.IM].

Buras, R. et al. (2006). "Two-dimensional hydrodynamic core-collapse supernova simulations with spectral neutrino transport. I. Numerical method and results for a 15 M star". In: 447, pp. 1049–1092. DOI: 10.1051/0004-6361:20053783. eprint: astro-ph/0507135.

Burrows, A. (2013). "Colloquium: Perspectives on core-collapse supernova theory". In: *Reviews of Modern Physics* 85, pp. 245–261. DOI: 10.1103/RevModPhys.85.245. arXiv: 1210.4921 [astro-ph.SR].

Burrows, A. and J. M. Lattimer (1986). "The birth of neutron stars". In: 307, pp. 178–196. DOI: 10.1086/164405.

Burrows, A. et al. (2007). "Features of the Acoustic Mechanism of Core-Collapse Supernova Explosions". In: 655, pp. 416–433. DOI: 10.1086/509773. eprint: astro-ph/0610175.

Cardall, C. Y., E. Endeve, and A. Mezzacappa (2013). "Conservative 3+1 general relativistic variable Eddington tensor radiation transport equations". In: 87.10, 103004, p. 103004. DOI: 10.1103/PhysRevD.87.103004. arXiv: 1209.2151 [astro-ph.HE].

Cernohorsky, J. (1990). "Neutrino driven neutron star formation". PhD thesis. University of Amsterdam.

Cernohorsky, J., L. J. van den Horn, and J. Cooperstein (1989). "Maximum entropy Eddington factors in flux-limited neutrino diffusion." In: 42, pp. 603–613. DOI: 10.1016/0022-4073(89)90054-X.

Chan, C. et al. (2018). "Black Hole Formation and Fallback during the Supernova Explosion of a 40 M Star". In: 852, L19, p. L19. DOI: 10.3847/2041-8213/aaa28c. arXiv: 1710.00838 [astro-ph.SR].

Colella, P. and P. R. Woodward (1984). "The Piecewise Parabolic Method (PPM) for Gas-Dynamical Simulations". In: *Journal of Computational Physics* 54, pp. 174–201. DOI: 10.1016/0021-9991(84)90143-8.

Cooperstein, J. and E. Baron (1992). "Flux-limited diffusion in hydrodynamics". In: 398, pp. 531–543. DOI: 10.1086/171878.

Dgani, R. and H.-T. Janka (1992). "Artificial opacity - Numerical implementation into flux-limited neutrino diffusion". In: 256, pp. 428–432.

Endeve, E., C. Y. Cardall, and A. Mezzacappa (2012). "Conservative Moment Equations for Neutrino Radiation Transport with Limited Relativity". In: *ArXiv e-prints*. arXiv: 1212.4064 [astro-ph.SR].

Favata, M. (2010). "The gravitational-wave memory effect". In: *Classical and Quantum Gravity* 27.8, 084036, p. 084036. DOI: 10.1088/0264-9381/27/8/084036. arXiv: 1003.3486 [gr-qc].

Fernández, R. (2015). "Three-dimensional simulations of SASI- and convection-dominated core-collapse supernovae". In: 452, pp. 2071–2086. DOI: 10.1093/mnras/stv1463. arXiv: 1504.07996 [astro-ph.HE].

Fernández, R. et al. (2014). "Characterizing SASI- and convection-dominated core-collapse supernova explosions in two dimensions". In: 440, pp. 2763–2780. DOI: 10.1093/mnras/stu408. arXiv: 1310.0469 [astro-ph.SR].

Foglizzo, T., L. Scheck, and H.-T. Janka (2006). "Neutrino-driven Convection versus Advection in Core-Collapse Supernovae". In: 652, pp. 1436–1450. DOI: 10.1086/508443. eprint: astro-ph/0507636.

Foglizzo, T. et al. (2007). "Instability of a Stalled Accretion Shock: Evidence for the Advective-Acoustic Cycle". In: 654, pp. 1006–1021. DOI: 10.1086/509612. eprint: astro-ph/0606640.

Font, J. A. (2008). "Numerical Hydrodynamics and Magnetohydrodynamics in General Relativity". In: *Living Reviews in Relativity* 11, 7, p. 7. DOI: 10.12942/lrr-2008-7.

Foucart, F. (2018). "Monte Carlo closure for moment-based transport schemes in general relativistic radiation hydrodynamic simulations". In: 475, pp. 4186–4207. DOI: 10.1093/mnras/sty108. arXiv: 1708.08452 [astro-ph.HE].

Hanke, F. et al. (2013). "SASI Activity in Three-dimensional Neutrino-hydrodynamics Simulations of Supernova Cores". In: 770, 66, p. 66. DOI: 10.1088/0004-637X/770/1/66. arXiv: 1303.6269 [astro-ph.SR].

Harten, Amiram, Peter D. Lax, and Bram van Leer (1983). "On Upstream Differencing and Godunov-Type Schemes for Hyperbolic Conservation Laws". In: *SIAM Review* 25.1, pp. 35–61. DOI: 10.1137/1025002. URL: https://doi.org/10.1137/1025002.

Heger, A., N. Langer, and S. E. Woosley (2000). "Presupernova Evolution of Rotating Massive Stars. I. Numerical Method and Evolution of the Internal Stellar Structure". In: 528, pp. 368–396. DOI: 10.1086/308158. eprint: astro-ph/9904132.

Heger, A. and S. E. Woosley (2010). "Nucleosynthesis and Evolution of Massive Metal-free Stars". In: 724, pp. 341–373. DOI: 10.1088/0004-637X/724/1/341. arXiv: 0803.3161.

Heger, A., S. E. Woosley, and H. C. Spruit (2005). "Presupernova Evolution of Differentially Rotating Massive Stars Including Magnetic Fields". In: 626, pp. 350–363. DOI: 10.1086/429868. eprint: astro-ph/0409422.

Hempel, M. et al. (2012). "New Equations of State in Simulations of Core-collapse Supernovae". In: 748, 70, p. 70. DOI: 10.1088/0004-637X/748/1/70. arXiv: 1108.0848 [astro-ph.HE].

Herant, M. et al. (1994). "Inside the supernova: A powerful convective engine". In: 435, pp. 339–361. DOI: 10.1086/174817. eprint: astro-ph/9404024.

Horowitz, C. J. (2002). "Weak magnetism for antineutrinos in supernovae". In: 65.4, 043001, p. 043001. DOI: 10.1103/PhysRevD.65.043001. eprint: astro-ph/0109209.

Janka, H.-T. (1992). "Flux-limited neutrino diffusion versus Monte Carlo neutrino transport". In: 256, pp. 452–458.

— (2012). "Explosion Mechanisms of Core-Collapse Supernovae". In: *Annual Review of Nuclear and Particle Science* 62, pp. 407–451. DOI: 10.1146/annurev-nucl-102711-094901. arXiv: 1206.2503 [astro-ph.SR].

— (2017a). "Neutrino-Driven Explosions". In: *Handbook of Supernovae, ISBN 978-3-319-21845-8. Springer International Publishing AG, 2017, p. 1095.* Ed. by A. W. Alsabti and P. Murdin, p. 1095. DOI: 10.1007/978-3-319-21846-5_109.

— (2017b). "Neutrino Emission from Supernovae". In: *Handbook of Supernovae, ISBN 978-3-319-21845-8. Springer International Publishing AG, 2017, p. 1575.* Ed. by A. W. Alsabti and P. Murdin, p. 1575. DOI: 10.1007/978-3-319-21846-5_4.

Janka, H.-T. and W. Hillebrandt (1989). "Monte Carlo simulations of neutrino transport in type II supernovae". In: 78, pp. 375–397.

Janka, H.-T. and E. Mueller (1996). "Neutrino heating, convection, and the mechanism of Type-II supernova explosions." In: 306, p. 167.

Janka, H.-T. et al. (2007). "Theory of core-collapse supernovae". In: 442, pp. 38–74. DOI: 10.1016/j.physrep.2007.02.002. eprint: astro-ph/0612072.

Just, O., M. Obergaulinger, and H.-T. Janka (2015). "A new multidimensional, energy-dependent two-moment transport code for neutrino-hydrodynamics". In: 453, pp. 3386–3413. DOI: 10.1093/mnras/stv1892. arXiv: 1501.02999 [astro-ph.HE].

Just, O. et al. (2018). "Core-collapse supernova simulations in one and two dimensions: comparison of codes and approximations". In: 481, pp. 4786–4814. DOI: 10.1093/mnras/sty2578. arXiv: 1805.03953 [astro-ph.HE].

Kuroda, T., T. Takiwaki, and K. Kotake (2016). "A New Multi-energy Neutrino Radiation-Hydrodynamics Code in Full General Relativity and Its Application to the Gravitational Collapse of Massive Stars". In: 222, 20, p. 20. DOI: 10.3847/0067-0049/222/2/20. arXiv: 1501.06330 [astro-ph.HE].

Kuroda, T. et al. (2018). "A full general relativistic neutrino radiation-hydrodynamics simulation of a collapsing very massive star and the formation of a black hole". In: 477, pp. L80–L84. DOI: 10.1093/mnrasl/sly059. arXiv: 1801.01293 [astro-ph.HE].

Lentz, E. J. et al. (2015). "Three-dimensional Core-collapse Supernova Simulated Using a 15 M Progenitor". In: 807, L31, p. L31. DOI: 10.1088/2041-8205/807/2/L31. arXiv: 1505.05110 [astro-ph.SR].

Levermore, C. D. and G. C. Pomraning (1981). "A flux-limited diffusion theory". In: 248, pp. 321–334. DOI: 10.1086/159157.

Liebendörfer, M. et al. (2004). "A Finite Difference Representation of Neutrino Radiation Hydrodynamics in Spherically Symmetric General Relativistic Spacetime". In: 150, pp. 263–316. DOI: 10.1086/380191. eprint: astro-ph/0207036.

Lindquist, R. W. (1966). "Relativistic transport theory". In: *Annals of Physics* 37, pp. 487–518. DOI: 10.1016/0003-4916(66)90207-7.

Liu, X.-D. and S. Osher (1998). "Convex ENO High Order Multi-dimensional Schemes without Field by Field Decomposition or Staggered Grids". In: *Journal of Computational Physics* 142, pp. 304–330. DOI: 10.1006/jcph.1998.5937.

Livne, E. et al. (2004). "Two-dimensional, Time-dependent, Multigroup, Multiangle Radiation Hydrodynamics Test Simulation in the Core-Collapse Supernova Context". In: 609, pp. 277–287. DOI: 10.1086/421012. eprint: astro-ph/0312633.

MacFadyen, A. I. and S. E. Woosley (1999). "Collapsars: Gamma-Ray Bursts and Explosions in "Failed Supernovae"". In: 524, pp. 262–289. DOI: 10.1086/307790. eprint: astro-ph/9810274.

Marek, A. et al. (2006). "Exploring the relativistic regime with Newtonian hydrodynamics: an improved effective gravitational potential for supernova simulations". In: 445, pp. 273–289. DOI: 10.1051/0004-6361:20052840. eprint: astro-ph/0502161.

Melson, T., H.-T. Janka, and A. Marek (2015). "Neutrino-driven Supernova of a Low-mass Iron-core Progenitor Boosted by Three-dimensional Turbulent Convection". In: 801, L24, p. L24. DOI: 10.1088/2041-8205/801/2/L24. arXiv: 1501.01961 [astro-ph.SR].

Melson, T. et al. (2015). "Neutrino-driven Explosion of a 20 Solar-mass Star in Three Dimensions Enabled by Strange-quark Contributions to Neutrino-Nucleon Scattering". In: 808, L42, p. L42. DOI: 10.1088/2041-8205/808/2/L42. arXiv: 1504.07631 [astro-ph.SR].

Mihalas, D. (1980). "Solution of the comoving-frame equation of transfer in spherically symmetric flows. VI - Relativistic flows". In: 237, pp. 574–589. DOI: 10.1086/157902.

Montero, P. J., T. W. Baumgarte, and E. Müller (2014). "General relativistic hydrodynamics in curvilinear coordinates". In: 89.8, 084043, p. 084043. DOI: 10.1103/PhysRevD.89.084043. arXiv: 1309.7808 [gr-qc].

Montero, P. J. and I. Cordero-Carrión (2012). "BSSN equations in spherical coordinates without regularization: Vacuum and nonvacuum spherically symmetric spacetimes". In: 85.12, 124037, p. 124037. DOI: 10.1103/PhysRevD.85.124037. arXiv: 1204.5377 [gr-qc].

Müller, B. (2015). "The dynamics of neutrino-driven supernova explosions after shock revival in 2D and 3D". In: 453, pp. 287–310. DOI: 10.1093/mnras/stv1611. arXiv: 1506.05139 [astro-ph.SR].

Müller, B. and H.-T. Janka (2014). "A New Multi-dimensional General Relativistic Neutrino Hydrodynamics Code for Core-collapse Supernovae. IV. The Neutrino Signal". In: 788, 82, p. 82. DOI: 10.1088/0004-637X/788/1/82. arXiv: 1402.3415 [astro-ph.SR].

Müller, B., H.-T. Janka, and H. Dimmelmeier (2010). "A New Multi-dimensional General Relativistic Neutrino Hydrodynamic Code for Core-collapse Supernovae. I. Method and Code Tests in Spherical Symmetry". In: 189, pp. 104–133. DOI: 10.1088/0067-0049/189/1/104. arXiv: 1001.4841 [astro-ph.SR].

Müller, B., H.-T. Janka, and A. Marek (2012). "A New Multi-dimensional General Relativistic Neutrino Hydrodynamics Code for Core-collapse Supernovae. II. Relativistic Explosion Models of Core-collapse Supernovae". In: 756, 84, p. 84. DOI: 10.1088/0004-637X/756/1/84. arXiv: 1202.0815 [astro-ph.SR].

Murphy, J. W., J. C. Dolence, and A. Burrows (2013). "The Dominance of Neutrino-driven Convection in Core-collapse Supernovae". In: 771, 52, p. 52. DOI: 10.1088/0004-637X/771/1/52. arXiv: 1205.3491 [astro-ph.SR].

Murphy, J. W., C. D. Ott, and A. Burrows (2009). "A Model for Gravitational Wave Emission from Neutrino-Driven Core-Collapse Supernovae". In: 707, pp. 1173–1190. DOI: 10.1088/0004-637X/707/2/1173. arXiv: 0907.4762 [astro-ph.SR].

Myra, E. S. et al. (1987). "The effect of neutrino transport on the collapse of iron stellar cores". In: 318, pp. 744–759. DOI: 10.1086/165408.

Obergaulinger, M., M. A. Aloy, and E. Müller (2006). "Axisymmetric simulations of magneto-rotational core collapse: dynamics and gravitational wave signal". In: 450, pp. 1107–1134. DOI: 10.1051/0004-6361:20054306. eprint: astro-ph/0510184.

O'Connor, E. (2015). "An Open-source Neutrino Radiation Hydrodynamics Code for Core-collapse Supernovae". In: 219, 24, p. 24. DOI: 10.1088/0067-0049/219/2/24. arXiv: 1411.7058 [astro-ph.HE].

O'Connor, E. and C. D. Ott (2011). "Black Hole Formation in Failing Core-Collapse Supernovae". In: 730, 70, p. 70. DOI: 10.1088/0004-637X/730/2/70. arXiv: 1010.5550 [astro-ph.HE].

O'Connor, E. P. and S. M. Couch (2018). "Two-dimensional Core-collapse Supernova Explosions Aided by General Relativity with Multidimensional Neutrino Transport". In: 854, p. 63.

OConnor, E. P. and S. M. Couch (2018). "Exploring Fundamentally Three-dimensional Phenomena in High-fidelity Simulations of Core-collapse Supernovae". In: 865, 81, p. 81. DOI: 10.3847/1538-4357/aadcf7. arXiv: 1807.07579 [astro-ph.HE].

Pomraning, G. C. (1981). "Maximum entropy Eddington factors and flux limited diffusion theory." In: 26, pp. 385–388. DOI: 10.1016/0022-4073(81)90101-1.

Rampp, M. and H.-T. Janka (2002). "Radiation hydrodynamics with neutrinos. Variable Eddington factor method for core-collapse supernova simulations". In: 396, pp. 361–392. DOI: 10.1051/0004-6361:20021398. eprint: astro-ph/0203101.

Richers, S. et al. (2015). "Monte Carlo Neutrino Transport through Remnant Disks from Neutron Star Mergers". In: 813, 38, p. 38. DOI: 10.1088/0004-637X/813/1/38. arXiv: 1507.03606 [astro-ph.HE].

Roberts, L. F. et al. (2016). "General-Relativistic Three-Dimensional Multi-group Neutrino Radiation-Hydrodynamics Simulations of Core-Collapse Supernovae". In: 831, 98, p. 98. DOI: 10.3847/0004-637X/831/1/98. arXiv: 1604.07848 [astro-ph.HE].

Sekiguchi, Y. et al. (2016). "Dynamical mass ejection from the merger of asymmetric binary neutron stars: Radiation-hydrodynamics study in general relativity". In: 93.12, p. 124046.

Shibata, M. et al. (2011). "Truncated Moment Formalism for Radiation Hydrodynamics in Numerical Relativity". In: *Progress of Theoretical Physics* 125, pp. 1255–1287. DOI: 10.1143/PTP.125.1255. arXiv: 1104.3937 [astro-ph.HE].

Smith, N. (2013). "A model for the 19th century eruption of Eta Carinae: CSM interaction like a scaled-down Type IIn Supernova". In: 429, pp. 2366–2379. DOI: 10.1093/mnras/sts508. arXiv: 1209.6155 [astro-ph.SR].

Steiner, A. W., M. Hempel, and T. Fischer (2013). "Core-collapse Supernova Equations of State Based on Neutron Star Observations". In: 774, 17, p. 17. DOI: 10.1088/0004-637X/774/1/17. arXiv: 1207.2184 [astro-ph.SR].

Sukhbold, T. et al. (2016). "Core-collapse Supernovae from 9 to 120 Solar Masses Based on Neutrino-powered Explosions". In: 821, 38, p. 38. DOI: 10.3847/0004-637X/821/1/38. arXiv: 1510.04643 [astro-ph.HE].

Sumiyoshi, K. and S. Yamada (2012). "Neutrino Transfer in Three Dimensions for Core-collapse Supernovae. I. Static Configurations". In: 199, 17, p. 17. DOI: 10.1088/0067-0049/199/1/17. arXiv: 1201.2244 [astro-ph.HE].

Summa, A. et al. (2018). "Rotation-supported Neutrino-driven Supernova Explosions in Three Dimensions and the Critical Luminosity Condition". In: 852, 28, p. 28. DOI: 10.3847/1538-4357/aa9ce8. arXiv: 1708.04154 [astro-ph.HE].

Suresh, A. and H. T. Huynh (1997). "Accurate Monotonicity-Preserving Schemes with Runge Kutta Time Stepping". In: *Journal of Computational Physics* 136, pp. 83–99. DOI: 10.1006/jcph.1997.5745.

Swesty, F. D. and E. S. Myra (2009). "A Numerical Algorithm for Modeling Multigroup Neutrino-Radiation Hydrodynamics in Two Spatial Dimensions". In: 181, pp. 1–52. DOI: 10.1088/0067-0049/181/1/1.

Takahashi, K., H. Umeda, and T. Yoshida (2014). "Stellar Yields of Rotating First Stars. I. Yields of Weak Supernovae and Abundances of Carbon-enhanced Hypermetal-poor Stars". In: 794, 40, p. 40. DOI: 10.1088/0004-637X/794/1/40. arXiv: 1406.5305 [astro-ph.SR].

Thorne, K. S. (1981). "Relativistic radiative transfer - Moment formalisms". In: 194, pp. 439–473. DOI: 10.1093/mnras/194.2.439.

Toro, Eleuterio F. (2009). *Riemann Solvers and Numerical Methods for Fluid Dynamics*. Springer Berlin Heidelberg. DOI: 10.1007/b79761. URL: https://doi.org/10.1007/b79761.

Vink, J. S., ed. (2015). *Very Massive Stars in the Local Universe*. Vol. 412. Astrophysics and Space Science Library. DOI: 10.1007/978-3-319-09596-7. arXiv: 1406.4836 [astro-ph.SR].

Vink, Jorick S. (2015). "Very Massive Stars in the Local Universe". In: *Very Massive Stars in the Local Universe*. Ed. by Jorick S. Vink. Cham: Springer International

Publishing, pp. 1–8. ISBN: 978-3-319-09596-7. DOI: 10.1007/978-3-319-09596-7_1. URL: https://doi.org/10.1007/978-3-319-09596-7_1.

Woosley, S. E. (1993). "Gamma-ray bursts from stellar mass accretion disks around black holes". In: *Astrophys. J.* 405, p. 273. DOI: 10.1086/172359.

Woosley, S. E. (2017). "Pulsational Pair-instability Supernovae". In: 836, 244, p. 244. DOI: 10.3847/1538-4357/836/2/244. arXiv: 1608.08939 [astro-ph.HE].

Woosley, S. E. and A. Heger (2006). "The Progenitor Stars of Gamma-Ray Bursts". In: 637, pp. 914–921. DOI: 10.1086/498500. eprint: astro-ph/0508175.

— (2007). "Nucleosynthesis and remnants in massive stars of solar metallicity". In: 442, pp. 269–283. DOI: 10.1016/j.physrep.2007.02.009. eprint: astro-ph/0702176.

— (2015). "The Deaths of Very Massive Stars". In: *Very Massive Stars in the Local Universe*. Ed. by J. S. Vink. Vol. 412. Astrophysics and Space Science Library, p. 199. DOI: 10.1007/978-3-319-09596-7_7. arXiv: 1406.5657 [astro-ph.SR].

Woosley, S. E., A. Heger, and T. A. Weaver (2002). "The evolution and explosion of massive stars". In: *Reviews of Modern Physics* 74, pp. 1015–1071. DOI: 10.1103/RevModPhys.74.1015.